Irradiation Correlation of Microstructural Changes in Metals

... A Computational Study of Collision Cascades

（金属中の微細構造変化に関する照射相関
...衝突カスケードの計算機シミュレーション）

1993年 12月

森 下 和 功

(1)

Irradiation Correlation of Microstructural Changes in Metals

--- A Computational Study of Collision Cascades

Kazunori MORISHITA

December 1993

Department of Quantum Engineering
and Systems Science,
Faculty of Engineering,
University of Tokyo

ABSTRACT

Establishment of correlation rules in radiation effects under different irradiation environments is required for prediction of materials behavior under expected irradiation conditions and for comparison of radiation effects in different irradiation facilities. This requirement is important especially for the development of nuclear fusion reactor materials, where the environment of nuclear fusion does not exist at present, therefore, the irradiation effects to be caused in nuclear fusion reactors must be extrapolated using existing irradiation facilities, as fission reactors and ion accelerators. In the present dissertation, a study of the irradiation correlation rules using computer simulation techniques is described.

Changes in the property of materials irradiated by high-energy particles are accompanied by atomic displacement sequences (so-called "cascades") and nuclear transmutation, determining the integrity and lifetime of construction in irradiation environments. The property changes are strongly associated with the changes in microstructure of the materials. Thus, the microstructural changes can be a good indicator estimating the changes in materials property. Therefore, the irradiation correlation should be prepared by the following two step-wise correlations. One is correlation connecting irradiation conditions, as projectile particles, target atoms, and irradiation temperature, with irradiation-induced microstructural changes in materials (*irradiation-microstructure correlation*). The other is correlation between the microstructural changes and property changes (*microstructure-property correlation*).

For the establishment of irradiation correlation, it is required to introduce a measure, i.e., so-called "an irradiation correlation parameter" that properly describes materials behavior under irradiation condition. Moreover, the irradiation correlation parameter should be able to predict the radiation effects of materials in arbitrary irradiation fields. The number of atomic displacements based on the Norgett-Robinson-Torrens model, i.e., NRT dpa, has been widely accepted as an irradiation correlation parameter so far. However, as represented by many experimental data, the NRT dpa is not always applicable for all radiation effects. Validity to use the NRT dpa as an irradiation correlation parameter is limited to similar irradiation fields. Although the spatial distribution of defects is largely considered to influence damage structures, the concept of the spacing is not incorporated into the NRT dpa. The present author has introduced the concept of the spacing of defects into the irradiation correlation parameter, trying to correlate irradiation-induced microstructural changes under different irradiation fields using computer simulation approach. New correlation rules is obtained for "cascade collapse", i.e., direct defect vacancy cluster formation in collision cascades initiated from high-energy primary knock-on atoms (PKAs).

Principal results obtained in the present study can be summarized as follows;

(1) Molecular dynamics calculations are performed to investigate the temperature dependence of the collisional and cooling phases (*chapter 2*) and cascade overlapping effects (*chapter 3*), indicating that the spatial localization of atomic displacements in the collisional phase may play a significant role on subsequent cascade processes including the

spontaneous recombination of defect pairs and direct defect cluster formation in cascades.

(2) Critical conditions for cascades to collapse into vacancy clusters are obtained using molecular dynamics technique. For the cascade collapse, the differences in atomic density between cascade molten zone and surrounding crystal are more essential than the deposited energy density (*chapter 4*).

(3) Comparisons are made between computational results based on binary collision calculations and ion irradiation experiments. The local density of atomic displacements in the collisional phase can be a good indicator correlating cascade collapse under different irradiation conditions. Cascade collapse probability is strongly related to the vacancy mobility of target elements (*chapter 5*).

(4) A molecular dynamics technique and a finite difference method are integrated to incorporate the electron-phonon coupling effects of cascade thermal spike stage. This new approach is initiated in this research as a practical simulation method and expected to simulate the cooling and thermal phases of cascade damage processes (*chapter 6*).

ACKNOWLEDGEMENTS

The author would like to express his heartfelt gratitude to Prof. Shiori ISHINO for whole-hearted advice, encouragement and arrangement for this work, to Prof. Shuichi IWATA for stimulating suggestions, encouragement and advice, and to Prof. Naoto SEKIMURA for instructive advice, encouragement and kind support.

The author also would like to thank Dr. Howard L. HEINISCH for stimulating comments and support during and after his visit to Pacific Northwest Laboratory (PNL).

The author is also grateful to all members of Ishino's laboratory. He also would like to express thanks to Dr. Hiroshi KAWANISHI and Mr. Yoshio ARAI for encouragement and advice in the matter of his life, to Mr. Akira FUKUMURA for instruction in computer simulation, and to Mr. Takeshi TOYONAGA for computer simulation works and fruitful discussion.

The author also would like to express his gratitude to Dr. Tomas DIAZ de la RUBIA and Mike W. GUINAN of Lawrence Livermore National Laboratory (LLNL) for providing the MOLDYCASK code.

Finally, the author wishes to express his sincere gratitude to his parents for support in all respects.

TABLE OF CONTENTS

GUIDE TO FIGURES

Chapter 1

INTRODUCTION

1-1 Characteristics of Radiation Damage in First Wall Materials of Fusion Reactors

The effective and accelerated research and development of thermonuclear fusion reactors are required for the effective and eternal solution to the international and domestic energy problems. One of the critical issues to be solved for materials development of first wall in fusion reactors is considered to be heavy radiation damage. It is estimated that cumulative wall loading by 14 MeV neutrons generated due to D-T fusion reactions is about 3~10 MW-y/m^2 at the end of the lifetime of the reactor [1-1], corresponding to the atomic displacement damage of 30~100 dpa (displacement per atom). The characteristic features of materials used in irradiation environments compared with those of other industrial materials are as follows [1-2].

- Atomic displacement damage initiated from a primary knock-on atom (PKA)
- Nuclear transmutation reaction

Especially for the first wall, the majority of PKAs have kinetic energies beyond several hundreds of keV, producing successive atomic displacements in a spatially inhomogeneous region called "cascade." If PKA energy is over a certain threshold value called "subcascade energy" that is material dependent, the cascade damage region is divided into several regions, each of which is called "subcascade" [1-3,4,5,6,7]. Such a cascade process produces a large number of athermal point defects in significant local fluctuation in defect concentration. The production, annihilation and accumulation of point defects during the displactive irradiation give rise to microstructural changes in materials, depending on a wide variety of such physical condition as the nature and energy of projectile particles and irradiation temperature. Nuclear transmutation products also play a significant role on the microstructural and microchemical evolution as impurity atoms. For example, the H and He atoms trapped by vacancy agglomerations stabilize the nucleus of cavity and void [1-8,9].

The cascade damage processes are classified into the following four stages; the collisional, cooling, thermal and diffusional phases [1-10]. The collisional phase is defined as a stage of atomic collision sequences, which begins with the first collision of an irradiating particle with target atoms, ending when no atoms have enough energy to create another stable displaced atom. During the collisional phase, which usually lasts a few tenths of picosecond, the cascade structure including the number, size, energy density and spacing of subcascades is already established, depending on PKA energy. Physical argument during the collisional phase is well described within the framework of binary collision. The cooling

phase, which continues for roughly 10^{-13} sec, is defined as a stage of the dissipation of energies deposited locally during the collisional phase, ending when the cascade region becomes thermal equilibrium with its surroundings. During the cooling phase, average kinetic energy in a cascade core is well above the melting temperature of materials and the significant rearrangement of defects takes place including recombination and clustering. After the cooling phase, interaction of point defects occurs by normal, thermally activated diffusion. The thermal and diffusional phases are stages where such defect interaction takes place through defect migration in the short and long distance ranges compared with cascade dimension, respectively. The characteristic durations of such thermal activated processes during the thermal and diffusional phases are $\sim 10^{-6}$ and $\sim 10^{-3}$ sec, respectively. The interactions of defects in the thermal and diffusional phases proceed depending much on irradiation temperature. At extremely low temperature where neither interstitial atoms nor vacancies are mobile, defect interaction in irradiated materials is limited in the collisional and cooling phases, and therefore, the end result of damage structure is largely dependent on the initial cascade structure. At relatively high temperature, interstitial atoms with relatively greater mobility rapidly annihilate in such sinks as dislocations, surfaces, and the vacancy- and interstitial-type clusters, and thereafter, the concentration of interstitial atoms rapidly becomes saturated in a steady state. The concentration of vacancies with smaller mobility needs longer time to become saturated when the rates of the production and annihilation of defects balance. In such defect diffusion processes, surrounding damage structure, including a difference in the spatial distribution of vacancies and interstitial atoms, sometimes influences the end results of damage structures: (i) If there is a dislocation, which prefers to absorb interstitial atoms in nature, more

vacancies can freely migrate around the dislocation, promoting the growth of voids (*dislocation bias* [1-11]). (ii) Once a vacancy cluster is formed directly in nascent cascades (cascade collapse [1-12]), freely migrating interstitial atoms are superior to vacancies in number, promoting the growth of interstitial clusters and the shrinkage of vacancy clusters. (iii) On the other hand, if an interstitial cluster is formed in nascent cascades [1-13], the result of damage structure is largely influenced by freely migrating vacancies (*production bias* [1-14]). (iv) Defect distribution in a cascade, which has a vacancy-rich core with an interstitial-rich periphery at the end of the collisional phase, produces more vacancies at the cascade core, promoting the growth of voids inside the cascade (*cascade localization induced bias; CLIB* [1-15]).

Changes in the properties of neutron-irradiated materials, including changes in hardness, ductility and volume, are brought by changes in the microstructure described above, depending on the production and subsequent behavior of defects as functions of irradiation condition, e.g., the recoil energies, irradiation temperature and the physical properties of target elements. For development of materials used in irradiation environments, basic knowledge of materials response to a given irradiation condition is required. The importance of the knowledge will be described in the following section for the case of materials development of the fusion reactor.

1-2 Simulation Studies for Fusion Materials Development

Simulation irradiation studies with charged particles and fission neutrons have been largely done for development of fusion reactor materials because of the lack of intense fusion neutron sources. These simulation

studies are essentially progressing according to the strategy that Ishino proposed [1-16], which is known as "Ishino's diagram". His basic philosophy is to extend neutron fluence to a high damage region using fission reactors, always considering the correlation of the results to the case of fusion neutron irradiation as schematically illustrated in ***Fig. 1-1***. His concept also contains

- fission-fission correlation,
- fission-ion correlation and
- ion-fusion correlation,

as well as fission-fusion correlation, concretely achieved by performing experiments with the same specimens in different irradiation environments as RTNS-II, FFTF, JMTR, JOYO and ion-accelerators and by studying less ambiguously the effect of spectrum, dose, dose rate and other irradiation parameters.

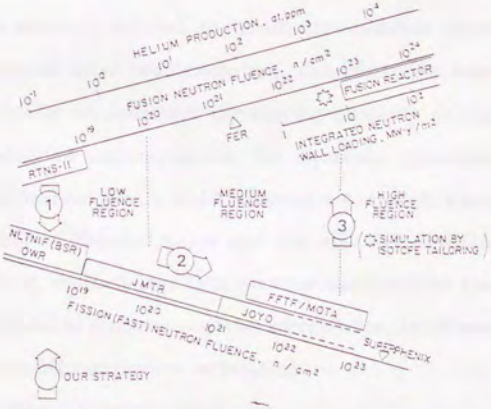

Fig. 1-1 **Strategy of approaching high fluence irradiation effect in a fusion reactor environment by utilizing existing reactors.**

It is one of the central issues for such simulation studies how we should utilize experimental data obtained from existing irradiation facilities for extrapolation to fusion environments. Which parameter should we choose as a scaling parameter when we perform the extrapolation? The correlation parameter should enable us to predict irradiation-induced changes under the wide variety of irradiation environment. Unfortunately, there is no unique correlation parameter that combines all the relationship between irradiation environments and various radiation effects. Hence, the correlation parameter should be determined depending on which correlation is expressed. Thus, these irradiation correlations for different irradiation environments should be established, not only for development of fusion reactor materials, but also for comparison of irradiation data under various experimental conditions.

The macroscopic properties of materials are determined by events occurring at an atomic scale. Irradiation-induced property changes in materials are strongly related to irradiation-induced microstructural changes during and after the irradiation. Therefore, the microstructural changes are ideally an indicator correlating property changes between different irradiation environments; for example, irradiation-induced changes in electrical resistivity and hardening are strongly associated to the absolute number of Frenkel pairs and the size distribution of defects, respectively. Thus, methodology that we must establish for the irradiation correlation is classified into two-stepwise correlations, as follows.

- Irradiation-Microstructure correlation
- Microstructure-Property correlation

The former is to clarify the relationship between irradiation conditions, as recoil energies, irradiation temperature and the physical properties of target material, and irradiation-induced microstructural changes in

materials. The latter is to clarify the relationship between the microstructural changes and the irradiation-induced changes in material property, as the strength, ductility and size stability of materials.

Microstructural changes in irradiated materials are mainly governed by atomic level interactions initiated from the collisions of projectile particles with target atoms. The concept of dpa (displacement per atom) based on the Norgett-Robinson-Torrens (NRT) model [1-17], which reflects successive atomic collisions that are one of the most distinctive features in irradiated materials, has been widely accepted as an international standard irradiation parameter for quantifying the number of atomic displacements in irradiated materials. Unfortunately, the NRT-dpa is not always a good correlation parameter available for all the irradiation correlations, mainly because not all the radiation effects are controlled by only the number of atomic displacements. In practice, the NRT-dpa is generally used just as an irradiation dose rather than an appropriate correlation parameter. The concept of the NRT-dpa does not include spatial fluctuation in defect distribution, nor does it represent the net number of residual defects.

The concept of damage efficiency has been introduced separately by many researchers to try to make the number of residual point defects consistent with the calculated number of atomic displacements. In those works the damage efficiency is only used just as an adjustable parameter without physical argument. Zinkle and Singh [1-18] have recently introduced several damage efficiencies based on each physical process associated with cascade damage, e.g., direct defect clustering in nascent cascades, intracascade thermal recombination in the thermal phase, defect clustering in the diffusional phase and unstable cluster evaporation, as follows.

- Displacement mixing factor (DMF)

- Quenched cascade defect fraction (QDF)
- Correlated recombination surviving defect fraction (SDF)
- Intracascade clustered defect fractions ($CDF_{i,v}$)
- Isolated point defect fractions ($IDF_{i,v}$)

All of those are defined in terms of the NRT calculated displacements. Their concept is expected to be useful for researchers to put their experimental data in order. It is, however, very difficult to obtain such damage efficiencies by experimental methods. Muroga *et al.* [1-19] estimated freely migrating defect fraction by observing the growth rate of interstitial dislocation loops in ion-irradiated Fe-Cr-Ni alloy, and found that their estimation is lower than those obtained from computer simulation and other experiment on segregation measurement. They concluded that other effects, as cascade overlapping effects, are included in their estimation. In this way, it is very difficult to discriminate each effect from the multiple and synergistic effects by experimental methods.

1-3 Computer Simulation of Cascade Damage Processes

Since cascade damage processes during the collisional and cooling phases take place in a spatially localized region (3-5 nm) in a very short time (~10 psec), it is not easy to directly observe the behavior of defects by experiments. Few techniques provide the atomic resolution required to study the primary state of the damage, and what we can do is to monitor only the final state of the damage. Moreover, the inhomogeneous and non-linear characters of cascades make theoretical modeling difficult, and the most analytical work has been limited to highly idealized treatment. Atomistic computer simulation has the advantage of such an atomistic level

resolution. Therefore, in the present study, several computer simulation methods are applied to cascade damage processes at atomic level.

A molecular dynamics (MD) method is a well-defined microscopic description of a many-body system, computing the phase space trajectories of a collection of molecules that individually obey classical laws of motion [1-20]. By using the MD method, one obtains the dynamic properties of a system as well as static one. Application of the MD method to the primary state of cascades provides the most realistic description, including the details of recombination, clustering and thermal energy dissipation.

The MD calculations provide us the schematic view of cascade evolution [1-21], as follows. First, within a few tenths of a picosecond, displaced atoms are generated in a spatially localized region. The number of displaced atoms in the collisional phase is much greater than that of the NRT calculated displacements. Due to the ballistic ejection and replacement collision sequences (RCSs) of interstitials, defect distribution in a collision cascade is spatially segregated into a vacancy-rich core with an interstitial-rich periphery. During the subsequent cooling phase, radial pair distribution functions for atoms located within the disordered regions show that melting occurs in the cascade core. Most of the displaced atoms near the cascade core recombine with vacant lattice sites during the cooling phase. As a result, the number of stable Frenkel pairs produced in the cascade is determined primarily by the number of interstitials transported beyond the boundary of the molten zone of the cascade. Thus, the survival ratio of defects is almost determined by the balance between the size of the molten zone and the number of interstitials escaping from the molten zone. The MD calculation shows [1-21] that, in a 25keV cascade in copper, quenched cascade defect fraction (QDF) defined as the number of survival defects after the cooling phase is estimated as about 0.20 comparable to

experimental data [1-22]. As the PKA energy increases, the size of the core region becomes larger and the escape probability of interstitials decrease. As a consequence, the QDF is decreasing with increasing PKA energy. The MD simulations also show the formation of direct defect cluster in collision cascades. Direct vacancy cluster formation by the collapse of a nascent cascade (so-called "cascade collapse") is observed near the core of a 25keV cascade in copper [1-21]. In addition, an interstitial prismatic dislocation loop is also observed to be punched from the core of the molten zone of the cascade [1-21].

In practice, the MD approach is limited to simulating only a small number of relatively low energy cascades for the simulated time of the order of picoseconds. However, since the cascade process is stochastic in nature, one cascade, or even several, may not be representative of the average cascade behavior. The binary collision approximation (BCA) applied to collision cascades in crystalline materials provides a way to model high-energy cascades with requisite physical reality in statistically significant numbers, although only the collisional phase of a cascade can be modeled. While the BCA simulations cannot correctly describe the ultimate positions of point defects within each subcascades, they nevertheless can provide the realistic description of the gross features of defect distribution, as the size, number and spacing of subcascades.

Using the BCA computer simulation code MARLOWE [1-23], Heinisch and Singh have clearly demonstrated the formation of subcascades from high-energy PKAs in Al, Cu, Ag, Au, Fe, Mo, W, Ti, Zr and Hf [1-24]. Threshold energies for subcascade formation are determined from the energy dependence of defect configurations in the collisional phase. Compared on the basis of reduced damage energy, the metals of the same crystal structure have subcascade thresholds at the same reduced damage

energy. The average number of subcascades per cascade increases linearly with increasing recoil damage energy in all the metals. At a given recoil damage energy, the numbers of subcascades in different metals decrease with increasing atomic number for such elements as transition metals. The separation of nearest-neighbor subcascades in sets of the same energy in a given material has a broad distribution, and the average separations are independent of energy, distributed ranging from the 40 to 70 atomic diameters in all the metals.

1-4 Objective of the present study

In the present study, the primary state of cascade damage processes is investigated using atomistic computer simulation techniques described above to seek effective irradiation correlation parameters for a phenomenon that is mainly governed by the primary damage state. The concept of defect spatial distribution is introduced into a irradiation correlation parameter available for cascade collapse.

In *chapter 2*, the temperature dependence of cascade damage evolution is investigated, followed by discussion of cascade overlapping effects in *chapter 3*, using molecular dynamics technique. In *chapter 4*, the controlling parameter of cascade collapse phenomenon is extracted from molecular dynamics calculations. In *chapter 5*, comparison between binary collision calculations and ion-irradiation experimental data leads the present author to establishment of correlation rules for cascade collapse in different irradiation environments. In *chapter 6*, extension of computer simulation method applied to cascade processes is described, discussing the possibility of simulating the cooling and thermal phases of cascades by incorporation of

electron-phonon coupling effect. The concluding remarks of the present dissertation are given in *chapter 7*.

References 1

[1-1] G.L. Kulcinski, J.M. Dupouy and S. Ishino, J. Nucl. Mater. 141-143 (1986) 3.

[1-2] S. Ishino, Radiation Damage (University of Tokyo Press, Tokyo, 1987) p. 1 (in Japanese).

[1-3] H.L. Heinisch and B.N. Singh, J. Nucl. Mater. 179-181 (1991) 893.

[1-4] Y. Yamamura, J. Nucl. Mater. 179-181 (1991) 94.

[1-5] R. Dierckx, J. Nucl. Mater. 144 (1987) 214

[1-6] T. Muroga, M. Eguchi, N. Yoshida, N. Tsukuda and K. Kitajima, J. Nucl. Mater. 141-143 (1986) 865.

[1-7] Y. Satoh, T. Yoshiie and M. Kiritani, J. Nucl. Mater. 191-194 (1992) 1101.

[1-8] N. Sekimura, Doctoral Dissertation of Engineering, University of Tokyo (1986).

[1-9] F. Kano, Doctoral Dissertation of Engineering, University of Tokyo (1993) (in Japanese).

[1-10] M. Kiritani, Simulation Studies of Radiation Damage Processes by D-T neutron, Report of Research Project, Grant-in-Aid for Scientific Research from Monbusho, Ed. K. Sumita and S. Ishino (March, 1988) (in Japanese).

[1-11] B.C. Skinner and C.H. Woo, Phys. Rev. B30 (1984) 3084; E. Kuramoto, J. Nucl. Mater. 191-194 (1992) 1279.

[1-12] S. Ishino, Rad. Eff. Def. Sol. 113 (1990) 29; C.A. English and M.L. Jenkins, Mater. Sci. Forum 15-18 (1987) 1003.

[1-13] Y. Shimomura, H. Fukushima, M. Kiritani and M.W. Guinan, Mater. Sci. Forum 15-18 (1987) 1093.

[1-14] C.H. Woo, B.N. Singh and F.A. Garner, J. Nucl. Mater. 191-194 (1992) 1224; C.H. Woo and B.N. Singh, Phys. Status Solidi B159 (1990) 609; C.H. Woo and B.N. Singh, Philos. Mag. A65 (1992) 889.

[1-15] T. Yoshiie and M. Kiritani, Mater. Sci. Forum 97-99 (1992) 105; T. Yoshiie, Y. Sato, S. Kojima and M. Kiritani, J. Nucl. Mater. 179-181 (1991) 954; T. Yoshiie and M. Kiritani, J. Nucl. Mater. 191-194 (1992) 1088; T. Yoshiie and M. Kiritani, to be published in the proc. of ICFRM-6 in J. Nucl. Mater.

[1-16] S. Ishino, Bull. Japan. Inst. Met. 26 (1987) 1044 (in Japanese); S. Ishino, T. Kondo and M. Okada, J. Nucl. Mater. 179-181 (1991) 3.

[1-17] M.J. Norgett, M.T. Robinson and I.M. Torrens, Nucl. Eng. Des. 33 (1975) 50; IAEA specialists' meeting, Nucl. Eng. Des. 33 (1975) 91.

[1-18] S.J. Zinkle and B.N. Singh, J. Nucl. Mater. 199 (1993) 173.

[1-19] T. Muroga, K. Mihara, H. Watanabe and N. Yoshida, in: 6th. International Conference on Fusion Reactor Materials (ICFRM6), to be published in J. Nucl. Mater.

[1-20] D.W. Heermann, Computer Simulation Methods in Theoretical Physics (Springer-Verlag, New York, 1990) p.13.

[1-21] T. Diaz de la Rubia, R.S. Averback, H. Hsieh and R. Benedek, J. Mater. Res. 4 (1989) 579; T. Diaz de la Rubia and M.W. Guinan, Mater. Sci. Forum 97-99 (1992) 23; T. Diaz de la Rubia and W.J. Phythian, J. Nucl. Mater. 191-194 (1992) 108; M.W. Guinan and J.H. Kinney, J. Nucl. Mater. 103&104 (1981) 1319.

[1-22] R.S. Averback, R. Benedek and K.L. Merkle, Phys. Rev. B18 (1978) 4156.

[1-23] M.T. Robinson and I.M. Torrens, Phys. Rev. B9 (1974) 5008.

[1-24] H.L. Heinisch and B.N. Singh, J. Nucl. Mater. 179-181 (1991) 893.

Chapter 2

TEMPERATURE DEPENDENCE OF THE PRIMARY STATE OF CASCADE DAMAGE PROCESSES

2-1 Introduction

Almost all the radiation damage processes are stochastic in nature, largely depending on irradiation temperature. The obvious effect of the irradiation temperature on cascade damage evolution is through thermally activated interactions of defects, as diffusion, association or dissociation with other defects. The temperature sensitivity of such interactions is represented by activation energy which depends on individual processes. One of the most important factors to complicate the temperature dependence of radiation damage evolution is a difference in temperature sensitivities depending on the type of the processes, as the production, migration and thermal stability of defects and on the type of defects, as vacancies, self-interstitial atoms (SIAs), impurity atoms and their clusters.

The difference in the temperature sensitivities gives rise to distinctive processes at a given temperature, as void swelling.

Since such stochastic interactions require, at least, a time period of several hundred times as long as that of thermal lattice vibrations, it is considered that the temperature effects do not occur during the cascade collisional phase. However, there is another temperature effect, which is via thermal lattice vibration that disturbs crystallographic structures. The effect of crystallographic structure on the cascade collisional phase in metals gives rise to the following distinctive phenomena predominant in relatively low energy range [2-1].

- Focusing
- Aeolotropy of threshold displacement energy

The focusing indicates collision sequences accompanied with energy transfer into a specific crystallographic direction. Some atoms in the sequences are replaced into different lattice sites from their original ones. Such collision sequence accompanied with mass transfer is called as a replacement collision sequence (RCS), which is one of the most effective mechanisms for an interstitial atom to migrate far away from a cascade core in a short time (~10^{-13} sec). Quenched cascade defect fraction (QDF) [2-2], which is defined as the fraction of the number of survival defects after the cascade cooling phase to the NRT calculated displacements, is considered to be largely related with the number of interstitial atoms escaping from the cascade core through the RCSs. These crystallographic effects on the collisional phase are considered to decrease with increasing irradiation temperature, because thermal lattice vibrations disturb the crystallographic structures of materials.

The NRT model [2-3] suggested that the number of Frenkel pairs (N_D) generated by a primary knock-on atom (PKA) of energy E is given by

$$N_D = \frac{\kappa(E - L_e)}{2E_d} = \frac{\kappa E_D}{2E_d}, \quad E_D > 2E_d/\kappa . \qquad (2.1)$$

Here κ is displacement efficiency, L_e is electronic energy loss, E_D is damage energy, and E_d is threshold displacement energy. Binary collision approximation (BCA) calculations indicate that the displacement efficiency is constant, $k \approx 0.8$ for PKA energies above $2E_d$ [2-4]. The threshold displacement energy is typically equal to ~25 eV, which is about ten times as large as the vacancy formation energy, E_{fv}, of target materials. The threshold energy depends much on target elements and crystallographic orientation in the same elements [2-5]. Moreover, it depends on irradiation temperature.

In the present study, the temperature effects on the primary state of cascade damage processes are investigated using molecular dynamics technique.

2-2 Procedure

Using the molecular dynamics computational technique, the primary states of cascade damage processes are simulated at various irradiation temperatures. The molecular dynamics code GRAPE [2-6] is modified [2-7] to control the initial irradiation temperatures of a computational cell and to apply many-body interatomic potential based on embedded atom method (EAM) [2-8,9] to description of atom behavior.

In the present study, kinetic temperatures are controlled by the following velocity scaling method,

$$\boldsymbol{v}_i^{'}(t) = \boldsymbol{v}_i(t)\,[1 + \alpha\,\{(\frac{T_b}{T(t)})^{1/2} - 1\}]\,, \tag{2.2}$$

where, $\boldsymbol{v}_i$ is the velocity of atom i, T_b is an ambient temperature and α ($0 \leq \alpha \leq 1$) is the degree of the scaling. When α equals to 1, the temperature of a system is strictly scaled to T_b. Since statistical mechanics does not request that the temperature strictly agrees with T_b, α can be randomly chosen step by step. $T(t)$ is kinetic temperature, given by the following relation,

$$T(t) = \frac{1}{3Nk_B} < \sum_{i=1}^{N} m_i\,\boldsymbol{v}_i(t) >\,, \tag{2.3}$$

where, N is the number of atoms and k_B is the Boltzmann constant.

The EAM-type many-body interatomic potential is described by the following,

$$E_{tot} = \sum_i F_i(\rho_{h,i}) + \frac{1}{2}\sum_{i \neq j} \phi_{ij}(r_{ij})\,, \tag{2.4}$$

where, an embedding term F is the functional of a background electron density experienced by atom i, and ϕ is a pair potential term. Foiles, Baskes and Daw suggested [2-8] that the background electron density is expressed as the superposition of atomic s- and d-valence electron densities with no core electrons,

$$\rho_{h,i} = \sum_{j(\neq i)} \rho_j^{a}(R_{ij})\,, \tag{2.5}$$

$$\rho^{a}(R) = n_s\,\rho_s(R) + n_d\,\rho_d(R)\,. \tag{2.6}$$

Here, ρ_s and ρ_d are the densities associated with the s- and d-wave functions, which are individually computed from the Hartree-Fock wave functions [2-10]. The numbers, n_s *and* n_d, are the numbers of outer s- and d-electrons, which are determined so as to give the proper heats of the solution of alloys [2-8]. The total energy, E_{tot}, is expressed in terms of the equation of state of Rose *et al.* [2-11] who have shown that the sublimation energy of most metals as a function of the lattice constant can be scaled to a simple universal function,

$$E_{tot} = -E_{sub}(1 + a^*)\exp(-a^*) . \tag{2.7}$$

In this expression, E_{sub} is the absolute value of sublimation energy at zero temperature and pressure. The quantity a^* is a measure of the deviation from the equilibrium lattice constant,

$$a^* = (a / a_0 - 1) / (E_{sub} / 9B\Omega)^{1/2} . \tag{2.8}$$

Here, B is the bulk modulus of material, a is the lattice constant, a_0 is the equilibrium lattice constant, and Ω is equilibrium volume per atom. The pair-interaction term is suggested to write the pair repulsion between the atoms of types A and B in terms of effective charges, as

$$\phi_{AB}(R) = Z_A(R) Z_B(R) / R , \tag{2.9}$$

where, a simple parametrized form is assumed for the $Z(R)$,

$$Z(R) = Z_0(1 + \beta R^{\gamma})\exp(-\alpha R). \tag{2.10}$$

Here, the value of Z_0 is the number of outer electrons of the atom, and other three parameters (α, β and ν) are empirically determined to yield elastic constants and vacancy formation energy. In the present study, *the simple embedded atom method (EAM) potential* of Oh and Johnson [2-12] is employed to describe interactions between atoms. In this model, they introduced the following features to the original EAM potential of Foiles, Baskes and Daw's; the smooth cut-off function for electron density function and two-body potential, and the analytic form of embedding energy function.

The equations of motions for atoms are integrated using so-called "Leap-frog method" [2-13],

$$\boldsymbol{v}_i(t+\frac{\Delta t}{2}) = \boldsymbol{v}_i(t-\frac{\Delta t}{2}) + \Delta t\,\boldsymbol{F}_i(t)/m_i \quad , \tag{2.11}$$

$$\boldsymbol{R}_i(t+\Delta t) = \boldsymbol{R}_i(t) + \Delta t\,\boldsymbol{v}_i(t+\frac{\Delta t}{2}). \tag{2.12}$$

where, $\boldsymbol{v}_i$ and $\boldsymbol{R}_i$ are the velocity and position of atom i, respectively.

In the present study [2-14], 250 eV cascades are simulated in gold. From the computational cell, one atom is chosen as a 250 eV PKA in the direction of <120>. Prior to the initiation of the cascade events, the cell is equilibrated at 0, 100, 300 and 1000K using the velocity scaling method described before. The value of 0.5 is employed as α in *Eq. (2.2)* for all the time for equilibration. Computational cell contains 10800 gold atoms corresponding to a rectangular parallelepiped of $15a_0$ x $15a_0$ x $12a_0$, where a_0 is the lattice constant. For atoms in the vicinity of the boundary of the cell, periodic boundary condition is employed. A time step equals to 3×10^{-15} sec for all the calculations. Since the system is thermally insulated, there is

eventually a temperature rise but the effect is such that does not affect the whole argument.

2-3 Results

Fig. 2-1 shows the time dependence of the number of displaced atoms in cascades occurred at various initial temperatures, where a displaced atom is defined to be displaced by over one-quarter of the lattice constant from nearest lattice site. The numbers of displaced atoms show a rapid increase in the collisional phase, which is followed by a decrease due to the relaxation of unstable defect pairs. The number of displaced atoms increases with increasing initial lattice temperature in the collisional phase, indicating that the threshold displacement energy has a temperature dependence. The effective threshold energy is higher at lower temperature. The time duration of the collisional phase does not depend much on the initial lattice temperature. During the subsequent cooling phase, the number of displaced atoms decreases with increasing temperature.

Fig. 2-2 shows the time dependence of the mean square displacement (*MSD*) of cascades initiated from a 250 eV PKA at various initial temperatures, where the *MSD* is defined as

$$MSD = \sum_i \frac{\{\boldsymbol{r}_i(t) - \boldsymbol{r}_{0,i}\}^2}{N}, \qquad (2.13)$$

where, $\boldsymbol{r}_i(t)$ and $\boldsymbol{r}_{0,i}$ denote the position at time t and original lattice site of atom i, and N is the number of all atoms in the computational cell. The MSD represents average diffusion distance per atom. From the figure, it is observed that the average diffusion distance per atom during the collisional

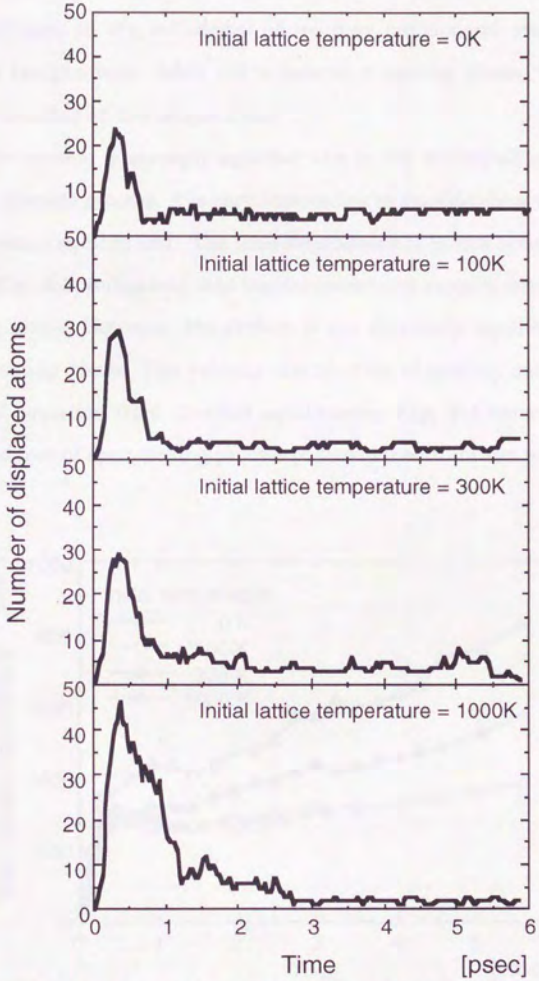

Fig. 2-1 **Time dependence of the number of displaced atoms as a function of initial lattice temperatures. A displaced atom is defined to be displaced by over one-quarter of the lattice constant from nearest lattice site.**

phase does not to depend much on the initial lattice temperature, since the ballistic collision in the collisional phase may not depend much on the irradiation temperature. After the subsequent cooling phase, the MSDs increase depending on the temperature.

Since the system is strongly agitated and in the non-equilibrium state during the cascade process, it is very interesting to consider how the system reaches thermal equilibrium. The time dependence of lattice temperature is shown in ***Fig. 2-3***, indicating that the temperatures remain constant after the cooling phase. However, the system is not thermally equilibrated just after the cooling phase. The velocity distribution of moving particles is a measure of deviation from thermal equilibrium. ***Fig. 2-4*** shows that the time dependence of approaching process to thermal equilibrium at various

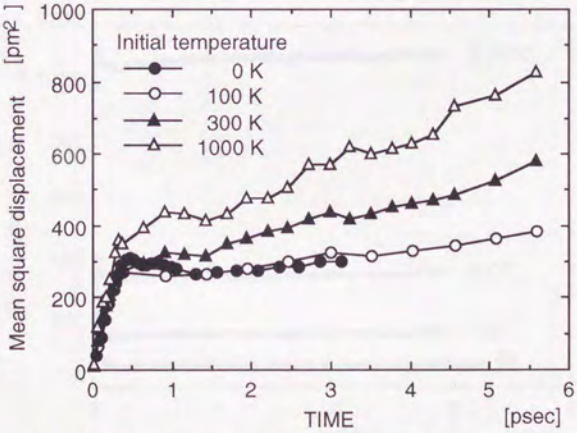

Fig. 2-2 **Time dependence of mean square displacement at various initial lattice temperatures.**

initial lattice temperatures. Here, χ^2 is defined as a measure of deviation from the Maxwell-Boltzmann distribution as

$$\chi^2 = \sum_i (N_i - n_i)^2 / n_i \ , \tag{2.13}$$

where N_i is the velocity distribution of the moving atoms, n_i is the Maxwell-Boltzmann velocity distribution. It is immediately evident that the time to reach equilibrium is much shorter for higher temperatures in these thermally insulated systems.

The trajectories of atom behavior during the collisional phase show clearly that there is temperature dependence of the length of replacement collision sequences (RCSs). Closer examination shows that the temperature

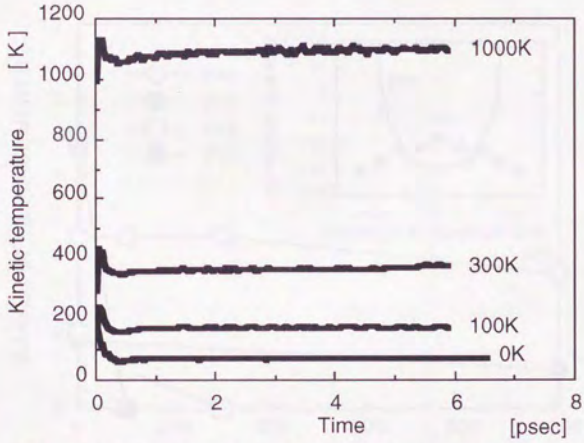

Fig. 2-3 **Time dependence of kinetic temperatures of 250eV cascades at various temperatures.**

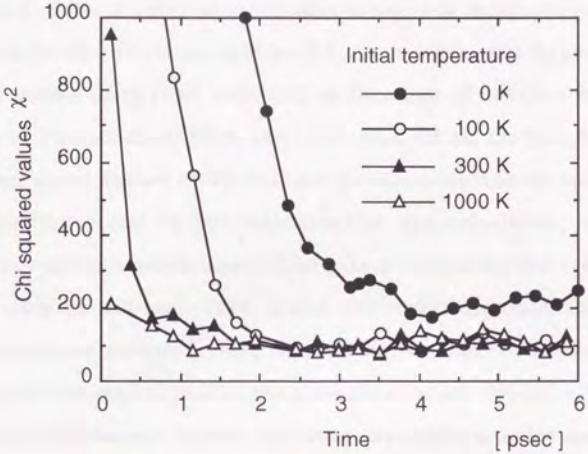

Fig. 2-4 **Time dependence of chi-squared values representing a difference between velocity distribution of moving atoms and Maxwellian velocity distribution.**

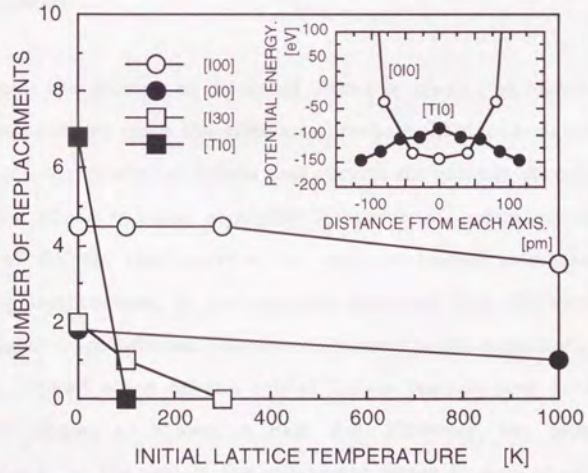

Fig. 2-5 **Length of replacement collision sequences for various directions as a function of initial lattice temperature. The insert shows the potential energy curves along [100] and [110] as functions of the distance from the center of two atoms along [010] and [$\bar{1}$10] axes.**

dependence of the number of replacements depends on the direction of focusing collisions, as shown in ***Fig. 2-5***. An insert in the figure shows potential curves along [100] and [110] as functions of distance from the center of two atoms along [010] and [110] axes, which are calculated by density functional method [2-15]. It is not unreasonable that the relaxation of surrounding atoms is not considered in the calculation, because replacement collision sequences (RCSs) take place during the collisional phase of cascades. Although [110] is a closest-packed direction, there is a local maximum of potential along the central axis and the focusing will easily slip off the central axis by the presence of small thermal vibration. On the contrary, thermal stability of [100] replacement collision sequences can be understood also from the potential curve.

2-4 Discussion

Although the number of displaced atoms is greater at higher initial lattice temperature since the effective threshold displacement energy is lower [2-16], the number of defects that survive the cascade quench during the cooling phase is lower at higher temperature, indicating that the fraction of defects that survive the cascade quench decreases with increasing temperature. In the cascades initiated from the same PKA energy, the average diffusion distance of all atoms in the computational cell does not depend much on the initial lattice temperature during the collisional phase, as shown in ***Fig. 2-2***. However, the number of displacements at the end of the collisional phase is greater at higher temperature. It indicates that the displacement distance increases with decreasing initial lattice temperature. Recombination of defects is more active at higher initial temperature. Moreover, there is not enough time for

the recombination of defect pairs to take place through normal diffusion processes. It is natural to consider that, at higher temperature irradiation, many unstable defect pairs with the short displacement distance are produced in the collisional phase, annihilating in the subsequent cooling phase. Production of such unstable defects at higher temperature is mainly due to the defocusing of RCSs, as shown in ***Fig. 2-5***. The RCS is considered to be an effective mechanism to send interstitial atoms far away from the cascade core. Therefore, a cascade region where atoms are displaced is more compact at higher temperature, although more atoms are displaced due to the lower threshold displacement energy. As a result, unstable defect pairs with short interstitial-vacancy separation are immediately recombined with each other, as shown in ***Fig. 2-1***. Thus, the spatial distribution of the displaced atoms is considered to dominate the quenched cascade defect fraction (QDF), which is defined as the fraction of atomic displacements that survive the cascade quench. For example, experiments show that the QDFs are nearly equal to 1 and 0.3 for the electron and proton-ion irradiations at 4K, respectively [2-17]. This difference in the QDFs is perhaps mainly due to the relative position of vacancy and interstitial atom at the end of the collisional phase. Unfortunately, however, the concept of the spatial distribution of atomic displacements is not incorporated into the NRT model [2-3].

It should be noted that the temperature dependence of the length of RCSs depends on crystallographic direction in metals. Although statistics are not enough to give general discussion, a RCS in the direction of <100> is stronger in the disturbance of crystallographic structure due to thermal lattice vibration than that in <110>, a close-packed direction. The RCS in a <100> direction proceeds with an assistance of the surrounding atoms. In such a so-called "assisted focusing" collision, atoms are migrating along the

minimal point of the potential curve. Therefore, the assisted focusing is observed at higher temperature, while normal RCSs in the close-packed direction are not observed.

2-5 Summary

Molecular dynamics calculation was performed to study the temperature dependence of cascade evolution initiated from a 250 eV PKA in gold. At higher temperature, more displaced atoms are produced since an effective threshold displacement energy is lower. However, most of them are unstable defect pairs due to the shorter separation of interstitial atom and vacancies, so that the QDF is reduced with higher temperature irradiation.

The short interstitial-vacancy separation at higher temperature is predominantly observed in the length of RCS. The assisted focusing process is stable against the large thermal lattice vibration at higher temperature.

Spatial distribution of the displaced atoms, i.e., interstitial-vacancy separation, may dominate the number of defects that survive after the cooling phase.

References 2

[2-1] S. Ishino, Radiation Damage (University of Tokyo Press, Tokyo, 1987) p.103 (in Japanese).

[2-2] S.J. Zinkle and B.N. Singh, J. Nucl. Mater. 199 (1993) 173.

[2-3] M.J. Norgett, M.T. Robinson and I.M. Torrens, Nucl. Eng. Des. 33 (1975) 50.

[2-4] M.T. Robinson and I.M. Torrens, Phys. Rev. B9 (1974) 5008.

[2-5] W.E. King and R. Benedek, J. Nucl. Mater. 117 (1983) 26.

[2-6] J.B. Gibson, A.N. Goland, M. Milgram and G.H. Vineyard, Phys. Rev. 120 (1960) 1229.

[2-7] K. Morishita, Master of Engineering Thesis, University of Tokyo (1991) (in Japanese).

[2-8] M.S. Daw and M.I. Baskes, Phys. Rev. B29 (1984) 6443; S.M. Foiles, M.I. Baskes and M.S. Daw, Phys. Rev. B33 (1986) 7983.

[2-9] G.J. Ackland, G. Tichy, V. Vitek and M.W. Finnis, Phil. Mag. A56 (1987) 735.

[2-10] E. Clementi and C. Roetti, Atomic Data and Nuclear Data Tables (ACADEMIC PRESS, New York, 1974) vol. 14; A.D. McLean and R.S. McLean, Atomic Data and Nuclear Data Tables (ACADEMIC PRESS, New York, 1981) vol. 26.

[2-11] J.H. Rose, J.R. Smith, F. Guinea and J. Ferrante, Phys. Rev. B29 (1984) 2963.

[2-12] D.J. Oh and R.A. Johnson, J. Mater. Res. 3 (1988) 471; D.J. Oh and R.A. Johnson, Atomistic Simulation of Materials, Ed. V. Vitek and D.J. Srolovitz (Plenum, New York, 1989) p.233.

[2-13] T. Okada and E. Ohsawa, Introduction to Molecule Simulation (Kaibundo, Tokyo, 1989) (in Japanese).

[2-14] K.Morishita, N.Sekimura, T.Toyonaga and S.Ishino, J. Nucl. Mater. 191-194 (1992) 1123; K. Morishita, N.Sekimura and S.Ishino, Rad. Eff. Def. Sol. (1993) in press; K.Morishita, T.Toyonaga, N.Sekimura and S. Ishino, Trans. Mater. Res. Soc. Jpn. 9 (1992) 110.

[2-15] W. Kohn and L.J. Sham, Phys. Rev. 136 (3B) (1964) B864; W. Kohn and L.J. Sham, Phys. Rev. 137 (6A) (1965) A1697; P. Hohenberg and W. Kohn; Phys. Rev. 136 (1964) B864.

[2-16] S.P. Chou and N.M. Ghoniem, J. Nucl. Mater. 179-181 (1991) 909.

[2-17] R.S. Averback, R. Benedek and K.L. Merkle, Phys. Rev. B18 (1978) 4156; J.H. Kinney, M.W. Guinan and Z.A. Munir, J. Nucl. Mater. 122&123 (1984) 1028; M.W. Guinan and J.H. Kinney, J. Nucl. Mater. 108&109 (1982) 95; R.C. Birtcher and T.H. Blewitt, J. Nucl. Mater. 98 (1981) 63.

Chapter 3

MOLECULAR DYNAMICS STUDY OF CASCADE OVERLAPPING EFFECTS

3-1 Introduction

There are some attempts to scale radiation-induced microstructural changes in metals with PKA energy spectrum [3-1,2,3]. The attempts are successful in correlating microstructural changes induced by low-dose irradiation in metals under different irradiation sources, indicating that PKA energy spectrum can be a good indicator of irradiation-induced microstructural changes. However, for high-dose, high-energy or molecular-ion irradiations, non-linear effects appear in the correlations.

The non-linear effects are mainly due to the overlapping of cascades, which may appear, for example, in high energy cascades where multiple subcascades interact with each other, at high dose irradiation where a newly formed cascade interacts with pre-existing defects formed by an old cascade, or at molecular-ion irradiation where molecular ions dissociate on

impact and produce strongly overlapping cascades with enhanced energy densities and vacancy supersaturations compared with the single ions of the same total energy.

Some neutron-irradiation experiments [3-1,4] show that defect-cluster yield increases in proportion to the square of neutron dose in the certain range of irradiation dose. Such a so-called "impact effect" [3-1] might occur perhaps due to the cascade energy overlapping, i.e., the shock wave [3-5] from other cascades. The irradiations of molybdenum and α-iron with antimony molecular ions show [3-6] that at the same total ion energy the defect-cluster yield increases with the number of atoms in the ion. Molecular dynamics calculation [3-7] shows that a newly formed cascade initiated from a 5keV PKA near a defect-cluster formed by an old cascade in silver has an impact on the position of the pre-existing defect cluster via replacement collision sequence (RCS). Another molecular dynamics study shows that the defect survival ratio is influenced by the effect of cascade overlapping [3-8]. Also from molecular dynamics simulation, compared to a cascade initiated from a monomer PKA with kinetic energy of 1keV, the enhancement of diffusion coefficient and atomic displacements in a dimer-1keV cascade is observed due to the cascade overlapping effects [3-9]. Diaz de la Rubia *et al.* [3-10] show using molecular dynamics technique that atomic mixing in a dimer-5keV cascade in copper is almost a factor of two larger than in a 10 keV monomer event and very similar in magnitude to a 25keV event.

Thus, there is experimental and computational evidence that cascade overlapping effects may play an important role on cascade damage structures, as defect cluster formation and defect survival ratio. The cascade overlapping effects are considered to be classified as follows.

- Energy overlapping: cascade energy is transferred through shock wave, focussons, *etc.*
- Mass overlapping: atomic mass is transferred via replacement collision sequences (RCSs), ballistic ejection, etc.

Mass transfer is always accompanied with energy transfer. The magnitude of these overlapping effects may be a function of cascade energies and differences in the initiating time and position of cascades.

In the present study, the cascade overlapping effects are evaluated using molecular dynamics technique. Cascade structures are simulated by introducing two PKAs with kinetic energies of 1 keV for each in a parallel direction in copper, then compared with a cascade initiated by a monomer PKA with kinetic energies of 1 and 2 keV.

3-2 Procedure

The molecular dynamics calculation code MOLDYCASK [3-11] developed by Diaz de la Rubia *et al.* is used to investigate cascade overlapping effects in copper. The MOLDYCASK code makes very efficient use of the vector processing capabilities of the CRAY-2 supercomputer, employing the vectorized link cell (VLC) method of Heys and Smith [3-12] to generate the tables of neighboring atoms for efficient calculation of interatomic forces. Integration of the classical equations of motion is carried out by means of a fourth order predictor-corrector algorithm [3-13]. The predicted values are given by

$$x(t+\Delta t)=x(t)+u_1+u_2+u_3\ , \tag{3.1}$$

$$u_1(t+\Delta t)=u_1(t)+2u_2+3u_3\ , \tag{3.2}$$

$$u_2(t+\Delta t) = u_2(t) + 3u_3 \text{ and} \tag{3.3}$$

$$u_3(t+\Delta t) = u_3(t) \ . \tag{3.4}$$

Here,

$$x\ (t) = coordinate \ , \tag{3.5}$$

$$u_1 = x^{'}(t)\Delta t \ , \tag{3.6}$$

$$u_2 = \frac{1}{2}x^{''}(t)\Delta t \ , \tag{3.7}$$

$$u_3 = \frac{1}{6}x^{'''}(t)\Delta t \ . \tag{3.8}$$

The corrected values are then given by

$$x^c\ (t+\Delta t) = x\ (t+\Delta t) + c_0\phi \ , \tag{3.9}$$

$$u_{1c}(t+\Delta t) = u_1(t+\Delta t) + c_1\phi \ , \tag{3.10}$$

$$u_{2c}(t+\Delta t) = u_2(t+\Delta t) + c_2\phi \ , \tag{3.11}$$

$$u_{3c}(t+\Delta t) = u_3(t+\Delta t) \ , \tag{3.12}$$

where, c_i 's are constant, F is an interatomic force and

$$\phi = \frac{1}{2}\frac{F}{m}(\Delta t)^2 - u_2(t+\Delta t) \ . \tag{3.13}$$

The equation of the motion of atoms is described by the Langevin equation [3-14] as follows;

$$m\,\frac{d\boldsymbol{v}}{dt} = \boldsymbol{F} - \beta\boldsymbol{v} + \boldsymbol{R}(t)\ , \tag{3.14}$$

where $\boldsymbol{v}$ is the atom velocity and $\boldsymbol{R}(t)$ is a random force that satisfies

$$<\boldsymbol{R}(t)> = 0\ , \tag{3.15}$$

$$<\boldsymbol{R}(t)\boldsymbol{R}(t')> = 2\beta k_B T\,\delta(t-t')\ , \tag{3.16}$$

with the distribution

$$P(\boldsymbol{R}) = (2\pi <\boldsymbol{R}^2>)^{-1/2} \exp(-\boldsymbol{R}^2/2<\boldsymbol{R}^2>)\ . \tag{3.17}$$

The Langevin equation of motion is employed in order to implement Caro and Victoria's model [3-15] for electronic losses and thermal conduction in metals, applying to all atoms in the crystallite rather than to just those in boundary cells, by connecting the coupling parameter β with the electronic charge density estimated in the framework of the embedded atom method (EAM) [3-16].

In the present study [3-17], the MOLDYCASK code is converted to be available on the HITAC S-820/S-3800 supercomputers, and applied to the simulation of displacement collision sequences from 2 PKAs and subsequent defect clustering in copper. Interatomic potential used here is the modified EAM potential that developed by Diaz de la Rubia *et al.* to perform high energy cascade simulation [3-11]. The simulation cell contains 55296 atoms, which is large enough so that boundary effects on defect production are

minimal. Periodic boundary condition is applied to the boundary atoms. Prior to an initiation of events, system is equilibrated at 10 K. Two PKAs are simultaneously introduced in a parallel direction with kinetic energies of 1 keV for each. Distance between the two PKAs, ***dx***, is varied in the range of 0.25-3 nm. For comparison with those dimer cascade events, cascades initiated from a monomer PKA with kinetic energies of 1 and 2 keV are also simulated. Computational condition is listed in ***Table 3-1***, where ϕ is an azimuthal angle and θ is a polar angle. It is noted in the table that cascade events initiated from monomer PKAs with kinetic energies of 1 and 2 keV are shown by representing the distances between two PKAs as 0.0 and ∞, respectively.

Table 3-1 **Distance between two PKAs, PKA energies and directions of PKAs in the simulated cascade events.**

ID	Distance between PKAs dx (nm)	PKA energy E (keV)	PKA direction θ (degree)	ϕ (degree)
1	(0.0)	2.0	37.5	36.0
2	0.255	1.0 + 1.0	37.5	36.0
3	1.02	1.0 + 1.0	37.5	36.0
4	1.53	1.0 + 1.0	37.5	36.0
5	1.78	1.0 + 1.0	37.5	36.0
6	2.55	1.0 + 1.0	37.5	36.0
7	3.10	1.0 + 1.0	37.5	36.0
8	(∞)	1.0	37.5	36.0

3-3 Results

The (001) projections of instantaneous defect configuration are shown in ***Fig. 3-1*** as functions of time, where symbols ●, ○ and + represent a displaced atom, a vacant lattice site and an uncorrelated-recombined atom, respectively. Here the uncorrelated-recombined atom indicates an atom that is replaced in a different lattice site from its original lattice site. The time

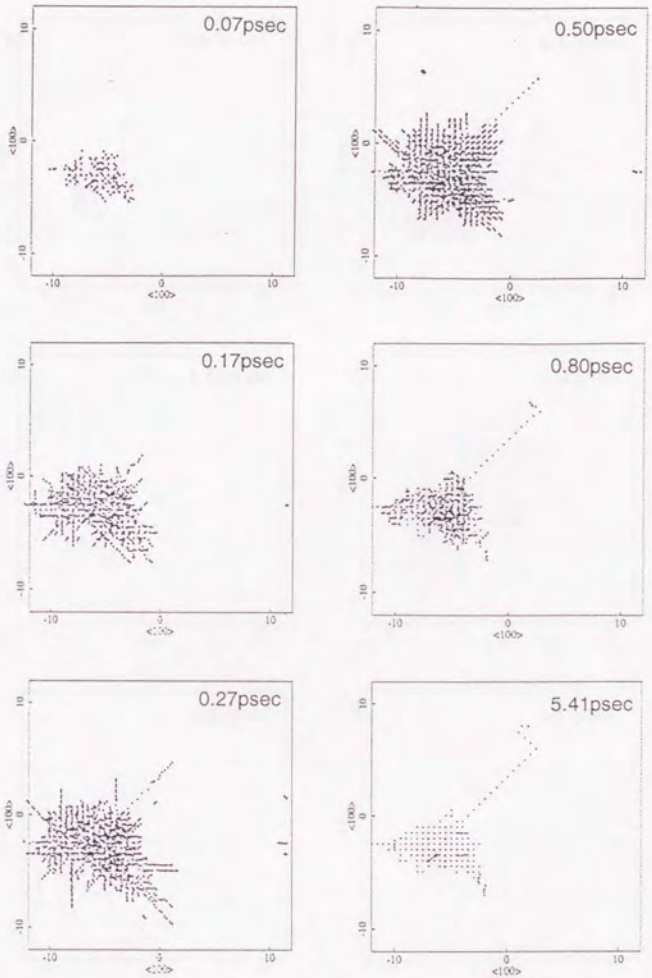

Fig. 3-1 (a) The (001) projections of instantaneous defect configuration in dimer cascade events of dx=0 nm (E_{PKA}=2keV), where symbols ●, ○ and + represent a displaced atom, a vacant lattice site and an uncorrelated-recombined atom, respectively.

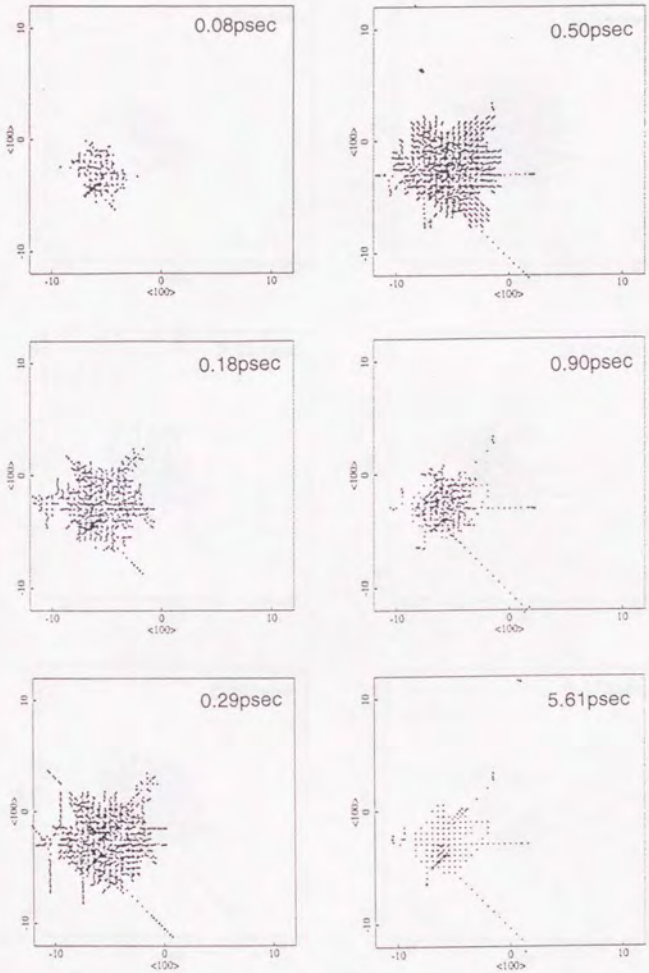

Fig. 3-1 (b) **The (001) projections of instantaneous defect configuration in dimer cascade events of dx=0.26 nm, where symbols ●, ○ and + represent a displaced atom, a vacant lattice site and an uncorrelated-recombined atom, respectively.**

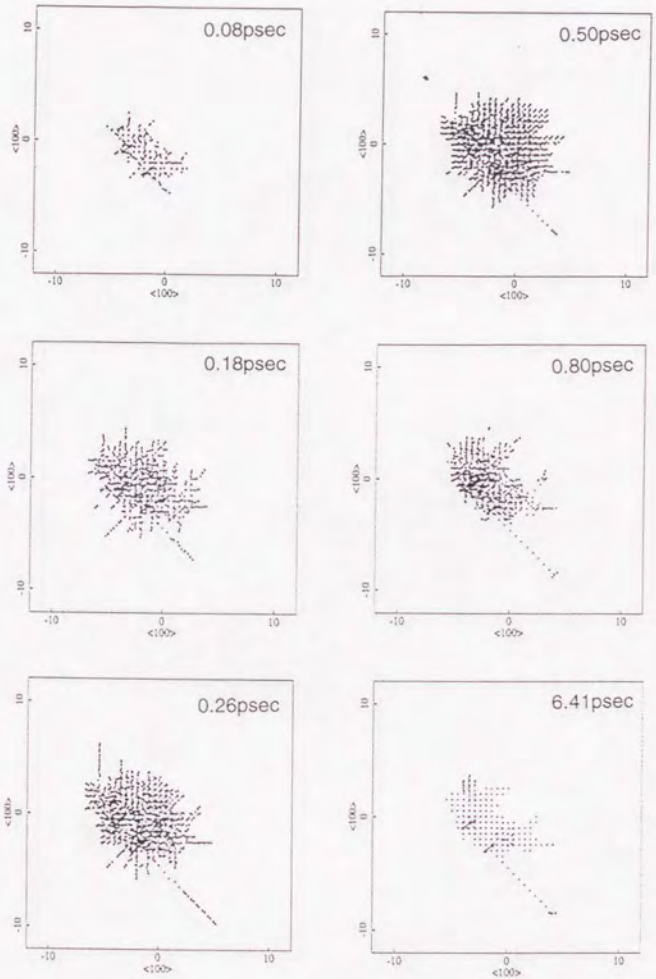

Fig. 3-1 (c) **The (001) projections of instantaneous defect configuration in dimer cascade events of dx=1.02 nm, where symbols ●, ○ and + represent a displaced atom, a vacant lattice site and an uncorrelated-recombined atom, respectively.**

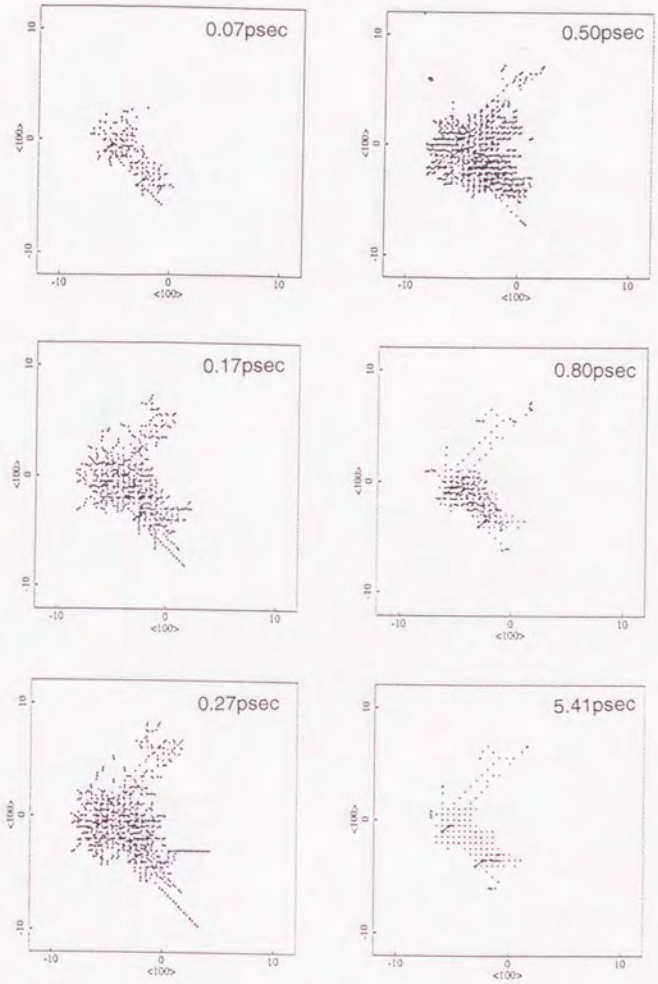

Fig. 3-1 (d) **The (001) projections of instantaneous defect configuration in dimer cascade events of dx=1.53 nm, where symbols ●, ○ and + represent a displaced atom, a vacant lattice site and an uncorrelated-recombined atom, respectively.**

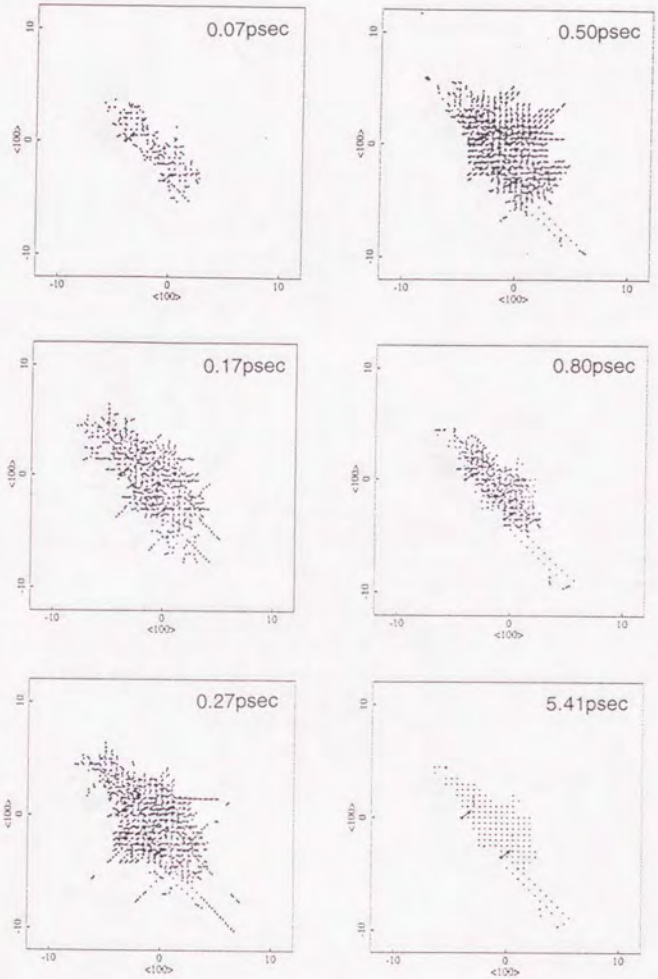

Fig. 3-1 (e) **The (001) projections of instantaneous defect configuration in dimer cascade events of dx=1.78 nm, where symbols ●, ○ and + represent a displaced atom, a vacant lattice site and an uncorrelated-recombined atom, respectively.**

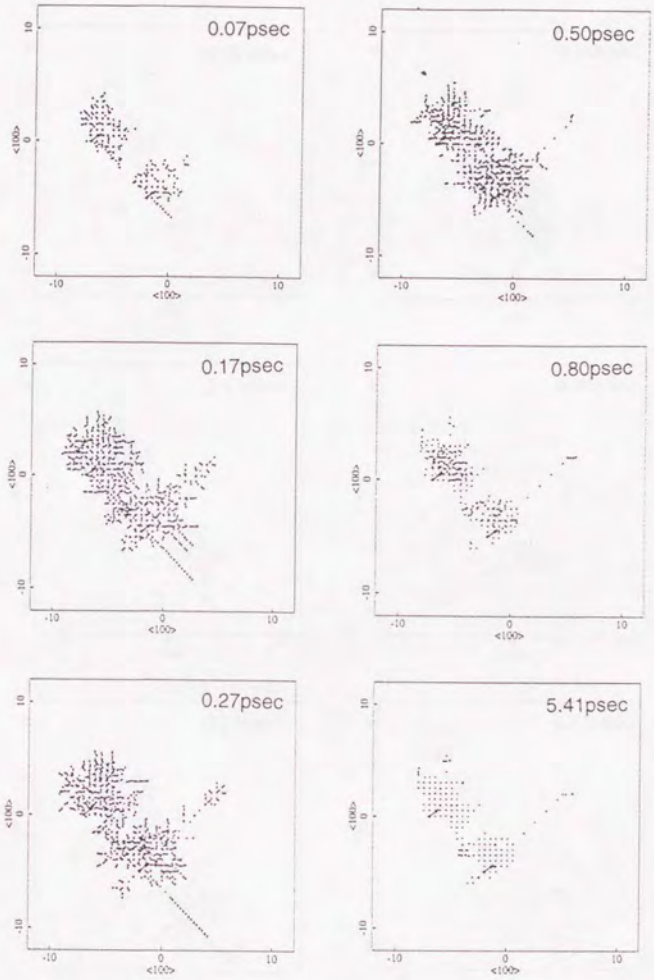

Fig. 3-1 (f) **The (001) projections of instantaneous defect configuration in dimer cascade events of dx=2.55 nm, where symbols ●, ○ and + represent a displaced atom, a vacant lattice site and an uncorrelated-recombined atom, respectively.**

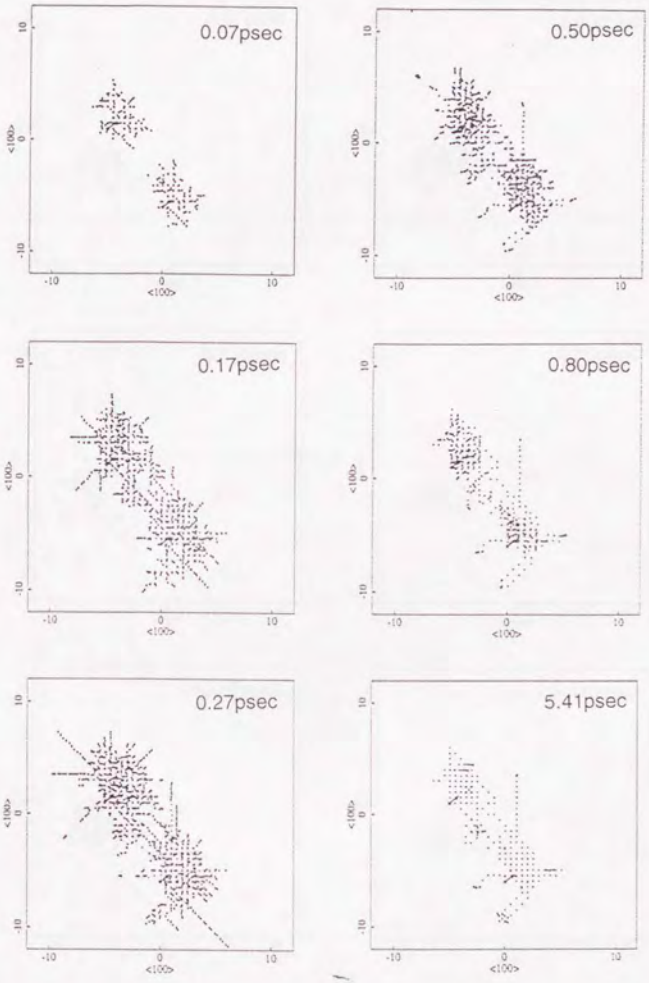

Fig. 3-1 (g) **The (001) projections of instantaneous defect configuration in dimer cascade events of dx=3.10 nm, where symbols ●, ○ and + represent a displaced atom, a vacant lattice site and an uncorrelated-recombined atom, respectively.**

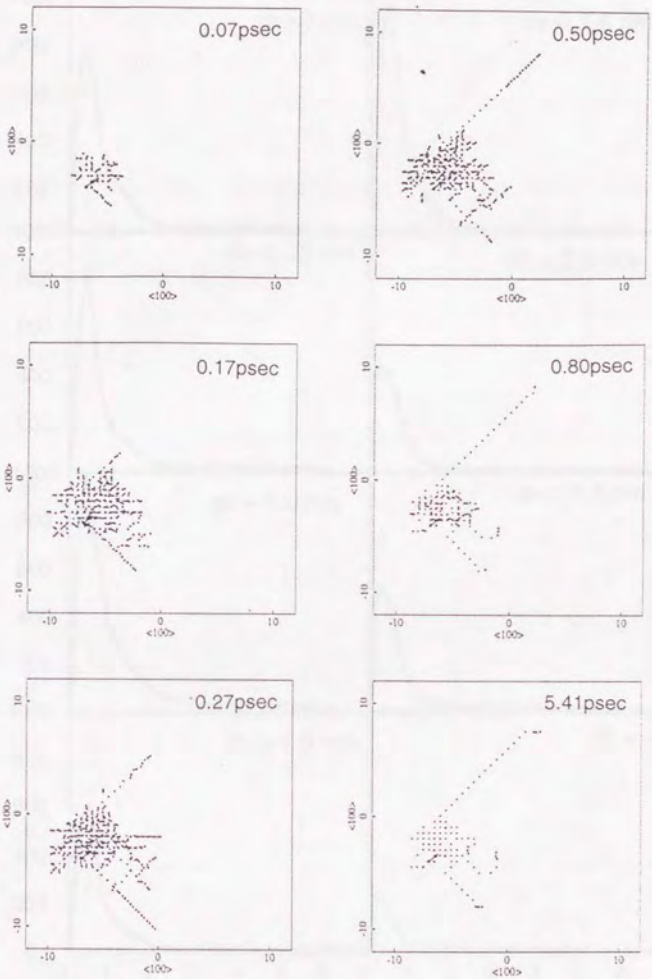

Fig. 3-1 (h) **The (001) projections of instantaneous defect configuration in dimer cascade events of dx=∞ nm (E_{PKA}=*1keV*), where symbols ●, ○ and + represent a displaced atom, a vacant lattice site and an uncorrelated-recombined atom, respectively.**

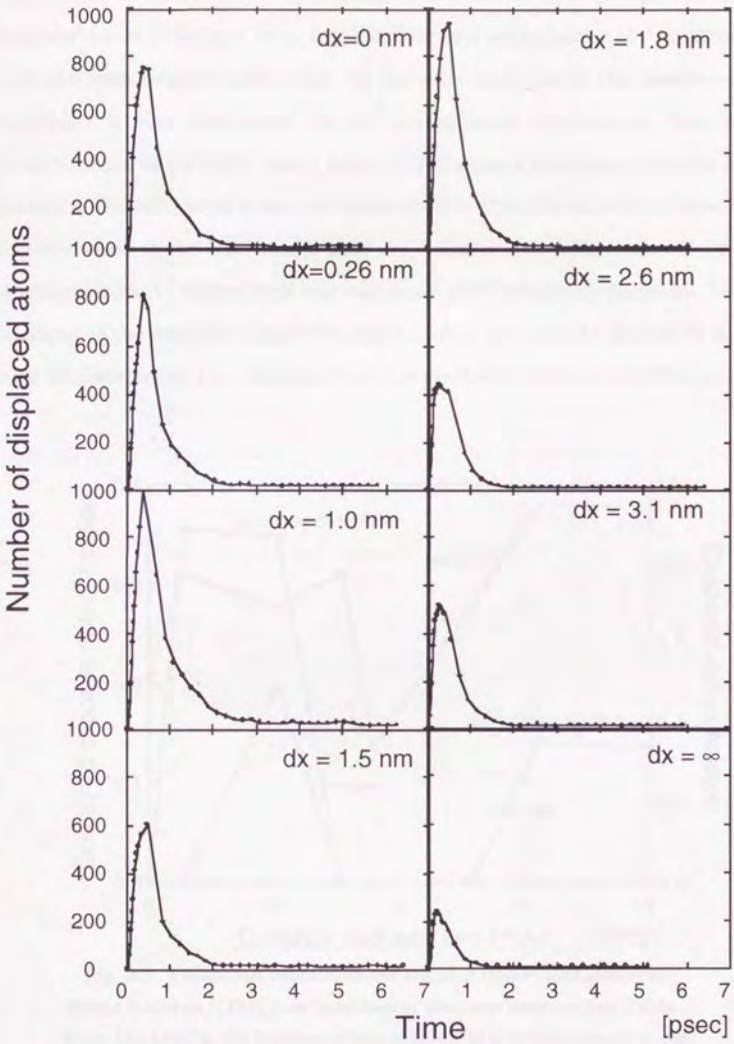

Fig. 3-2 Time dependence of the number of displaced atoms as a function of distance between two PKAs, where a displaced atom is defined to be displaced by over one-quarter of the lattice constant from the nearest lattice site.

dependence of the number of displaced atoms is shown in ***Fig. 3-2***, where a displaced atom is defined to be displaced by over one-quarter of the lattice constant from nearest lattice site. In the collisional phase the number of displaced atoms increases, then immediately decreasing due to recombination of unstable defect pairs. The numbers of displaced atoms at the end of the collisional phase are much greater than the calculated atomic displacements of the NRT model that are estimated as 28.6, 28.9 and 14.5 at monomer-2keV, dimer-1keV and monomer-1keV events, respectively. The fractions of the number of survival defects after the cascade quench to the NRT displacements, i.e., the quenched cascade defect fractions (QDFs), are

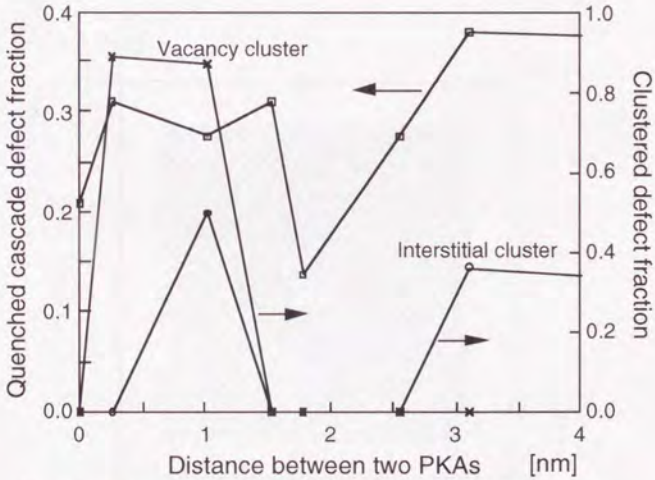

Fig. 3-3 **Quenched cascade defect fraction (QDF) and clustered defect fraction ($CDF_{i,v}$) as functions of distance between two PKAs. Here, the QDF is the fraction of the number of survival defects to the NRT calculated displacements. The CDF is the fraction of clustered interstitials and vacancies to the NRT displacements.**

Fig. 3-3 as a function of the distance between two PKAs, ***dx***. The fractions are complicatedly varied due to cascade overlapping effects.

Fig. 3-4 shows atomic configurations on (001) plane of width $a_0/2$ (a_0 is the lattice constant) in the dimer cascade event of ***dx***=1.02nm at the end of the collisional phase, where highly disordered region is clearly seen near the center of the cascade. The disordered zones are also observed in the other cascades, including monomer events. ***Fig. 3-5*** is the results of Voronoi polyhedron analysis [3-18,19] for atoms in the core of the dimer cascade event of ***dx***=1.02nm as a function of time, indicating that the core is largely disordered and has a liquid-like structure during the cooling phase. Here, the cascade core is defined to be the spherical volume of radius $2a_0$ with the

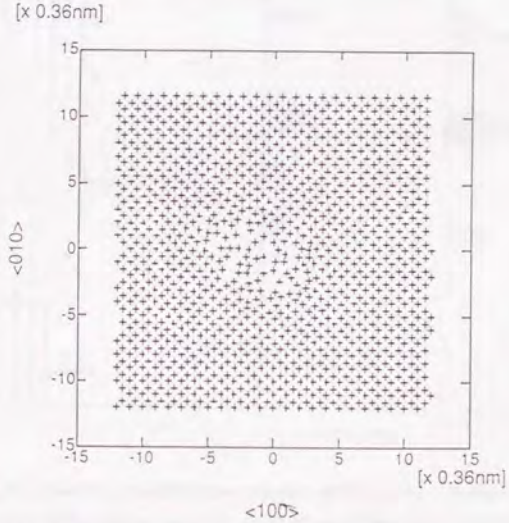

Fig. 3-4 **(001) projection of instantaneous atomic configuration at the end of the collisional phase within cross sectional slabs of thickness $a_0/2$ in a dimer cascade event of *dx*=1.02nm.**

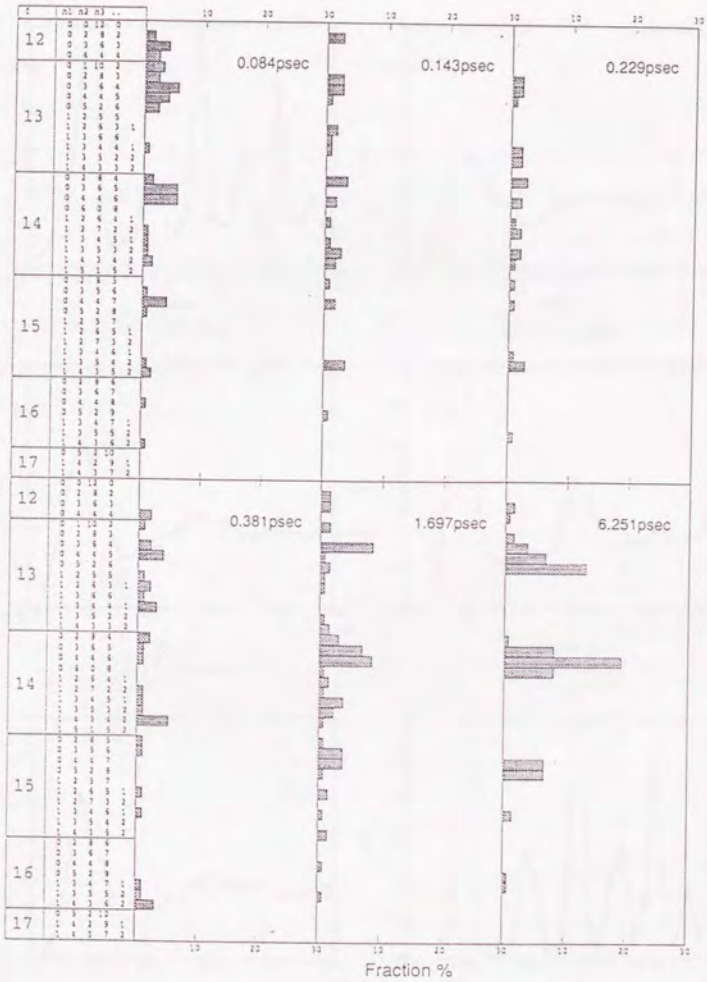

Fig. 3-5 **Voronoi polyhedron analysis of the atomic configuration in the core of the dimer event of dx=1.02 nm. The core is defined to be the spherical volume of radius $2a_0$ with the center of the gravity of the deposited kinetic energies above melting temperature at the end of the collisional phase.**

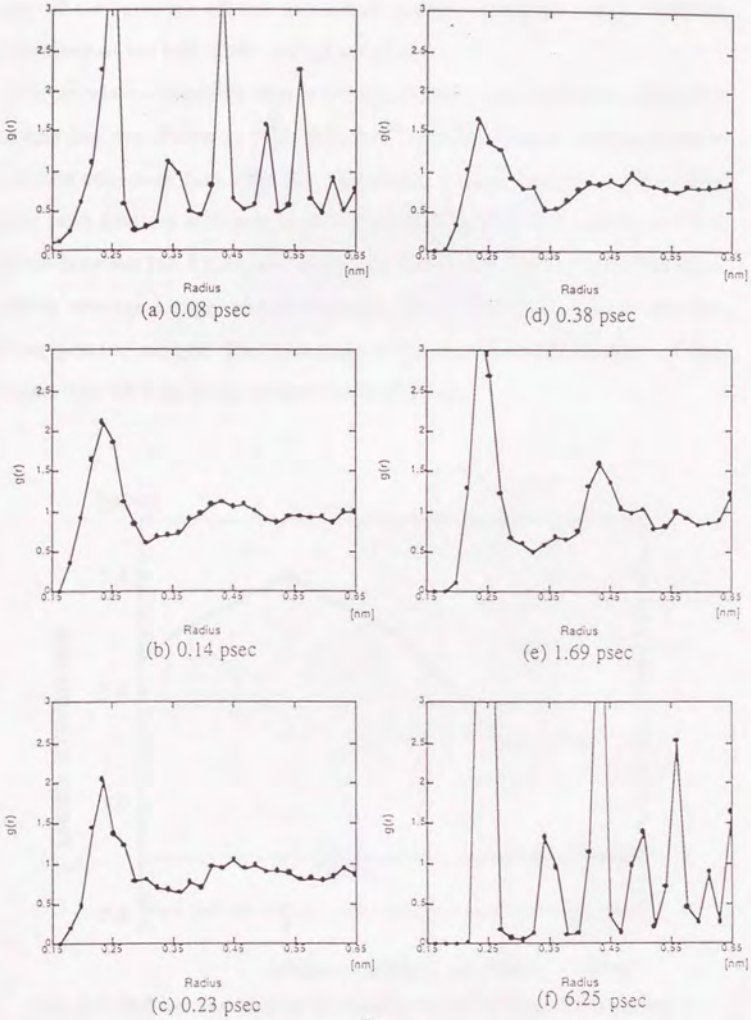

Fig. 3-6 **Pair correlation function averaged over the atoms in the cascade core of the dimer event of dx=1.02 nm as a function of time. It represents a liquid-like structure during the cooling phase.**

center of the gravity of the deposited kinetic energies above melting temperature at the end of the collisional phase.

Pair correlation function that is averaged over atoms in the cascade core of radius $2a_0$ are shown in ***Fig. 3-6*** as a function of time, representing a liquid-like structure just after the collisional phase. The variation of the molten zone lifetime of cascades is shown in ***Fig. 3-7*** as a function of the distance between two PKAs, ***dx***, where the lifetime is defined to be the time at which average kinetic temperature in the cascade core falls below the melting point of copper. The variation is not a monotonic function of the distance. The lifetime is the longest at ***dx***=1.02 nm.

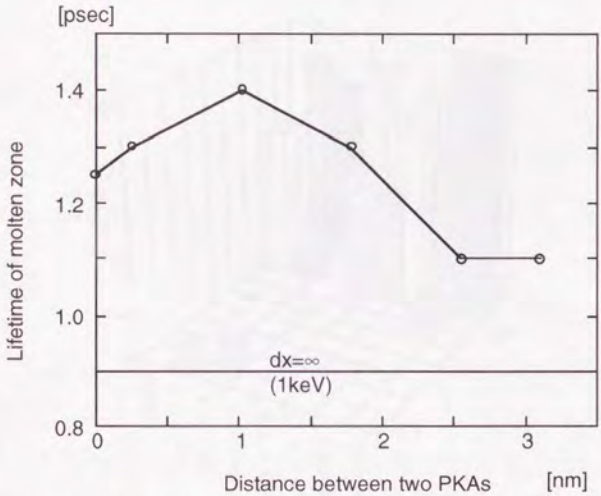

Fig. 3-7 **Molten zone lifetime of cascades versus distance between two PKAs. The molten zone lifetime is defined as the time at which average kinetic temperature in the cascade core region falls below the melting point.**

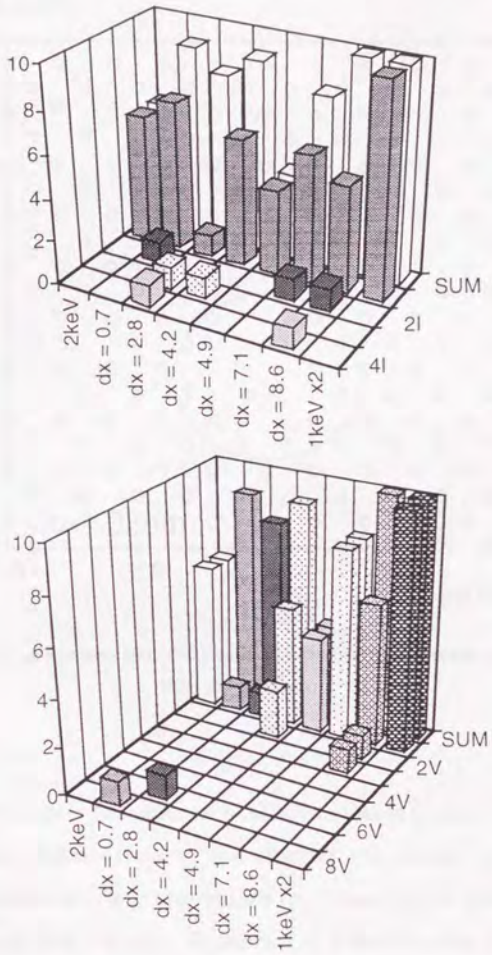

Fig. 3-8 Size distribution of defect clusters formed in dimer cascade events as a function of the distance between two PKAs, *dx*.

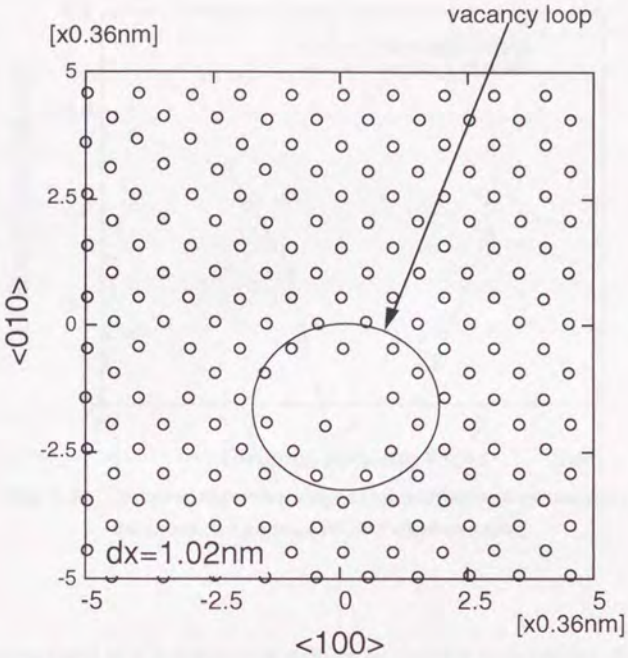

Fig. 3-9 **A vacancy loop formed in the dimer-1keV cascade event with *dx*=1.02 nm.**

Direct defect cluster formation in a collision cascade is observed in some cases. The size distributions of the clusters are shown in ***Fig. 3-8***. Interstitial clusters with four interstitials are formed at the dimer cascade events of ***dx***=3.1 and 1.02 nm. Clustering of 7 and 8 vacancies are also observed at the ***dx***=0.26 and 1.02 nm events, respectively. The vacancy cluster formed at the ***dx***=1.02 nm event is found to be a vacancy loop on (001) plane, as shown in ***Fig. 3-9***. Neither vacancy- nor interstitial-clusters are observed at monomer PKA events in the simulated energy range.

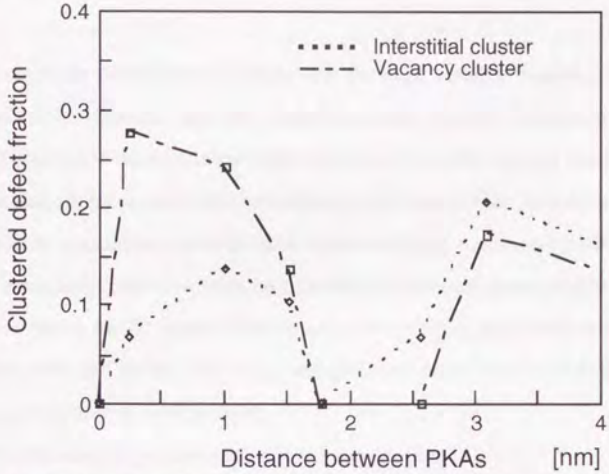

Fig. 3-10 **Clustered defect fractions of interstitials and vacancies to the calculated number of NRT displacements.**

The fractions of the number of defects in clusters that consist of more than two defects to the calculated displacements of the NRT model (i.e., the interstitial- and vacancy-clustered defect fraction; $CDF_{i,v}$ [3-20]) are shown in ***Fig. 3-10*** as functions of the distance between two PKAs, ***dx***. Diaz de la Rubia *et al.* found that the CDF_i and CDF_v in events initiated from 5keV monomer PKA in copper are 0.07 and 0.06, respectively [3-21]. They also obtained 0.21 and 0.14 as the $CDF_{i,v}$ in their 25keV monomer cascade, respectively. In the present study, there are some dimer events whose $CDF_i s$ and $CDF_v s$ are greater than those of monomer events, as shown in ***Fig. 3-10***. It indicates that the clustering probability of defects is possibly enhanced due to the cascade overlapping effects.

3-4 Discussion

The cascade overlapping effects are through energy transfer with *or* without mass transfer. All the dimer cascade events simulated in the present study are accompanied with the mass transfer. Due to the ballistic ejection and replacement collision sequences of interstitials, the distribution of defects in a collision cascade that initiated from a monomer PKA gives rise to a vacancy-rich core with an interstitial-rich periphery [3-22~27]. On the other hand, at the dimer PKA event, the overlapping effects with mass transfer give rise to the following complicated distribution of defects, as schematically shown in ***Fig. 3-11***.

- The overlapping of interstitials (*I-I overlapping*),
- The overlapping of interstitials and vacancies (*I-V overlapping*),
- The overlapping of vacancies (*V-V overlapping*).

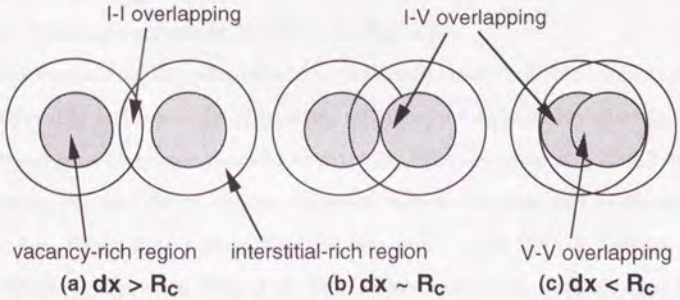

Fig. 3-11 **Schematic view of the cascade overlapping effects, which are divided into (i) I-I overlapping, (ii) I-V overlapping and (iii) V-V overlapping. Localization of cascade defects due to the cascade overlapping effects gives rise to the enhancement of efficiencies of defect clustering. R_c indicates the approximate radius of a single cascade.**

These spatial distribution of defects caused by the cascade overlapping effects influences the efficiencies of defect production and their clustering.

The quenched cascade defect fraction (*QDF*) considerably depends on how far and how efficient the interstitials and vacancies are separated at the end of the collisional phase, because almost all the atoms in a cascade molten zone can recombine with the vacant lattice site. The separation of interstitials and vacancies depends much on the nature of the cascade overlapping effects, i.e., (i) *I-I*, (ii) *I-V* and (iii) *V-V* overlappings. At the ***dx***=1.78 nm event, where the *I-V* overlapping is possibly dominant, interstitial atoms and vacancies are efficiently recombined in the region where interstitial atoms and vacancies are closely distributed. Thus, the *QDF* of the ***dx***=1.78 nm event is the smallest in the simulated events. On the other hand, in the ***dx***=0.255 and 1.02 nm events that correspond to the case of $\boldsymbol{dx}<R_c$ in ***Fig. 3-11***, the *I-V* overlapping region, where an efficient recombination can take place, largely separates the regions of the *V-V* overlapping and interstitial-rich periphery. As a result, the *QDF*s at those dimer events are enhanced, as shown in ***Fig. 3-3***.

The cascade overlapping effects on the spatial distribution of defects also considerably influence the clustering efficiency of defects. No clusters are observed in a monomer cascade event with PKA energies of 1 and 2 keV. However, in some dimer events, clustered defects are observed as shown in ***Fig. 3-8***. From that figure, the clusters with more than 4 defects are extracted to show in ***Fig. 3-3***. The interstitial- and vacancy-types of clusterings take place in the condition where the distances between two PKAs are relatively long and short, respectively. In the ***dx***=3.10 nm event where the I-I overlapping is possibly dominant, an interstitial cluster is observed near the center of the two cascades. In the ***dx***=0.255 and 1.02 nm events corresponding to the V-V overlapping, vacancy clusters are formed.

Especially for the ***dx***=1.02 nm event, the vacancy cluster is found to be a vacancy loop on the (001) plane. In this case the molten zone lifetime is the longest of the simulated cascades in the present work as shown in ***Fig. 3-7***. Thus, the defect clustering directly in a cascade is almost determined by the defect distribution at the end of the collisional phase. Moreover, the collapse of vacancies into a dislocation loop may require a long molten zone lifetime for vacancies to migrate on the same plane.

It is noted that at the ***dx***=1.02 nm event both types of defect clusters are formed by the cooperative mechanism of interstitials and vacancies, as shown in ***Fig. 3-1(c)*** and schematically shown in ***Fig. 3-12***. At that event, vacancies in the core of a cascade (call "A") are recombined with interstitials ejected from another cascade (call "B"). Therefore, interstitials ejected from the "A"-cascade cannot return to the core of their original "A"-cascade. In consequence, such interstitials are punched out from their original "A"-cascade, resulting in an interstitial cluster. Vacancies in the "B"-cascade lose a *chance* to recombine with interstitial atoms, because the interstitials

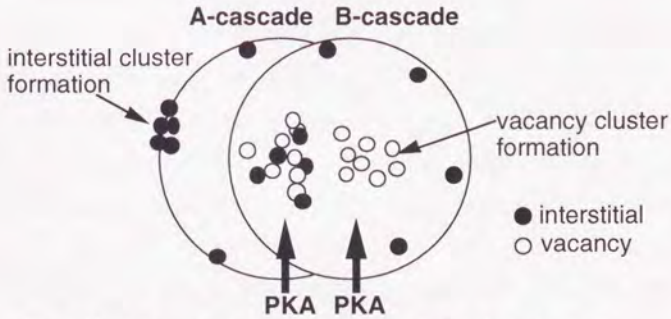

Fig. 3-12 **Schematic view of a cooperative defect clustering in the dimer event at *dx*=1.02 nm. Cascade overlapping effects assist to form both types of defect clusters.**

from the "B"-cascade recombine with the vacancies in the "A"-cascade, resulting in a vacancy cluster near the core of the "B"-cascade. In this way, the cascade overlapping effects can give rise to such a cooperative and assisted mechanism of defect clustering. In fact, molecular-ion irradiation experiments show enhancement of vacancy-cluster yield.

3-5 Summary

The overlapping effects of cascade defects were investigated using molecular dynamics technique. The efficiencies of defect production and their clustering are influenced by the cascade overlapping effects, depending on the distance between two PKAs.

Even at too small energy density deposition to produce defect clusters directly in a monomer cascade event, the defect clusters can be formed at some dimer cascade events. It indicates that direct defect cluster formation in a collision cascade significantly depends on the spatial localization of defects at the end of the collisional phase.

References 3

[3-1] M. Kiritani, T. Yoshiie, S. Kojima and Y. Satoh, Rad. Eff. Def. Sol. 113 (1990) 75.

[3-2] N. Sekimura, Y. Kanzaki, S.R. Okada, T. Masuda and S. Ishino, in: Sixth International Conference on Fusion Reactor Materials (ICFRM6); to be published in J. Nucl. Mater.; T. Masuda, Graduate Thesis (1993) University of Tokyo; Y. Kanzaki, Master of Engineering Thesis (1993) University of Tokyo.

[3-3] Y. Satoh, T. Yoshiie and M. Kiritani, J. Nucl. Mater. 191-194 (1992) 1101.

[3-4] S.R. Okada, N. Sekimura, J. Saeki, K. Yoshii and S. Ishino, presented at the 113rd. Japan Institute of Metals (1993) at Nagoya; S.R. Okada, Master of Engineering Thesis (1994) University of Tokyo.

[3-5] M.W. Guinan, J. Nucl. Mater. 53 (1974) 171.

[3-6] C.A. English and M.L. Jenkins, Mater. Sci. Forum 15-18 (1987) 1003.

[3-7] Y. Shimomura, T. Diaz de la Rubia and M.W. Guinan, presented at the 112nd. Japan Institute of Metals (1993) at Yokohama.

[3-8] W.J. Phythian and C.A. English, in: IEA workshop in La Jolla, USA; to be published in Rad. Eff. Def. Sol. (1993).

[3-9] F. Rossi and N.V. Doan, Nucl. Instr. Meth. B61 (1991) 27; N.V. Doan, F. Rossi and L. Boulanger, J. Nucl. Mater. 191-194 (1992) 1106.

[3-10] T. Diaz de la Rubia and M.W. Guinan, Mater, Sci. Forum 97-99 (1992) 23.

[3-11] T. Diaz de la Rubia and M.W. Guinan, J. Nucl. Mater. 174 (1990) 151.

[3-12] D.M. Heyes and W. Smith, Information Quarterly for Computer Simulation of Condensed Phases, No 26 (Science and Engineering

Research Council, Daresbury Laboratory, Warrington WA4AD, England, 1987) p.68.

[3-13] A. Ueda, Computer Simulation (Asakura, Tokyo 1990) p.29 (in Japanese).

[3-14] D.W. Heermann, Computer Simulation Methods in Theoretical Physics (Springer-Verlag, New York, 1990) p.55.

[3-15] A. Caro and M. Victoria, Phys. Rev. A40 (1989) 2287; S. Pronnecke, A. Caro, M. Victoria, T. Diaz de la Rubia and M.W. Guinan, J. Mater. Res. 6 (1991) 483.

[3-16] M.S. Daw and M.W. Baskes, Phys. Rev. B29 (1984) 6443.

[3-17] T. Toyonaga, Master of Engineering Thesis (1993) University of Tokyo; T. Toyonaga, K. Morishita, N. Sekimura and S. Ishino, presented at the Atomic Energy Society of Japan (1993 spring).

[3-18] J.L. Finney, J. Comp. Phys. 32 (1979) 137.

[3-19] M. Tanemura, T. Ogawa and N. Ogita, J. Comp. Phys. 51 (1983) 191.

[3-20] S.J. Zinkle and B.N. Singh, J. Nucl. Mater. 199 (1993) 173.

[3-21] T. Diaz de la Rubia and M.W. Guinan, Mater. Sci. Forum 97-99 (1992) 23.

[3-22] T. Diaz de la Rubia, R.S. Averback, H. Hsieh and R. Benedek, J. Mater. Res. 4 (1989) 579.

[3-23] A.J.E. Foreman, W.J. Phythian and C.A. English, Harwell AEA Technology Report AEA-TRS-2031 (1991).

[3-24] M.W. Guinan and J.H. Kinney, J. Nucl. Mater. 103&104 (1981) 1319.

[3-25] H.L. Heinisch, Radiat. Eff. Def. Solids 113 (1990) 53.

[3-26] J.A. Brinkman, J. Appl. Phys. 25 (1954) 961.

[3-27] H.L. Heinisch and B.N. Singh, Philos. Mag. A67 (1993) 407.

Chapter 4

MOLECULAR DYNAMICS STUDY OF VACANCY CLUSTER FORMATION DIRECTLY IN COLLISION CASCADES

4-1 Introduction

Collapse of vacancy-rich zones formed in cascade cores to vacancy clusters has significant consequences for the subsequent microstructural changes in metals irradiated with ion and fast neutron, and may play an important role in such processes as void swelling, irradiation hardening and irradiation-induced creep [4-1]. The vacancy cluster has various configurations, as a Frank faulted loop, a perfect loop and a stacking fault tetrahedra (SFT), depending on its cluster size and material parameters as stacking-fault energy. The vacancy cluster formation directly in collision cascades still takes place at extremely low irradiation temperatures below Stage I_e, showing that the cluster formation is an athermal process [4-2]. This indicates that the directed motion of vacancies in a collision cascade

toward cluster nucleus takes place during the collisional and cooling phases of the cascade.

A large number of experimental studies have been done to determine cascade collapse efficiencies in ion-irradiated metals. Two parameters are most commonly used to describe the efficiencies of the cascade collapse. The first is the defect yield defined as the number of vacancy clusters observed by transmission electron microscope (TEM) per incident ion. The second is the cascade efficiency given by the number of vacancies retained in the vacancy cluster formed as a result of the collapse per the calculated number of vacancies generated in the cascade.

The ion-irradiation experiments show that the cascade collapse probabilities depend on the irradiation and materials variables as follows [4-3].

- Ion energies, mass and PKA energy spectra
- Target elements, impurities, composition
  and lattice structure (fcc, bcc, hcp)
- Irradiation temperature

The defect yield generally increases with ion energy. Moreover, an increase in ion mass at constant energy generally increases the defect yield [4-3,4], with some exceptions [4-5]. This suggests that the deposited energy density and the related vacancy supersaturation are important parameters in governing the cascade collapse.

In bcc and hcp metals, defect yield and cascade efficiency are on average lower than those in fcc metals [4-3]. In fcc metals, the Frank loops formed by cascade collapse unfault to perfect loops only in high stacking fault energies [4-6], while the Frank loops dissociate to form complicated geometries in low stacking fault energy [4-7]. In bcc metals, most of the Frank loops tend to unfault to perfect loops due to the high stacking fault

energy. As perfect loops can glide through the lattice, they may, if suitably oriented, be lost to irradiation surface through the action of image forces. The loop loss to the surface is particularly important in bcc metals for estimation of the correct value of cascade collapse efficiencies from experiments.

Vetrano *et al.* investigated the effects of addition of dilute solute elements to Ni on the probability and size of the vacancy loops directly formed in collision cascades [4-8]. The effects of additional solute elements are very complex. With increasing solute content, the defect yield shows an initial increase followed by a decrease. TEM-image size remains unchanged in very dilute alloys and then increases with further solute addition. They concluded that these observations can be explained by solute effects on the character of the molten zone of cascades, as interruption of replacement collision sequences (RCSs) and focussons and interstitial-solute binding.

Black *et al.* show [4-9] the temperature dependence of the defect yields in ion-irradiated Cu_3Au. The cascade collapse in Cu_3Au takes place with significantly lower probability at 30 K than in corresponding room-temperature irradiations. They concluded that this reduction is attributed to the faster resolidification rate of the molten zone at 30 K.

Thus, the cascade collapse phenomenon depends largely on the variety of the materials and irradiation parameters as described above.

In the present study, computer simulations of cluster formation by the directed motion of vacancies in copper are performed using the molecular dynamics technique to determine dominant parameters for the collapse. In the previous chapter, the interstitial- and vacancy-type clusterings of cascade defects were observed in dimer PKA events, showing the importance of the localization of atomic displacements at the end of the collisional phase, i.e., how efficiently interstitials and vacancies are

separated mainly due to the replacement collision sequences and ballistic ejection of interstitials. For direct vacancy-cluster formation in collision cascades by the collapse of cascade defects, atomic density in cascade molten zone at the end of the collisional phase is considered to be strongly associated with the probability of the cascade collapse. In this work, only the thermal spike in the cooling phase of cascade processes is simulated. For that purpose, prior to initiation of cascade thermal spike, vacancies are introduced in computational cell.

4-2 Procedure

The MOLDYCASK code [4-10] described in the previous chapter is applied for simulating the cascade collapse in copper. Simulation cell containing 10976 atoms that correspond to a $14a_0$ cube was, in advance, equilibrated at the irradiation temperature of 10 K before the energy deposition to the cell. To avoid the dependence of cascade evolution on the direction of PKA, the central region of the simulation cell is heated by giving the Gaussian distributed velocities to the atoms, in stead of simulation of a PKA-initiated cascade where an atom in the simulation cell is chosen to give PKA energy. Deposited energy densities simulated in the present work are ranging from 0.0 to 1.5 eV/atom, which covers 0.96 eV/atom corresponding to the energy density of a 25keV-cascade in copper [4-11]. In the PKA-initiated cascade simulation, it is very difficult to extract the features from the simulations, since the following two parameters are complicatedly dependent on each other; the number of atoms escaping from the cascade molten zone through RCSs *or* ballistic ejection and the energy density deposition. This is why such parameters are separately controlled as input data in the present study. However, such a method simulates only

the cascade thermal spike stage, excluding the characteristic features in the collisional phase, as the RCSs and ballistic ejection of interstitials. Therefore, the atoms, which escape from cascade molten zone and cannot get back the cascade core, are introduced prior to an initiation of the spike in order to make the region predominant for vacancies, as general cascade core. Hence, several vacancies are, in advance, introduced into the simulation cell in such a way that the same number of atoms is randomly removed from a "cascade volume" that is defied as a sphere with radius of $5a_0$ (a_0 is the lattice constant). The initial vacancy density defined in the present work is, therefore, a measure of the efficient separation of displaced atoms and vacant lattice sites at the end of the collisional phase. To fit the average number of vacancies retained in a vacancy cluster observed by ion-irradiation experiments, the numbers of initially introduced vacancies are chosen to be 0, 42 and 105, corresponding to that the fractions of the number of atoms to the number of lattice sites in the cascade volume are 0, 2 and 5 %, respectively.

After an introduction of vacancies into the cascade volume, kinetic energies are deposited into the cell by endowing atoms in the simulation cell with a Gaussian radial distribution of velocities that corresponds to the desired energy. The spherical Gaussian distribution of temperatures is given by

$$T_g = T_0 \exp\left(-\frac{\boldsymbol{r}^2}{2\sigma^2}\right) + T_{irr}, \qquad (4.1)$$

where T_0 is central temperature, T_{irr} is irradiation temperature and σ is the width of the Gaussian distribution. The deposited energy E that incident particle transfers to the lattice by elastic collision is given by

$$
\begin{aligned}
E &= \int 3k_B NT\, dV \\
&= \int_0^\infty 3k_B N_0 4\pi r^2\, dr\, T_0 \exp\left(-\frac{r^2}{2\sigma^2}\right) \\
&= 3k_B N_0 (2\pi\sigma)^{3/2} T_0, \qquad (4.2)
\end{aligned}
$$

where, k_B is the Boltzmann constant, N is the number of atoms, N_0 $(=1/\Omega)$ is the atomic density. Thus, the central temperature is described by

$$
T_0 = \frac{E\ \Omega}{3k_B (2\pi\sigma)^{3/2}}. \qquad (4.3)
$$

At an initiation of the heat spike, the velocity of atom i at the position $\boldsymbol{r}_i$ in the simulation cell is multiplied by $(\frac{T_g}{T_c})^{1/2}$, where T_c is the current kinetic temperature of the atom i. Half of the energies deposited are immediately converted to potential energies within ~10^{-13} sec. The deposited energy E and width σ are listed in ***Table 4-1***.

The trajectories of vacancies are observed for ~20 psec after the initiation of the heat spike. To identify the characteristics of cascade evolution, several parameters are introduced in the present analysis, as follows.

- ENERGY DEPOSITION [eV] defined as the kinetic energy deposited in the cascade volume.
- ENERGY DENSITY [eV/atom] given by the energy deposition divided by the number of atoms in the cascade volume.
- MEAN SQUARE DISPLACEMENT (*MSD*) [m^2] defined as

  $$< \boldsymbol{r}^2 > = \sum_{i=1}^{N} \frac{\{\boldsymbol{r}_i(t) - \boldsymbol{r}_i(0)\}^2}{N},$$

  where $\boldsymbol{r}_i(t)$ is the atom position at time t and N is the number of atoms in the cascade volume.

Table 4-1 Computational condition

ID No.	Gaussian		Deposited Energy Density (eV/atom)	Initial Vacancy Density					
				0 %		2 %		5 %	
	Energy E_0(eV)	Width σ (a_0)		MSD (a_0^2)	AD (%)	MSD (a_0^2)	AD (%)	MSD (a_0^2)	AD (%)
1	0	-	0.0	-	100.0	-	98.1	-	95.9
2	1000	4	0.15	0.036	100.0	0.036	98.1	0.037	95.9
3	625	2.5	0.21	0.036	100.0	0.037	98.1	0.041	95.7
4	5000	5	0.45	0.035	100.0	0.044	97.9	0.105	90.6
5	6500	5	0.58	0.038	99.7	0.075	96.2	0.198	86.0
6	7500	5	0.67	0.048	99.7	0.117	94.4	0.288	86.9
7	5000	4	0.76	0.103	99.5	0.208	92.4	0.371	86.4
8	10000	5	0.89	0.323	99.5	0.427	92.2	0.591	85.8
9	7500	4	1.14	0.591	100.8	0.727	92.4	0.854	86.4
10	10000	4	1.53	1.25	99.3	1.34	93.9	1.45	88.0

- MIXING EFFICIENCY (*ME*) [m^5/eV] given by the *MSD* per unit energy density.
- ATOMIC DENSITY [%] defined as the fraction of the number of atoms to the lattice points in a given volume.

The energy deposition and the energy density are the quantity at the beginning of heat spikes, t=0. The *MSD* is a measure of the self-diffusion distance per atom during the cascade damage processes. The volume, in which the atomic density is defined, is a sphere with a center of the gravity of vacancies.

4-3 Results

After an initiation of the spike, a large number of vacancies and interstitial atoms are immediately generated in the cascade volume, showing a liquid-like structure in the cascade core. Kinetic lattice temperatures decay with time constant of 4~6 psec, depending on the energy deposition. In quenched cascades at t≈20psec after the spike initiation, various defect configurations are observed depending on the cascade event. Without energy deposition (simulation ***ID=1***), the migration of vacancies is not observed, showing that spontaneous collapse does not take place without energy deposition in the present work. However, with a help of energy deposition, vacancies in a cascade volume migrate to form a cluster in some events, which are marked with solid circles in ***Fig. 4-1***. Examples of the cross sectional views of final atomic configuration formed in the heat spike events are shown in ***Fig. 4-2*** and ***Fig. 4-3***. ***Fig. 4-2*** is the case for the event of 0.89 eV/atom deposition at the initial vacancy density of 2% (***ID=8***), representing the formation of a vacancy loop on (010) plane.

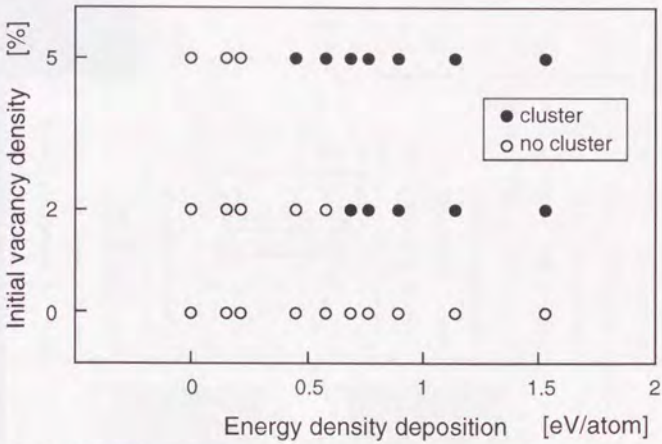

Fig. 4-1 **Initial computational condition of the present work. The abscissa indicates initial energy density deposition, and the ordinate shows initial density of vacancies introduced prior to the initiation of cascade events. A solid circle indicates that vacancy clusters are observed at the end of the calculation.**

Fig. 4-3 shows the very close configuration of stacking fault tetrahedra (*SFT*) in a 5% cascade with 0.58 eV/atom deposition (***ID=5***).

As shown in ***Fig. 4-1***, vacancy clusters are formed at the higher energy density deposition than ~0.7 and ~0.5 eV/atom in the 2% and 5% cascade events, respectively. In the 0% cascade events, no clusters are observed by the energy deposition in the range of the present work, although thermal, single vacancies are formed at higher energy density deposition than ~0.5 eV/atom.

Fig. 4-4 shows a plot of energy density deposition versus final atomic density in a cascade core that is defined as a sphere with a center of the

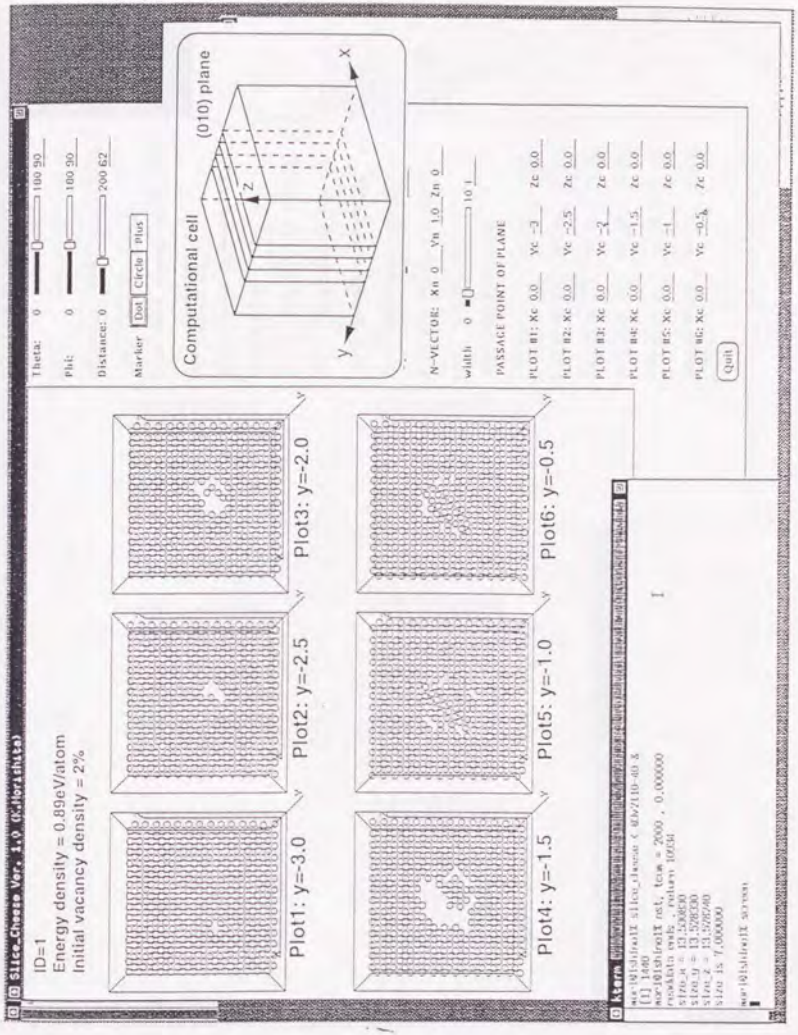

Fig. 4-2 **Cross sectional views of final atomic configuration in the event of 0.89 eV/atom deposition at the initial vacancy density of 2% (ID=8). A vacancy loop is formed on (010) plane.**

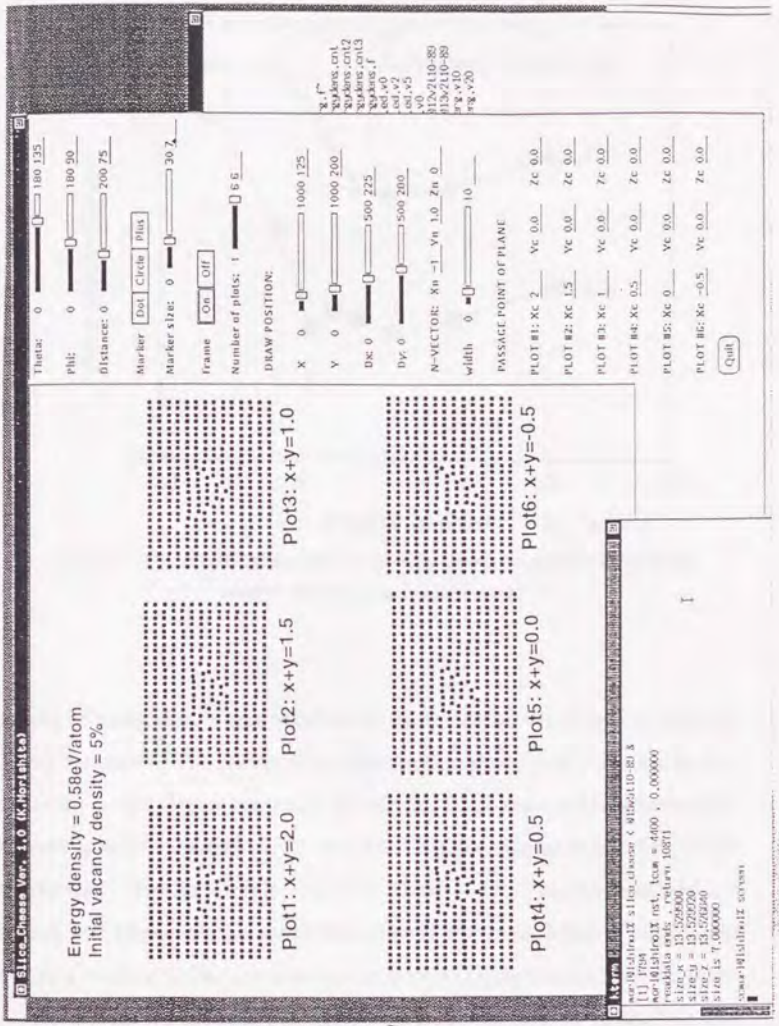

Fig. 4-3 Cross sectional views of final atomic configuration in the event of 0.58 eV/atom deposition at initial vacancy density of 5% (ID=5). The very close configuration of stacking fault tetrahedra is clearly seen.

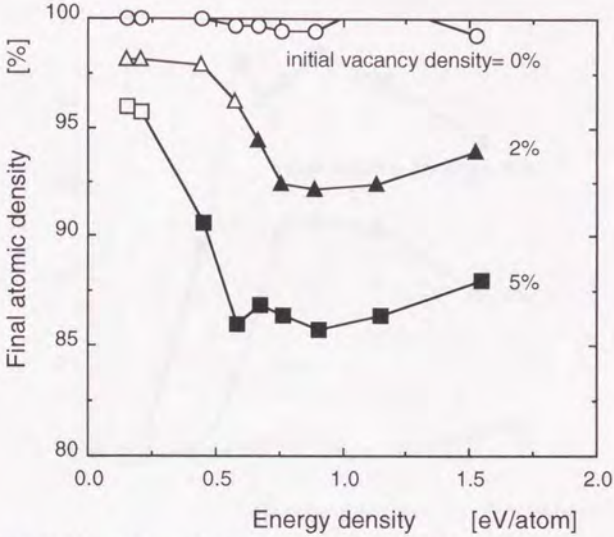

Fig. 4-4 **The relationship between energy density deposition and final atomic density in a cascade core.**

gravity of vacancies, where solid symbols represent the events of vacancy cluster formation. The radius of the spherical cascade core is chosen as $3a_0$, where a_0 is the lattice constant, giving the most reasonable relationship between atomic densities in the core and vacancy cluster formation. In the events with smaller atomic densities than ~94%, vacancy clusters are formed, and hereafter, the atomic densities in this core, which is meaningful only in a relative sense, are used as a measure of vacancy cluster formation.

Fig. 4-5 shows the relationship between energy density deposition and the net number of vacancies entering the cascade core during the events. The number of the entering vacancies, ΔN_v , is a measure of vacancy transport during the events. The figure shows an initial increase followed

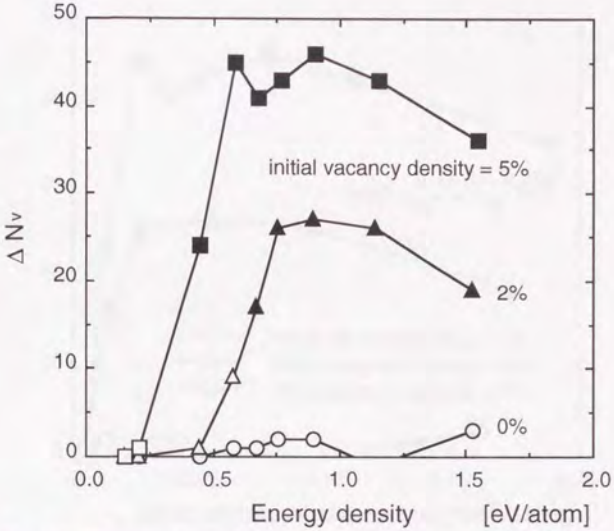

Fig. 4-5 **The relationship between energy density deposition and net number of vacancies entering the cascade core.**

by a small decrease with increasing energy density deposition, depending on the initial vacancy densities. Although the decreasing trend in the figure is not clear, it might be related with the detail configuration of vacancy clusters. The relationship between ΔN_v and *MSD* given at the end of the simulation is shown in ***Fig. 4-6***. From the figure it is found that the vacancy transports are different depending on initial vacancy density even at the same *MSD*, the atomic diffusion distance per atom. ***Fig. 4-5*** and ***Fig. 4-6*** indicate that neither energy density deposition nor *MSD* is a good indicator of vacancy transport during the cascade evolution.

Fig. 4-7 is a plot of the initial vacancy densities versus the *MSD*s at the end of the calculation, representing that, even at the same energy density

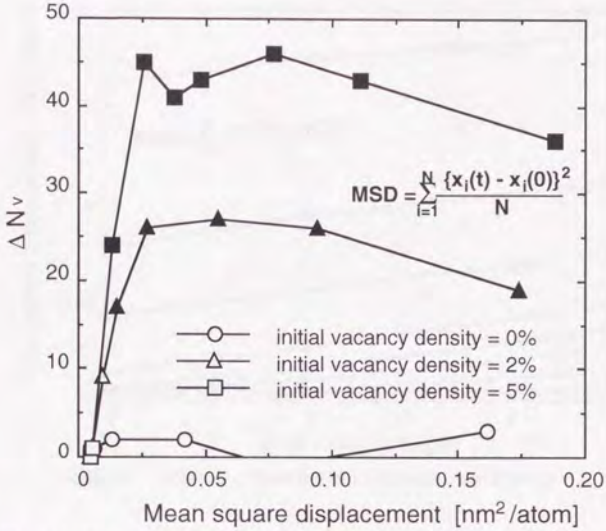

Fig. 4-6 **The relationship between MSD and net number of vacancies entering the cascade core during the cascades.**

deposition, the *MSD* is linearly increasing with increasing initial vacancy density. This indicates that atomic diffusion is enhanced by an introduction of vacancies. The enhancement of the *MSD*s is, hereafter, described as ΔMSD. ***Fig. 4-8*** is a plot of ΔMSD versus ΔN_v, showing a good correlation between them. The ΔMSD is a good scaling parameter for representing ΔN_v.

Even if the *MSD* is replaced by mixing efficiency (*ME*), the conclusion is the same. ***Fig. 4-9*** is a plot of initial vacancy density versus mixing efficiency (*ME*), showing an increase of the mixing efficiency with increasing initial vacancy density at higher energy deposition. ***Fig. 4-10*** represents a relationship between ΔN_v and ΔME given by the mixing efficiency enhanced by an introduction of vacancies, showing a good correlation between the two

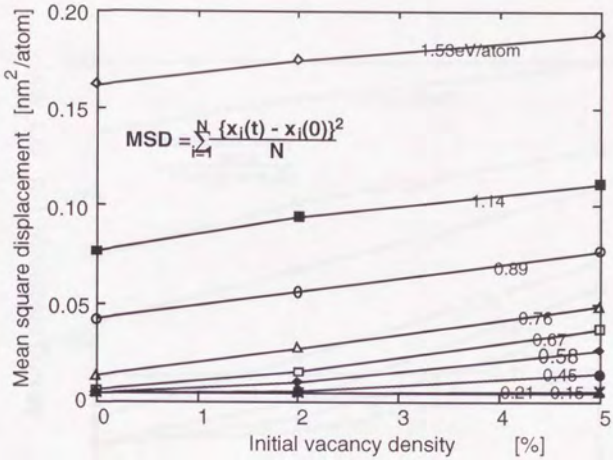

Fig. 4-7 **MSD as a function of initial vacancy density.**

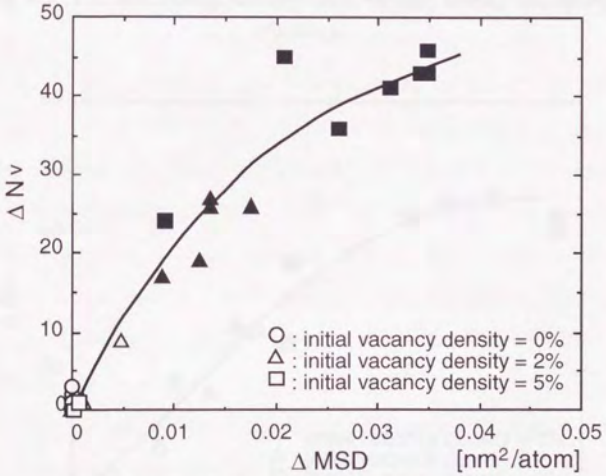

Fig. 4-8 **The relationship between ΔMSD and ΔN_v.**

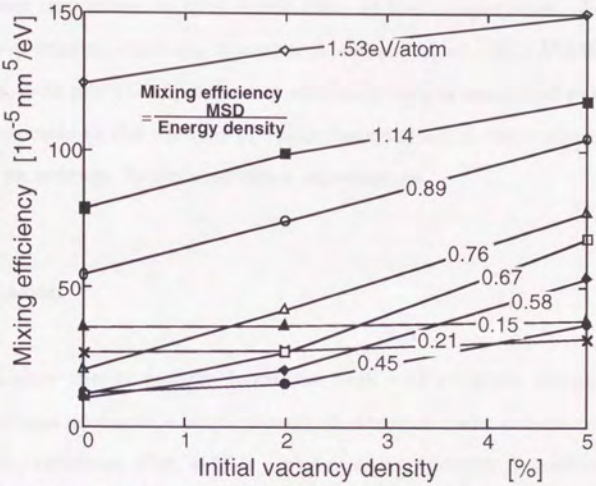

Fig. 4-9 **The relationship between initial vacancy density and mixing efficiency.**

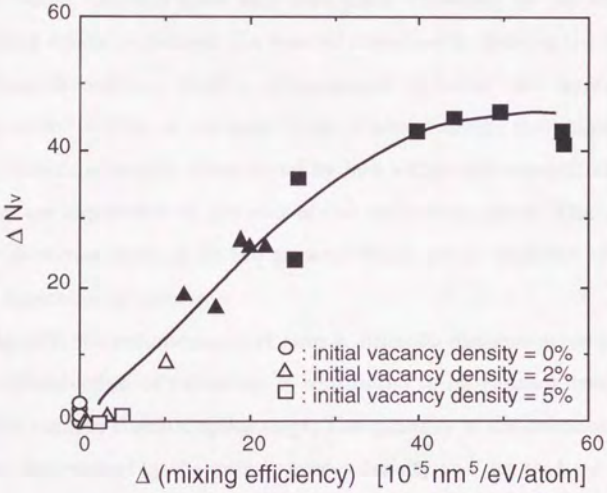

Fig. 4-10 **The relationship between ΔME and ΔN_V.**

parameters. Kim *et al.* performed [4-12] the experiments of ion-beam mixing using tracer impurities in thin metal films at low temperature, showing that the ion-mixing efficiency in copper is estimated as ~25.3 $Å^5$/eV/atom. Using ***Fig. 4-10*** and the experimental efficiency, ΔN_v is estimated to be ~30 that corresponds to the number of vacancies retained in the vacancy loop observed, on average, in ion-irradiation experiments.

4-4 Discussion

With higher energy density deposition than ~0.5 eV/atom, the agitated cascade volume produces a large amount of athermal point defects and has a liquid-like structure. ***Fig. 4-11*** is a plot of energy density deposition and *MSD*, showing a initial loose increase followed by a steep increase with increasing energy density deposition. In the events within such steep increase region, thermal spike may take place. However, by the effect of surrounding crystal structure, the most of atoms settle down to the lattice in the cascade volume. Such a phenomenon is called the "correlated recombination" within a cascade [4-13]. Consequently, the number of survival defects is largely determined by how efficiently interstitials and vacancies are separated at the end of the collisional phase. The initial vacancy densities defined in the present work are a measure of such efficient separation of defects.

In ***Fig. 4-7***, the enhancement of atomic diffusion distance accompanied with an introduction of vacancies is considered to be vacancy transport during the cascade thermal spike stage. The quantity of the enhancement, ΔMSD, is determined by the initial vacancy density and the gradient of the straight lines in ***Fig. 4-7***. It is noted that the gradients does not depend much on energy density that ranges more than ~0.6 eV/atom. The ΔMSD is

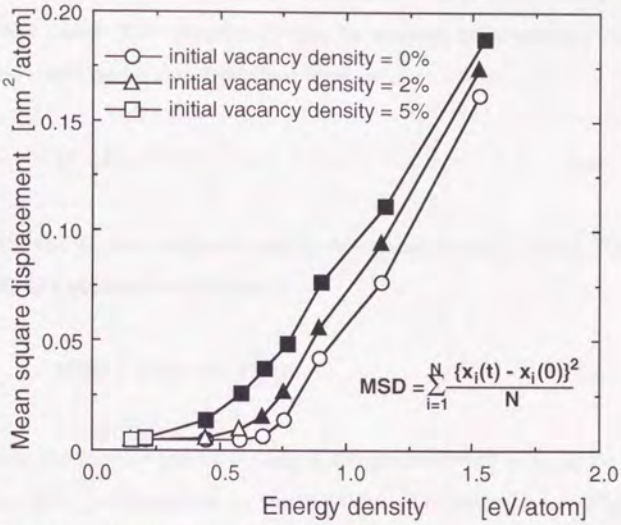

Fig. 4-11 **The relationship between energy density deposition and mean square displacement.**

determined by rather the initial vacancy density than the energy density deposition, although the absolute values of *MSD* are greater with increasing energy density deposition. Since the initial vacancy density defined in the present work is a measure of the efficient separation between displaced atoms and vacant lattice sites, it can be said that the essence of cascade collapse is the difference in atomic density between cascade molten zone and its surrounding crystal [4-11,14]. The difference may be brought by the *RCS*s and ballistic ejection of interstitial atoms during the collisional phase.

The *MSD* is generally described using the diffusion coefficient, D , as

$$MSD = 6Dt \quad , \tag{4.1}$$

where t is elapsed time which is, in the present study, constant (~20 psec) for all the cases. The quantity D can be written by a vacancy density dependent term and a non-dependent term, as

$$D = D_0 + D_v C_v \ , \tag{4.2}$$

where D_0 and D_v are constants and C_v is vacancy density. Using Eqs (4.1) and (4.2), one obtains the MSD as

$$MSD = 6(D_0 + D_v C_v)t \ . \tag{4.2}$$

If one take the initial vacancy density in the present work as C_v in Eq. (4.2), the term, $6D_v t$, corresponds to the gradient of straight-line in ***Fig. 4-7***. From ***Fig. 4-7***, the coefficient, D_v, is found to equal 5.8 x 10^9 nm^2/sec, approximating the coefficient of vacancy diffusion at the melting temperature of copper, 2.1 x 10^9 nm^2/sec. It might suggest that greater collapse probability is expected in metals with higher vacancy diffusion coefficient at the melting temperature of target material, since ΔMSD is expected to increase with increasing gradient, D_v, as schematically shown in ***Fig. 4-12***.

4-5 Summary

The mechanisms of cascade collapse were investigated using molecular dynamics technique. The difference in atomic density between the molten zone and the surrounding crystal is essentially important for cascade collapse.

Vacancy transport during the cascade thermal spike stage is determined by ΔMSD, the enhancement of mean square displacement due to an introduction of vacancies into the cascade volume. The ΔMSD is largely related with the coefficient of vacancy diffusion at the melting point of the material, strongly depending on initial vacancy density rather than deposited energy density.

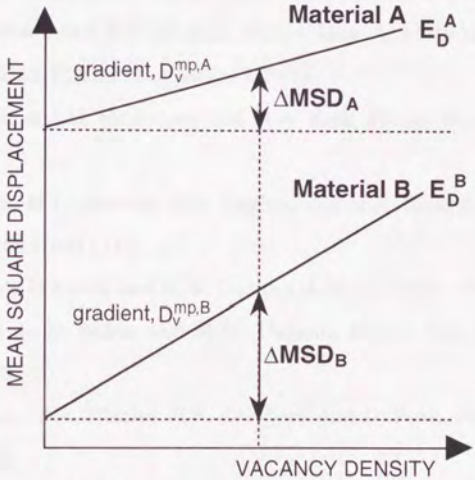

Fig. 4-12 **Schematic view of the relationship between initial vacancy density and mean square displacement. Higher ΔMSD is expected in metals with higher diffusion coefficient at the melting temperature.**

References 4

[4-1] C.A. English, J. Nucl. Mater. 134 (1985) 71.

[4-2] M.A. Kirk, I.M. Robertson, M.L. Jenkins, C.A. English, T.J. Black and J.S. Vetrano, J. Nucl. Mater. 21 (1987) 149.

[4-3] C.A. English and M.L. Jenkins, Mater. Sci. Forum 15-18 (1987) 1003.

[4-4] M.L. Jenkins, C.A. English and B.L. Eyre, Philos. Mag. 38 (1987) 97.

[4-5] W.J. Phythian, B.L. Eyre, D.J. Bacon and C.A. English, Philos. Mag.

[4-6] M.T. Robinson and M.L. Jenkins, Philos. Mag. A43 (1981) 999.

[4-7] M.L. Jenkins, Philos. Mag. 29 (1974) 813.

[4-8] J.S. Vetrano, I.M. Robertson and M.A. Kirk, Philos. Mag. A68 (1993) 381.

[4-9] T.J. Black, M.L. Jenkins, C.A. English and M.A. Kirk, Proc. Roy. Soc. Lond. A409 (1987) 177.

[4-10] T. Diaz de la Rubia and M.W. Guinan, J. Nucl. Mater. 174 (1990) 151.

[4-11] T. Diaz de la Rubia and M.W. Guinan, Mater. Sci. Forum 97-99 (1992) 23.

[4-12] S.-J. Kim, M-A. Nicolet, R.S. Averback and D. Peak, Phys. Rev. B37 (1988) 38.

[4-13] S.J. Zinkle and B.N. Singh, J. Nucl. Mater. 199 (1993) 173.

[4-14] R.S. Averback, T. Diaz de la Rubia, H. Hsieh and R. Benedek, in: Int. Conf. on Ion Beam Modification of Materials (Knoxvville, TN, 1990) to be published in Nucl. Instr. & Meth. B.

Chapter 5

RELATIONSHIP BETWEEN COLLISIONAL PHASE DEFECT DISTRIBUTION AND CASCADE COLLAPSE EFFICIENCY

5-1 Introduction

Changes in the microstructure of the neutron- and ion-irradiated materials depend on the production and subsequent behavior of defects as functions of irradiation conditions, e.g., recoil energies, irradiation temperature and the physical properties of target material. Many features impacting the role of defects in microstructural change are set forth during the cascade collisional phase, during which the cascade structure, including the number, size, energy density and spacing of subcascades, is almost established. Since the collisional phase consists of relatively high energy atomic collisions, it is well described using the binary collision approximation (BCA) [5-1]. Heinisch and Singh [5-2] simulated the structure of high energy cascades caused by primary recoil atoms (PKAs) of energies up to 1 MeV in a number of pure metals using the computer simulation code MARLOWE [5-1], which is based on the binary collision

approximation (BCA). In that work the number and spacing of subcascades were determined within the framework of collision physics as functions of atomic number, atomic mass and crystal structure. The analysis relied heavily on the concept of defect density to identify subcascades. The implicit assumption was made that the spatial density of vacant sites at the end of the collisional phase is directly related to the deposited energy density, and that regions of sufficiently high vacancy density correspond to areas where TEM-visible clusters are produced. Comparisons were made between their simulated subcascades and TEM images of 14 MeV neutron-irradiated metal foils. In copper there is remarkably good agreement between the observed number of clusters per group and the simulated number of subcascades per recoil. However, in gold there are more than ten times as many clusters observed as subcascades per recoil calculated in the simulation. From these comparisons it was concluded that multiple TEM-visible vacancy clusters could be associated with a single subcascade. The number of visible clusters per subcascade was found to increase with atomic mass.

There is experimental evidence [5-3~12] that cascade defects collapse to form visible vacancy clusters directly in the cascade region, even at extremely low temperature where vacancies cannot migrate to form a cluster. Many experiments involving the ion-irradiation of thin metal foils have determined the cascade collapse efficiency, reporting the "defect yield", the number of TEM-visible vacancy clusters produced per incident ion. The ion-irradiation experiments offer an opportunity to compare BCA simulations of high energy cascades with TEM observations for heavy-ion irradiations, including self-ions. As shown in *chapter 3*, the localization of defect distribution in the collisional phase governs the direct defect cluster formation in cascades. Moreover, in *chapter 4*, the essence of cascade

collapse is the difference in atomic density between cascade molten zone and surrounding crystal. The present study is undertaken to determine if the spatial localization of cascade defects at the end of the collisional phase, as represented by the density of vacant sites, correlates with the production of TEM-visible vacancy clusters. The objective of the present work is to examine if a "critical density" for cascade collapse can be identified, and if so, to study the dependence of the critical densities on the physical properties of target elements.

The spatial local densities of vacant lattice sites determined in this work represent local atomic displacements, assumed to be a measure of the difference in atomic density between cascade molten zone and surrounding crystal. The "vacancy densities" here are not intended as a quantitative measure of the density of stable vacancies produced in a cascade, which in any case do not exist until the thermal energy dissipates after the collisional phase.

5-2 Procedure

Ion-irradiations in Au, Ag, Cu, Ni, Fe, Mo and W are simulated using the MARLOWE, the well-known binary collision computer code of Robinson and Torrens [5-1]. In the MARLOWE, the trajectories of two atoms interacting according to a conservative central repulsive force are shown in ***Fig. 5-1***. The equations of motion representing these trajectories can be described in using the following relations for the barycentric scattering angle

$$\theta = \pi - 2s \int_R^{\infty} dr \; [\{g(r)\}^{-1} - (1 - \frac{s^2}{r^2})^{-1/2}] \; , \qquad (5.1)$$

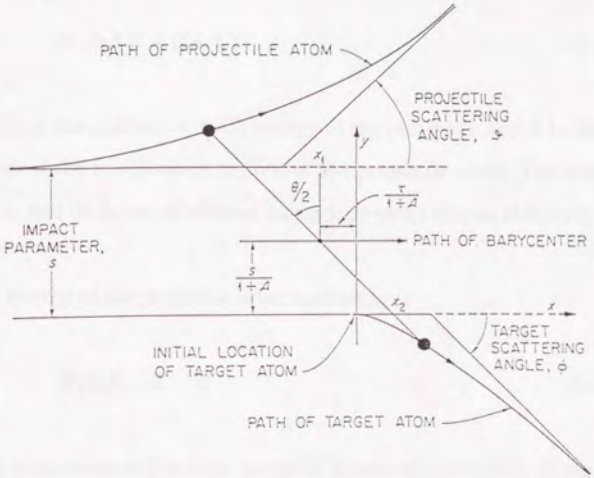

Fig. 5-1 **Laboratory trajectories of two particles interacting according to a conservative central repulsive force. The positions of the particles and of the barycenter are shown at the apsis of the collision.**

and for time integral

$$\tau = (R^2 - s^2)^{1/2} - \int_R^{\infty} dr \; [\{g(r)\}^{-1} - (1 - \frac{s^2}{r^2})^{-1/2}] \; , \qquad (5.2)$$

where s is the impact parameter, E_r is the relative kinetic energy, r is the interatomic separation, $V(r)$ is the potential of interatomic force, R is the apsis of the collision defined by $g(R) = 0$ and

$$g(r) = [1 - s^2/r^2 - V(r)/E_r]^{1/2} \; . \qquad (5.3)$$

The relative kinetic energy is

$$E_r = A E_0 / (1 + A) \ , \tag{5.4}$$

where E_0 is the incident kinetic energy of the projectile and A is the ratio of the mass of the target atom to that of the projectile atom. The integrals in Eqs (5.1) and (5.2) are evaluated using four-point Gauss-Mehler quantities [5-13].

The energy of the projectile after scattering is

$$E_1 = E_0 - T - Q \ . \tag{5.5}$$

Impact-parameter-dependent inelastic losses are included using Firsov's theory [5-14], which is described as

$$Q = \alpha / (1 + \beta p)^5 \ , \tag{5.6}$$

where

$$\begin{aligned} \alpha &= 0.05941 \, (Z_1 + Z_2)^{5/3} (E_0 / M_1)^{1/2} \quad [eV], \\ \beta &= 0.3042 \, (Z_1 + Z_2)^{1/3} \qquad [\text{Å}^{-1}], \end{aligned} \tag{5.7}$$

and p is the nearest neighbor collision distance.

Interatomic interaction for colliding atoms is described by the screened Coulomb potential;

$$V(r) = \frac{Z_1 Z_2}{r} e^2 f(r) \ , \tag{5.8}$$

where r is the distance between two nuclei, Z_1e and Z_2e are nuclear charges and $f(r)$ is the screening function. In the present calculation, the Moliere approximation [5-15] to the Thomas-Fermi screening function is employed, as follow;

$$f(r) = 0.35\exp(-0.3\frac{r}{a}) + 0.55\exp(-1.2\frac{r}{a}) + 0.10\exp(-6.0\frac{r}{a}), \quad (5.9)$$

where a is the screening radius that is usually chosen using Firsov expression [5-14], as follows;

$$a = \frac{0.8853a_0}{(Z_1^{1/2} + Z_2^{1/2})^{-2/3}} \quad (5.10)$$

Without changing the high-energy portion significantly, by adjusting the value of the screening radius, the Moliere function can be made to give a realistic description for interacting atoms at distances near the equilibrium separation of atoms. Torrens and Robinson [5-16] adjusted the screening radius so that the Moliere function gives the same value at the nearest-neighbor separation as a Born-Mayer potential fitted to elastic constants. Heinisch and Singh [5-2] chose the screening radius so that the Moliere approximation is equal to a pair potential fitted to elastic constants at the separation where the pair potential gives an energy of about a quarter of the displacement energy. In the present study, the screening radii are chosen according to the Torrens and Robinson's formalism, the Heinisch and Singh's formalism and Firsov's formalism, for gold, copper and iron, for silver, molybdenum and tungsten and for nickel, respectively. It is noted that high energy part of the Thomas-Fermi potential, which is important for

the present calculation, does not depend much on a choice of the screening radius.

Another important parameter setting of the MARLOWE code is cut-off energies below which atoms are no longer monitored. In the present calculation, the cut-off energy is set at the measured displacement energy for each metal [5-2,17,18,19].

The screening radii and the cut-off energies used in the present work are listed in ***Table 5-1***. The geometry of incident ion beam on target is set up to match the irradiation conditions of each experiment. More than one hundred ions are followed for each ion-target combination, and for each set of incident ions a beam divergence of 5-20 degrees is assumed, depending on how precisely the target geometry is described by the experimenter.

Table5-1 **MARLOWE parameter settings used in the present work.**

ELEMENTS	SCREENING RADIUS (Å)	CUT-OFF ENERGY (eV)
Au	0.0752	50
Ag	0.08167	39
Cu	0.0738	30
Ni	0.09716	40
Fe	0.0781	40
Mo	0.09126	65
W	0.08054	84

Defect distribution produced in a high energy cascade is spatially localized, forming so-called "subcascade" structure, as shown in ***Fig. 5-2***. Heinisch and Singh [5-2] first defined the subcascades based on collision physics and then determined the number of subcascades; however, the number does not always agree with experimental defect yields. Conversely, in the present study, the minimum vacancy density required for a cascade

to collapse into a TEM-visible vacancy cluster is determined using the defect distribution of the MARLOWE cascades and the experimental values of defect yield. To map the varying defect density distribution calculated by the MARLOWE code as shown in ***Fig. 5-2***, high density regions (*HDR*s) are identified for each cascade using a modified version of the subcascade identification scheme described in Ref. [5-2]. The procedure of *HDR* identification is as follows.

(1) The local density of vacancies within a small spherical volume with radius of third-nearest-neighbors is determined about each vacancy in cascades calculated using the MARLOWE code. Those vacancies with local densities above a given critical value are identified.

(2) The procedure of step (1) is repeated using only the set of vacancies identified in step (1). Each of the 'dense region' vacancies identified is associated with an *HDR*.

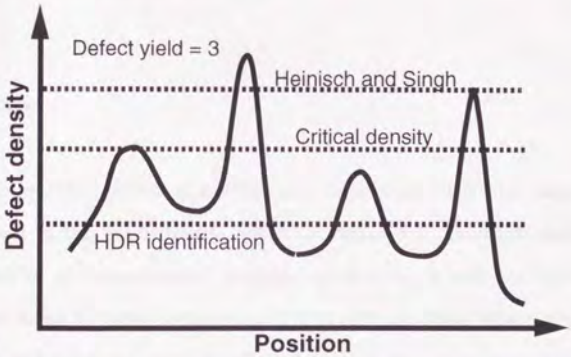

Fig. 5-2 **Defect distribution in a high energy cascade is spatially localized, having so-called "subcascade" structure. While Heinisch and Singh [5-2] defined the subcascades based on collision physics, in the present study, threshold vacancy density for cascade collapse, i.e., critical densities, are determined based on experimental defect yield values.**

The critical value used for identification of dense region defects is about twice as large as average local vacancy density (*ALVD*), which is defined as the average number of vacancies within third-nearest-neighbor distance around each vacancy. The *ALVD* is independent [5-2] of cascade energies in the range simulated in the present work. Thus, candidates of defect dense regions to collapse into TEM-visible vacancy clusters are chosen, as shown in ***Fig. 5-2***. An *HDR* does not represent a cascade *or* a subcascade that is defined by Heinisch *et al.* [5-2], *nor* does it represent a visible cluster *or* loop. The number of *HDR*s is nearly proportion to damage energies. The density of defects in an *HDR* is defined in this analysis as the occupation ratio of vacant lattice sites to lattice sites in a spherical volume of constant radius of $5a_0$. The vacancy densities of the *HDR*s for simulated cascades are distributed over a range of values, starting from the minimum value used to define the *HDR*s as shown in ***Fig. 5-3***.

5-3 Results

The calculated *HDR* densities are compared with the defect yields determined in the experiments listed in ***Table 5-2***. Thin foil metals have been used in all experiments adopted in this work and the experiments have been done at room temperature with low ion dose, where overlapping effects of cascades are considered to be neglected. It is assumed that the *HDR*s of higher density have a higher probability of resulting in a collapse into a TEM-visible vacancy cluster. The distribution of the *HDR* density values per ion is schematically represented in ***Fig. 5-3***, where the method of determining the critical vacancy density for cascade collapse is illustrated. The shaded area under the distribution curve, which corresponds to an

experimental defect yield value (i.e., TEM-visible clusters per ion), determines the critical density. It should be noted that the critical density obtained in this analysis is independent of the number of *HDR*s, i.e., the choice of parameter settings that were used to identify *HDR*s.

Table5-2 **Experimental yields of visible defects per ion (DYs) and the corresponding calculated critical densities (CDs) in the collisional phase for ion-irradiated metal foils.**

ENERGY(keV)	*ION*	*TARGET*	*DY*	*CD(%)*	*REFERENCE*
20	Au	Au	0.05~0.09	2.8~2.9	Sekimura [5-3]
50	Au	Au	0.39~0.46	2.8~3.1	Sekimura [5-3]
70	Au	(001) Au	1.0	1.9	Merkle [5-4]
100	Au	Au	1.11~1.25	1.6~1.8	Sekimura [5-3]
200	Au	Au	1.50~1.67	1.8~1.9	Sekimura [5-3]
300	Au	Au	1.71~1.86	2.0~2.1	Sekimura [5-3]
400	Au	Au	1.91~2.18	2.1~2.3	Sekimura [5-3]
30	Ag	(001) Ag	0.55	1.6	Shober [5-5]
50	Ag	(001) Ag	0.95	1.6	Shober [5-5]
30	Ag	Ag	0.50 *1)	1.7	Kiritani [5-6]
60	Ag	Ag	1.13 *1)	1.6	Kiritani [5-6]
100	Ag	Ag	1.60 *1)	1.6	Kiritani [5-6]
150	Ag	Ag	1.98 *1)	1.7	Kiritani [5-6]
30	Cu	(011) Cu	0.50±0.01	1.4	Stathopoulos [5-7]
90	Cu	(011) Cu	1.1±0.1	1.3~1.4	Stathopoulos [5-8]
30	W	(011) Cu	0.60±0.01	1.7~1.8	Stathopoulos [5-7]
90	W	(011) Cu	0.95±0.1	1.8~2.0	Stathopoulos [5-8]
50	Ni	(110) Ni	0.14±0.01	2.0~2.1	Robertson [5-9]
50	Kr	(110) Ni	0.21±0.02	2.1	Robertson [5-9]
80	Fe	Fe	~0.001*1,2)	4.1	Jenkins [5-10]
60	Mo	(011) Mo	0.12±0.02	2.6~2.8	English [5-11]
60	Sb	(011) Mo	0.15±0.02	2.8~3.0	English [5-11]
60	Xe	(011) Mo	0.20±0.02	2.7~2.8	English [5-11]
120	Sb	(011) Mo	0.29±0.02	2.6~2.9	English [5-11]
180	Sb	(011) Mo	0.35±0.02	2.6~2.8	English [5-11]
60	Au	W	0.1	4.1	Haussermann [5-12]

*1) DYs are quoted from figures in the literature
2) Not corrected for loop loss to irradiation surface

Figs 5-4(a)~(g) show the density distributions of *HDR*s for ion-irradiated pure metals. The vertical lines indicate the critical density values, i.e., the density value above which an *HDR* corresponds to a TEM-visible vacancy cluster. Calculated critical densities for each irradiation are given in ***Table 5-2***. The variation of critical densities in each irradiation is due to the quoted experimental error in defect yield values. The density distributions vary with ion energies as shown in ***Fig. 5-2***. However, it is noted that the critical densities are independent of incident ion energies for materials irradiated by the self- and similar-mass-ions. From these results it is clear that there is a threshold density in the collisional phase above which a visible vacancy cluster will be formed at the end of a cascade.

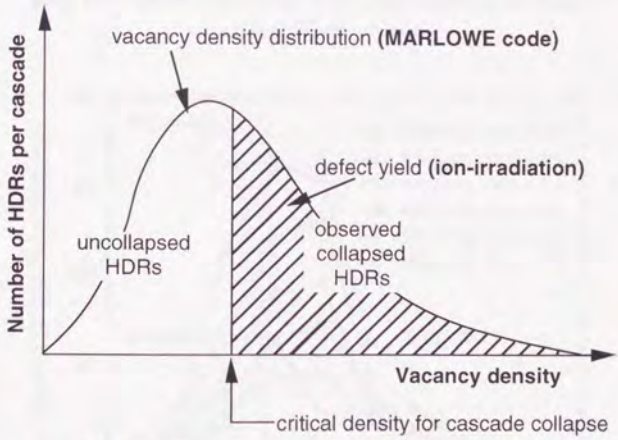

Fig. 5-3 **A schematic representation of the definition of critical density. A distribution of vacancy densities of high density regions (*HDR*s) in cascades is plotted. The shaded area represents the fraction of *HDR*s per ion that correspond to the observed visible vacancy clusters per ion. The vertical line thus indicates the critical density within an *HDR* for production of a visible vacancy cluster.**

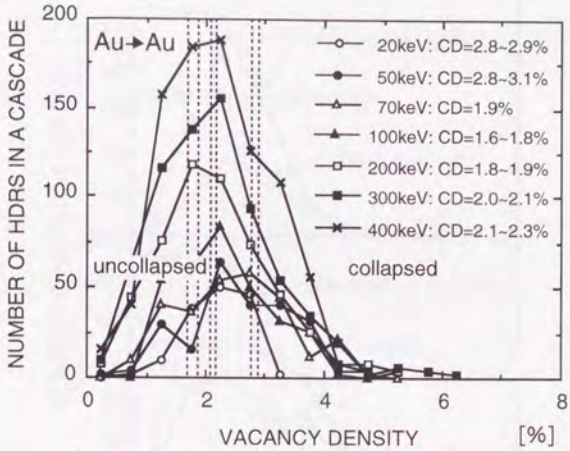

Fig. 5-4(a) **Distribution of *HDR* vacancy density in ion-irradiated gold. The vertical dashed lines in the figure indicate the range of critical density values.**

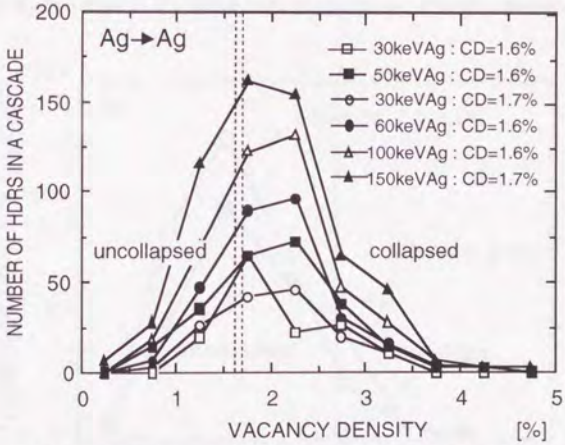

Fig. 5-4(b) **Distribution of *HDR* vacancy density in ion-irradiated silver. The vertical dashed lines in the figure indicate the range of critical density values.**

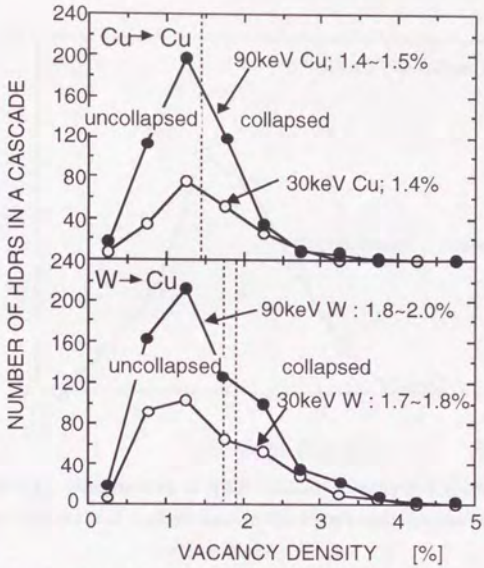

Fig. 5-4(c) **Distribution of *HDR* vacancy density in ion-irradiated copper. The vertical dashed lines in the figure indicate the range of critical density values.**

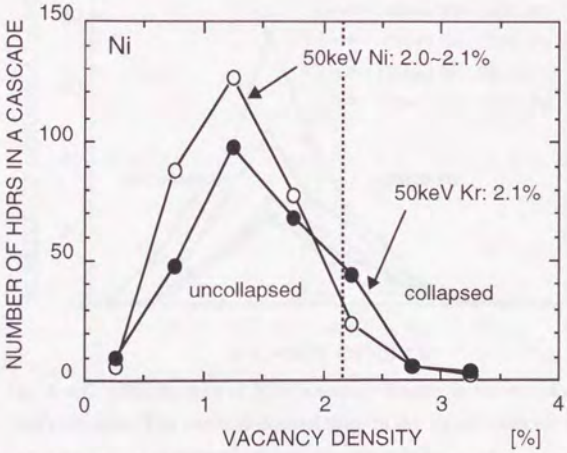

Fig. 5-4(d) **Distribution of *HDR* vacancy density in ion-irradiated nickel. The vertical dashed lines in the figure indicate the range of critical density values.**

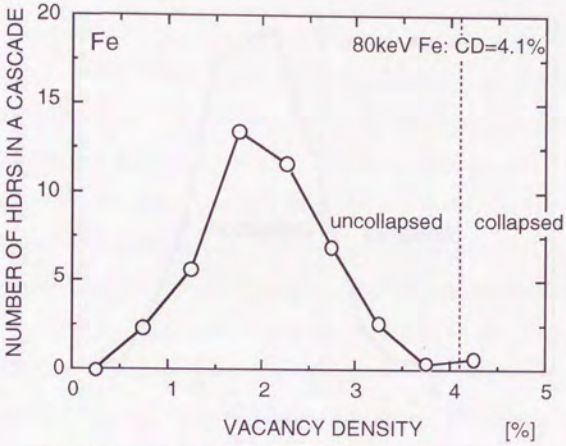

Fig. 5-4(e) **Distribution of *HDR* vacancy density in ion-irradiated iron. The vertical dashed lines in the figure indicate the range of critical density values.**

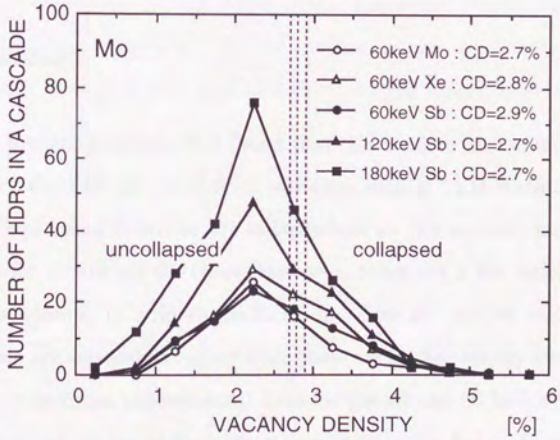

Fig. 5-4(f) **Distribution of *HDR* vacancy density in ion-irradiated molybdenum. The vertical dashed lines in the figure indicate the range of critical density values.**

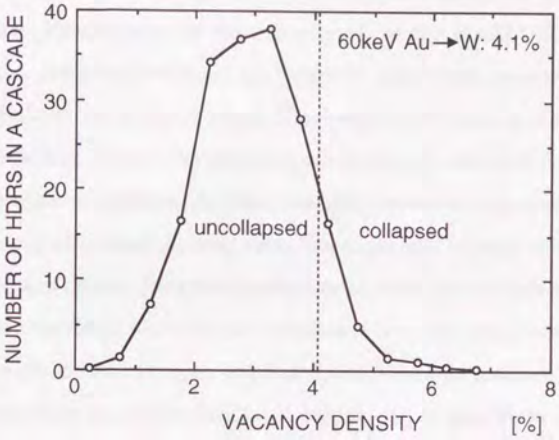

Fig. 5-4(g) **Distribution of *HDR* vacancy density in ion-irradiated tungsten. The vertical dashed lines in the figure indicate the range of critical density values.**

5-4 Discussion

In the present analysis, it is found that there exists the threshold value of vacancy density for cascade to collapse into a TEM-visible vacancy cluster. The critical densities are independent on the incident ion energies and mass for almost all the cases. However, there are a few exceptions for the independence. In gold the critical densities for the 20 and 50 keV irradiations are somewhat higher than those for higher energy irradiations. This may be because experimental data for the 20 and 50 keV irradiations are very limited, owing to their close proximity to the foil surface. Another exception is for copper, where the critical densities exhibit a slight dependence on ion mass. If the cascades with 1.4% density collapse in self-ion irradiated copper, why do they not collapse when produced by tungsten

ions? A possible reason is the influence of cascade shape on the cascade cooling rate. Examination of the aspect ratio of the MARLOWE cascade shows that cascades produced by tungsten ions have somewhat more elongated shape on average. Thus, they might cool off in a significantly shorter time than the self-ion cascades, requiring a higher initial density of defects to achieve collapse. Another possible reason for the exceptions to independence of critical density from ion mass and energy is the depth distributions of defects from the irradiation surface. The exceptions are the cases where the depth distribution is shallower from the irradiation surface. The critical densities in copper irradiated with tungsten ions are relatively higher than those in self-ion irradiated copper, and in gold there are higher critical densities in the 20 and 50 keV self-ion irradiations.

It may be possible to compare the critical densities for cascade collapse in different materials if some characteristic parameters of target materials that affect the defect mobility and defect transport during the cascade cooling phase are considered. In the previous chapter, we have obtained such a result that materials with higher vacancy diffusion coefficient at the melting temperature are expected to have a higher probability of collapsing. ***Fig. 5-5*** is a plot of the critical densities determined for the target materials for self- or similar-mass-ion irradiation versus the vacancy mobility defined as $D_v / k_B T_m$, where D_v is the vacancy diffusion coefficient at the melting temperature of each material, k_B is the Boltzmann constant and T_m is the melting temperature. D_v is calculated using vacancy migration energy, as follows,

$$D_v = \frac{1}{6}\delta^2 z \, \nu_0 \exp\left(-\frac{E_{1v}^m}{k_B T_{mp}}\right) , \qquad (5.11)$$

where, E_{1v}^{m} is the vacancy migration energy, T_{mp} is the melting temperature, k_B is the Boltzmann constant, ν_0 is the Debye frequency and δ is the nearest neighbor distance between the atoms of target materials. These parameters used in the present work are listed in ***Table 5-3***. Vacancy migration energies are quoted from Ref. [5-20] for gold, silver, copper and molybdenum, Ref. [5-21] for nickel, Ref. [5-22,23] for iron and Ref. [5-24] for tungsten. Since the abscissa is represented by using the lattice constant, a_0, the critical densities in this figure are given in terms of the number of vacancies in a unit cell with volume in cubic lattice constants. Except for iron, a strong correlation between the critical densities and the vacancy mobility is clearly seen. The critical densities are lower in the cases where greater defect transport can take place.

For iron, the estimated critical density is much greater than that expected from a trend in ***Fig. 5-5***. If the correlation in ***Fig. 5-5*** is correct, why is the critical density for iron overestimated? This is probably because the published defect yield for iron employed in the present study was not corrected for loss of clusters by glide to the irradiation surface [5-10]. This cluster loss to the surface probably takes place in the metals with high stacking fault energy [5-11]. Jenkins *et al.* [5-10] discussed the cluster loss

Table5-3 **The Debye's frequencies and vacancy migration energies employed in the present work.**

ELEMENTS	Debye's frequency ν_0(sec $^{-1}$)	Vacancy migration energy E_{1v}^{m}(eV)
Au	3.44×10^{12}	0.83
Ag	4.70×10^{12}	0.66
Cu	7.15×10^{12}	0.71
Ni	9.37×10^{12}	1.25
Fe	9.79×10^{12}	0.55
Mo	9.37×10^{12}	1.3
W	8.34×10^{12}	2.02

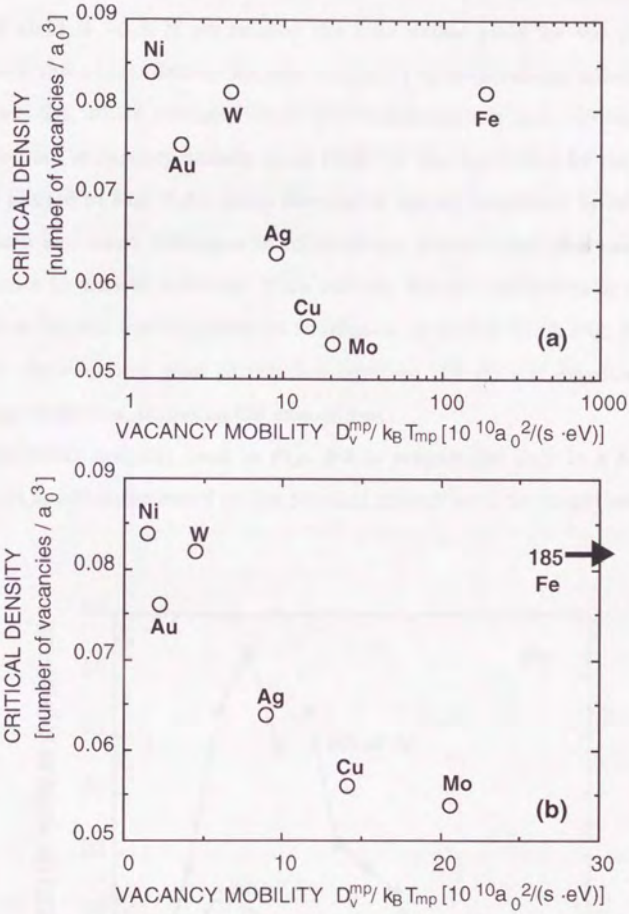

Fig. 5-5 **Critical density values determined in the present analysis versus vacancy mobility in each metal near the melting temperature. Metals with higher vacancy mobility have smaller critical densities. The abscissas are (a) a logarithmic scale and (b) a linear scale.**

to the surface and estimated true defect yield in iron irradiated by 80 keV tungsten (not by self-ion). It is estimated to be ~0.9, while the measured defect yield is ~0.2. If we employ the true defect yield for the present analysis, the critical density for iron irradiated by tungsten-ion is evaluated as about 2%, which corresponds to 0.04 vacancies in a unit volume. (The distribution of vacancy density in an *HDR* for iron irradiated by tungsten-ion is plotted in ***Fig. 5-6***.) As is the case of copper irradiated by self- and tungsten-ion, large difference in incident ion masses may give rise to an difference in critical densities. If we assume that the difference in critical densities for self- and tungsten-ion irradiation on iron is small, ***Fig. 5-5*** will clearly show a very good correlation between the critical densities and vacancy mobilities, including the case of iron.

The defect mobility used in ***Fig. 5-5*** is meaningful only in a relative sense. It is estimated based on the physical properties of the target material

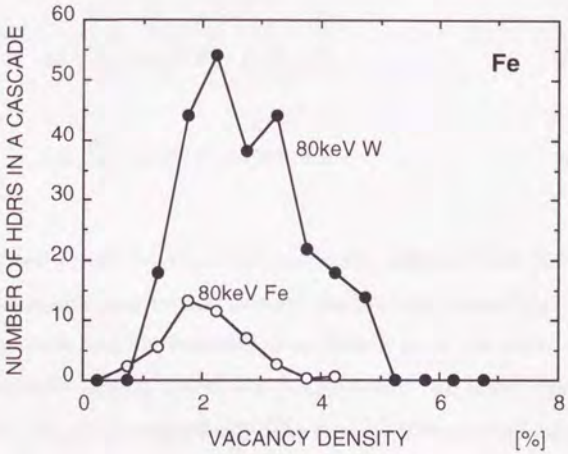

Fig. 5-6 **Comparison of the distributions of *HDR* vacancy densities in ion-irradiated iron.**

in the solid state. Molecular dynamics computer simulation [5-25] shows a liquid-like structure at molten zone in cascade core during the thermal spike stage. However, the physical arguments of the liquid state may not be applicable to describing the cascade cooling phase. Perhaps a more precise description of vacancy transport in the cascade cooling phase is required for an appropriate correlation with critical densities in different materials.

Thermal spike lifetime may also play an important role on the cascade collapse [5-26]. The lifetime is strongly related to electron-phonon coupling in metals [5-27] and the melting temperature of target materials. A more important factor is defect transport in the cooling phase including the effect of the lifetime. However, the effect is not incorporated into the defect mobility of ***Fig. 5-5***.

Simultaneous equations of thermal conductivity can be described for the electronic and lattice system, as follows.

$$\rho_0 C_e \frac{\partial T_e}{\partial t} = \kappa_e \nabla^2 T_e - G(T_e - T_l) \tag{5.12}$$

$$\rho_0 C_l \frac{\partial T_l}{\partial t} = \kappa_l \nabla^2 T_l + G(T_e - T_l) \tag{5.13}$$

where T_e and T_l are the electronic and lattice temperatures (K), κ_e and κ_l are the electronic and lattice thermal conductivity (J/sec/K/m), G is the electron-phonon coupling constant (J/sec/K/m^3), ρ_0 is the molar density of atoms (mol/m^3), and C_e and C_l are the electronic and lattice specific heat coefficients (J/mol/K), respectively. The electron-phonon coupling constant, G, is estimated based on the electronic thermal relaxation model of Allen [5-

28]. If electrons in a metal are heated, the electron-phonon interaction causes temperature relaxation

$$\frac{d\,T_e}{d\,t} = \gamma_T\,(T_l - T_e)\ , \tag{5.14}$$

where γ_T is described as

$$\gamma_T = \frac{3\hbar\,\lambda < \omega^2 >}{\pi\,k_B\,T_e}\ . \tag{5.15}$$

The dimensionless electron-phonon coupling parameter, λ, is derived from experimental resistivity measurement.

$$\begin{aligned}\lambda &= \frac{\hbar\,\Omega_p^2}{8\pi^2}\,\frac{\rho}{k_B T}\,F_{th} \\ &= (0.8422\times 10^{-3}\,\{\rho\,(\mu\Omega cm)\}\,[\{\Omega_p\,(eV)\}^2]\,F_{th}\ ,\end{aligned} \tag{5.16}$$

where, Ω_p is the Drude-Plasma energy [5-29], F_{th} is the correction factor [5-29] and ρ is the electronic resistivity to be measured by experiments. The values of λ [5-28] used in the present work are listed in ***Table 5-3***. The average of the square of phonon frequency, $<\omega^2>$, is described as [5-30]

$$\begin{aligned}<\omega^2> &= \int d\,\omega\,\omega\,\alpha^2(\omega)F(\omega) / \int d\,\omega\,\alpha^2(\omega)\frac{F(\omega)}{\omega} \\ &\cong \int d\,\omega\,\omega\,F(\omega) / \int d\,\omega\,\frac{F(\omega)}{\omega}\ ,\end{aligned} \tag{5.17}$$

where, $F(\omega)$ is the density of states of phonon, which is estimated simply using the Debye's model in the present study. The dimensionless electron-phonon coupling parameter, λ, and the electron-phonon coupling constant, G, employed in this work are listed in ***Table 5-4***.

Table5-4 **Electron-phonon coupling constant estimated using Allen's model.**

ELEMENTS	λ	G (J/sec/K/m^3)	γ_T (=G/ρ_0C$_e$) (1/sec)
Au	0.15	1.87×10^{16}	2.55×10^{14} / T_e
Ag	0.12	2.26×10^{16}	3.81×10^{14} / T_e
Cu	0.13	9.27×10^{16}	9.56×10^{14} / T_e
Ni	0.31	$422. \times 10^{16}$	39.1×10^{14} / T_e
Fe	0.34	$330. \times 10^{16}$	46.9×10^{14} / T_e
Mo	0.32	85.7×10^{16}	40.4×10^{14} / T_e
W	0.26	35.4×10^{16}	26.0×10^{14} / T_e

To investigate the temperatures profile in a spherical cascade, the simultaneous equations, (5.12) and (5.13), are solved using the finite difference method (*FDM*). In practice, the central difference scheme of the *FDM* is applied to the calculations, and calculation system is represented by spherical coordinate. The width of mesh is 1 nm. Since the parameter C_e depends on the electronic temperature, the electronic specific heat at time t=(k+1)Δt, $C_e\{(k+1)\Delta t\}$, is required when one calculates the temperatures at time t=(k+1)Δt. In the present study, the following "predictor-corrector" method is applied to this problem.

(1) $C_e\{(k+1)\Delta t\}$ is first predicted using the parameter settings at time t=kΔt.

(2) The new $C_e\{(k+1)\Delta t\}$ is obtained using newly obtained parameter settings.

(3) After several iterations of step (2), the corrected $C_e\{(k+1)\Delta t\}$ is obtained. Then the temperatures at time t=(k+1)Δt are obtained using the corrected electronic specific heat.

Boundary condition employed here is as follows,

$$\frac{d\,T_e}{d\,r} = 0 \text{ and } \frac{d\,T_l}{d\,r} = 0 \qquad \text{at } r=0 \qquad (5.18)$$

$$T_e = T_{amb} \text{ and } \frac{d\,T_l}{d\,r} = 0 \qquad \text{at } r=r_{max} \qquad (5.19)$$

and initial condition ($t=0$) is as follows,

$$T_e(r) = T_{amb} \text{ and } T_l(r) = T_0 \exp\left(-\frac{r^2}{R^2}\right) + T_{amb} \quad . \qquad (5.20)$$

where, T_{amb} is an ambient temperature and R is the characteristic length of a cascade. As shown in Eq. (5.20), initial lattice temperature profile is Gaussian distribution, which is the solution of thermal conductivity equations with an initial condition of the three-dimensional delta function [5-31]. In the present calculations, T_0, T_{amb} and R are 3500K, 300K and 5nm, respectively. ***Figs 5-7 (a)~(g)*** show the time development of the electronic and lattice temperatures at $r=0$ in each metal, when the same amount of energy is deposited. For gold, silver and copper, where the lattice system is weakly coupled with the electronic system, the electronic temperatures remain constant. However, for the other metals, where the lattice is strongly coupled with the electrons, the electronic temperatures show a rapid increase followed by a decrease with increasing time.

The total jump number of vacancies in the cascades is evaluated using the lattice temperature changes in ***Figs 5-7***. The jump number is defined as

$$\text{(Total vacancy jump)} = \sum_i z\ \nu_0 \exp\left(-\frac{E_{mv}}{k_B T_l(t_i)}\right) \Delta t \qquad (5.21)$$

where, z is the number of jump sites (i.e., $z=12$ for fcc and $z=8$ for bcc), ν_0 is

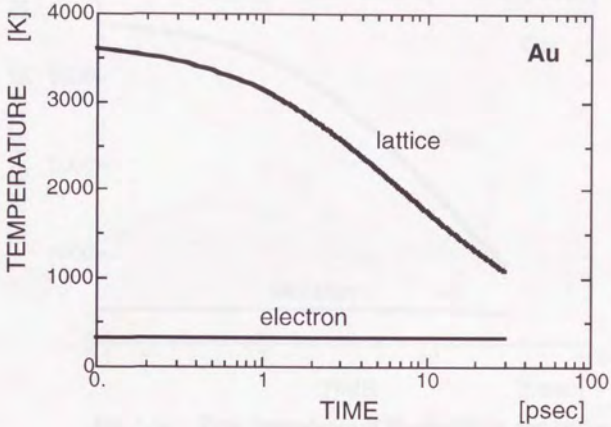

Fig. 5-7(a) **Time dependence of the electronic and lattice temperatures during the thermal spike phase in gold.**

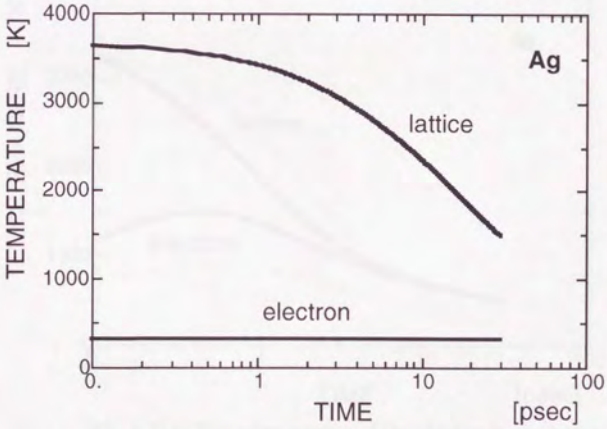

Fig. 5-7(b) **Time dependence of the electronic and lattice temperatures during the thermal spike phase in silver.**

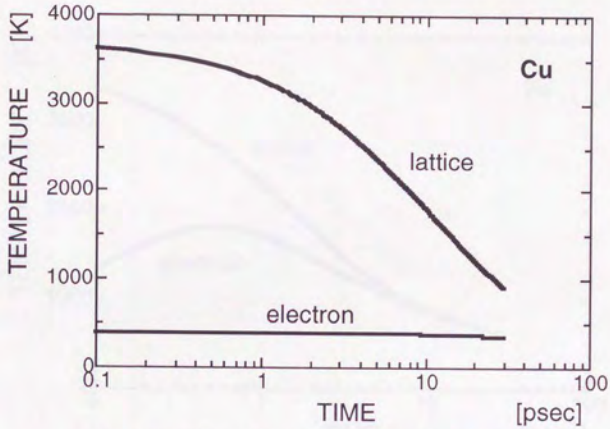

Fig. 5-7(c) **Time dependence of the electronic and lattice temperatures during the thermal spike phase in copper.**

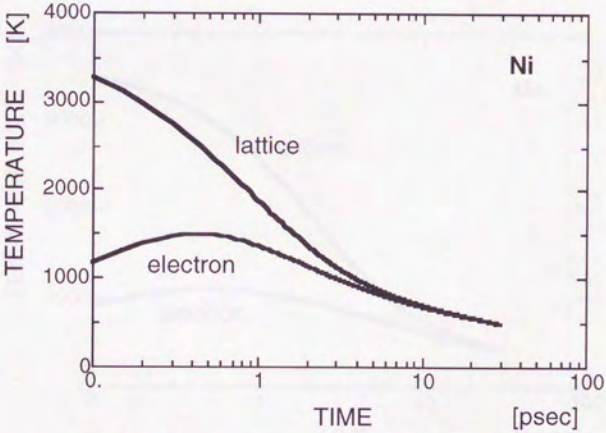

Fig. 5-7(d) **Time dependence of the electronic and lattice temperatures during the thermal spike phase in nickel.**

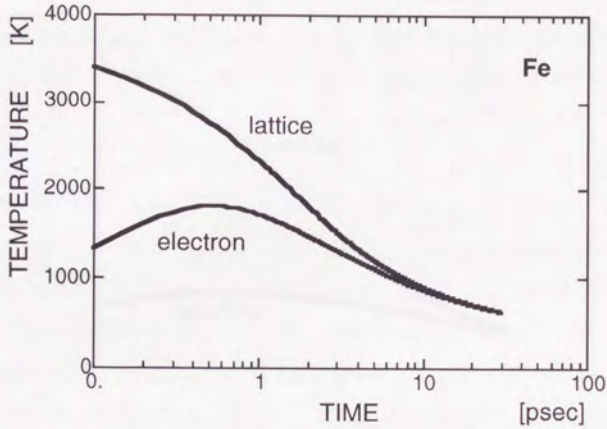

Fig. 5-7(e) **Time dependence of the electronic and lattice temperatures during the thermal spike phase in iron.**

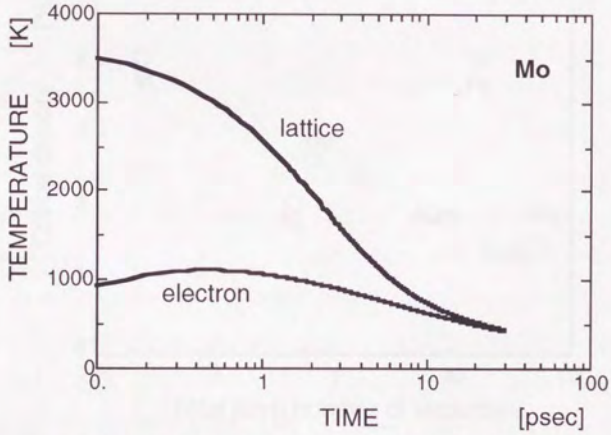

Fig. 5-7(f) **Time dependence of the electronic and lattice temperatures during the thermal spike phase in molybdenum.**

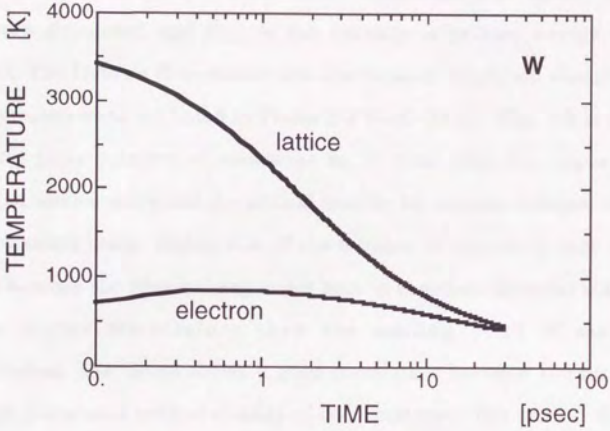

Fig. 5-7(g) **Time dependence of the electronic and lattice temperatures during the thermal spike phase in tungsten.**

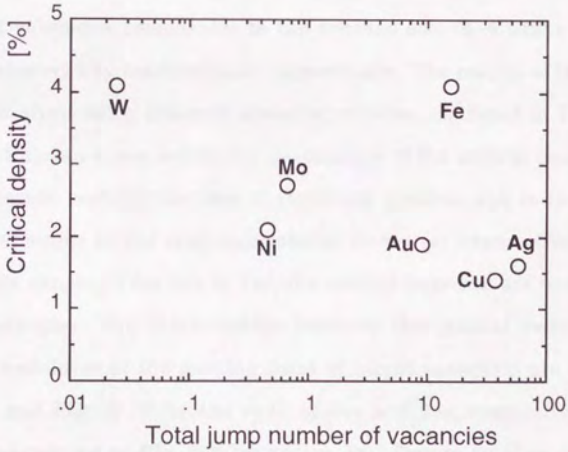

Fig. 5-8 **Critical density values determined in the present analysis versus the number of vacancy jumps in the cascades deposited with kinetic temperature of 3500 K.**

the Debye's frequency, $T_l(t_i)$ is the lattice temperature at time t_i, Δt is the time step simulated and E_{mv} is the vacancy migration energy of each element. The Debye's frequencies and the vacancy migration energies used in the present work are listed in ***Table 5-3*** [5-20~24,32]. ***Fig. 5-8*** is a plot of the total jump number of vacancies in 30 psec after the deposition of Gaussian temperature and the critical density for cascade collapse obtained in the present work. Estimation of the number of vacancy jumps is quite rough, because the physical argument here is based on the solid state even at the higher temperature than the melting point of materials. Nevertheless, the figure shows a good correlation between the number of vacancy jumps and critical density of each material. The critical densities are lower in the cases where greater vacancy transport can take place.

In the critical density analysis described so far, the radius of sampling volume employed for defining the densities is fixed at $5a_0$, because this sampling volume is comparable to the average size (3~4 nm) of vacancy clusters observed by ion-irradiation experiments. The results of the critical density analysis using different sampling volumes are listed in ***Table 5-5***. When radius $3a_0$ is employed, the fluctuations of the critical densities are slightly larger probably because of statistical problem due to the smaller number of atoms in the sampling volume. However, irrespective of using any radius ranging from $3a_0$ to $7a_0$, the critical densities are independent on ion energies. The relationships between the critical densities and vacancy mobilities at the melting point of target materials are shown in ***Fig. 5-9*** and ***Fig. 5-10*** for the radii of $3a_0$ and $7a_0$, respectively. These figures correspond to ***Fig. 5-5*** for radius $5a_0$. Due to smaller number of sampling atoms in the sampling volume, the correlation is not so good for radius $3a_0$. However, except for the case of iron because of the same reason described above, it is still found that the critical densities are lower in the

cases where greater vacancy transport is expected to take place, whenever one employs any sampling radius ranging from $3a_0$ to $7a_0$.

Table5-5 **The dependence of calculated critical densities (CDs) in the collisional phase on the sampling volume of high dense region (HDR).**

Target	Ion (keV)	Critical density		
		$3a_0$	$5a_0$	$7a_0$
Au	20 Au	6.4~6.9	2.8~2.9	1.3
	50 Au	4.6~4.9	2.8~3.1	1.8
	70 Au	2.9	1.9	1.1
	100Au	2.2~2.9	1.6~1.8	1.1~1.2
	200Au	2.9~3.1	1.8~1.9	1.1~1.2
	300Au	3.5~3.8	2.0~2.1	1.3
	400Au	3.8~4.0	2.1~2.3	1.4~1.5
Ag	30 Ag	3.1	1.6	0.85
	50 Ag	2.9	1.6	0.92
	30 Ag	3.5	1.7	0.97
	60 Ag	2.7	1.6	0.96
	100 Ag	2.9	1.6	0.97
	150 Ag	3.1	1.7	1.0
Cu	30 Cu	3.1	1.4	0.80~0.85
	90 Cu	2.7~3.1	1.3~1.4	0.75~0.82
	30 W	3.8	1.7~1.8	1.0
	90 W	3.5~3.8	1.8~2.0	1.1~1.2
Ni	50 Ni	4.2~4.4	2.0~2.1	1.2
	50 Kr	3.8	2.1	1.2~1.3
Fe*1)	80 Fe	10.2	4.1	2.3
Mo	60 Mo	5.7~6.2	2.6~2.8	1.5~1.6
	60 Sb	5.7~6.2	2.8~3.0	1.6~1.8
	60 Xe	5.7~6.2	2.7~2.8	1.5~1.6
	120 Sb	5.7~6.2	2.6~2.9	1.5~1.7
	180 Sb	6.2	2.6~2.8	1.6~1.8
W	60 Au	8.4	4.1	2.5

*1) A defect yield value emplyed in the present study is not corrected for loop loss to irradiation surface.

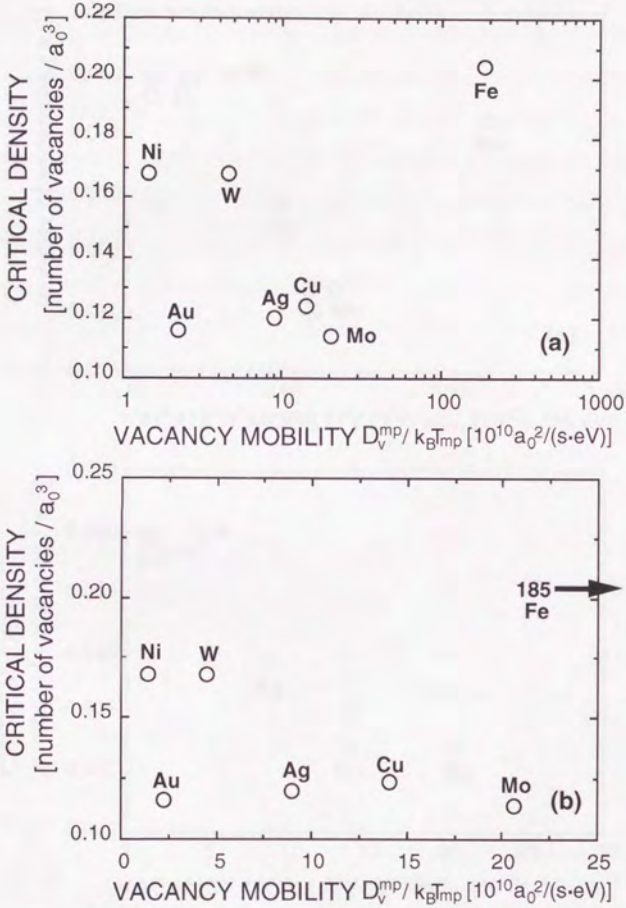

Fig. 5-9 **Critical density values determined in the present analysis using radius of $3a_0$ versus vacancy mobility in each metal near the melting temperature. The abscissas are (a) a logarithmic scale and (b) a linear scale.**

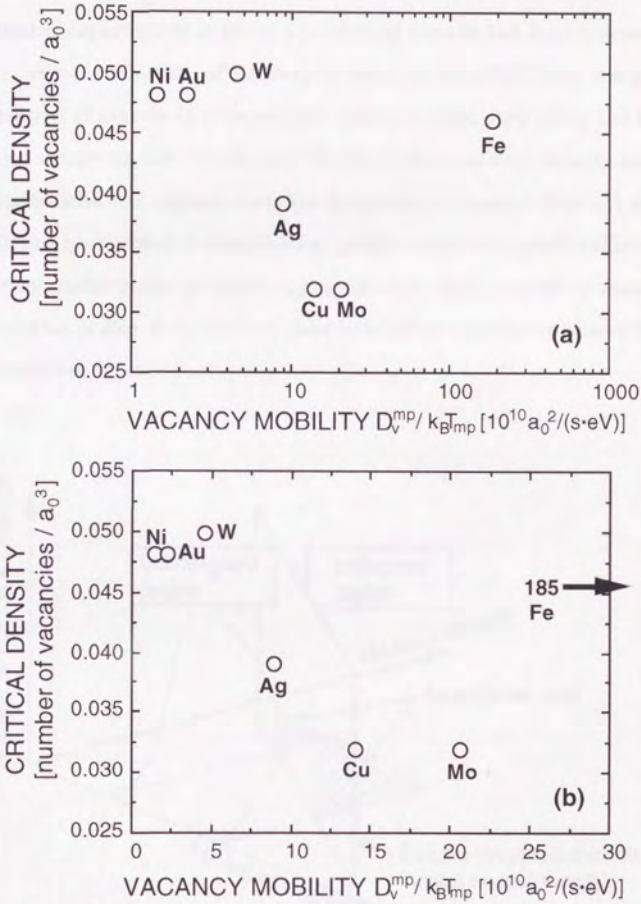

Fig. 5-10 **Critical density values determined in the present analysis using radius of $7a_0$ versus vacancy mobility in each metal near the melting temperature. The abscissas are (a) a logarithmic scale and (b) a linear scale.**

A schematic representation of the way to predict cascade collapse efficiencies is shown in ***Fig. 5-11***. The defect yield to be measured by ion-irradiation experiments is given as a shaded area in the figure, depending on; (1) the distribution of vacancy density in an *HDR* (i.e., the spatial localization of atomic displacements), which is calculated using the binary collision computer simulation, and (2) the critical vacancy density strongly associated with the vacancy mobility or vacancy transport of target metals. The figure is expected to enable us to predict the defect yield values in an arbitrary metal under an arbitrary irradiation field. In such a sense, the shaded area in ***Fig. 5-11*** can be a good irradiation correlation parameter for the cascade collapse.

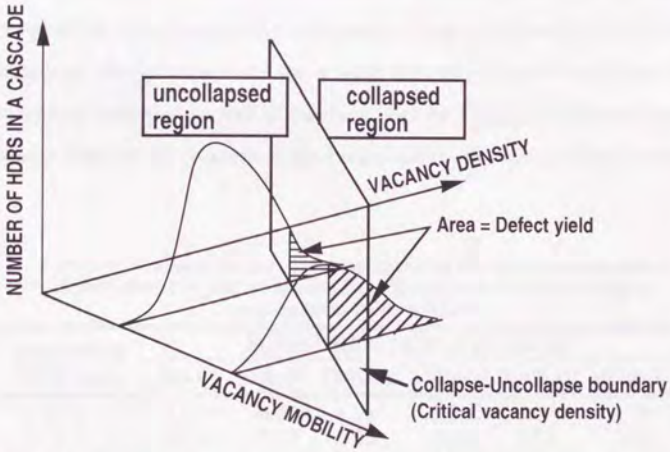

Fig. 5-11 **A schematic representation for the prediction of cascade collapse efficiency. The shaded area represents a defect yield value, which may be predicted by the critical density that depends much on the vacancy mobility of target element and the vacancy density distribution that depends on ion-target combination, as illustrated in the figure.**

Sekimura *et al.* investigated the cluster size dependence of defect yields for gold irradiated by self-ion at room temperature [5-33]. The critical density calibration presented in this work is applied to those experimental defect yield values for each cluster size that are listed in ***Table 5-6***. ***Fig. 5-12*** is a plot of ion energy versus the critical densities of each cluster size, showing that the critical densities are independent on incident ion energies, except for the 20 and 50 keV irradiations due to the same reason described at the beginning of this section. It indicates that the spatial distribution of vacancies at the end of the collisional phase is fully correlated with the size distribution of vacancy clusters observed by TEM after the irradiations. One may consider that this correlation is not easily acceptable, because the vacancy clusters formed by the collapse of cascade defects during the cooling phase are able to grow after the subsequent thermal phase since vacancies can migrate at room temperature. However, if one consider that the fraction of vacancies freely migrating for a long distance is very small at room temperature and the growth of clusters may be largely influenced by the vacancies close to the clusters at the temperature, the independence of the

Table5-6 **Vacancy cluster size dependence of the experimental defect yield values for gold irradiated by self-ions with incident energies ranging from 20 to 400 keV.**

CLUSTER SIZE (nm)	MEASURED DEFECT YIELD					
	20keV	50keV	100keV	200keV	300keV	400keV
≥ 1	0.070	0.43	1.18	1.59	1.78	2.05
≥ 2	0.070	0.40	1.02	1.50	1.78	1.93
≥ 3	0.063	0.29	0.68	1.09	1.54	1.37
≥ 4	0.014	0.13	0.40	0.63	0.89	0.87
≥ 5	-	0.077	0.23	0.33	0.45	0.35
≥ 6	-	0.055	0.091	0.19	0.25	0.15
≥ 7	-	0.025	0.033	0.10	0.14	0.091
≥ 8	-	0.014	0.017	0.068	0.067	-

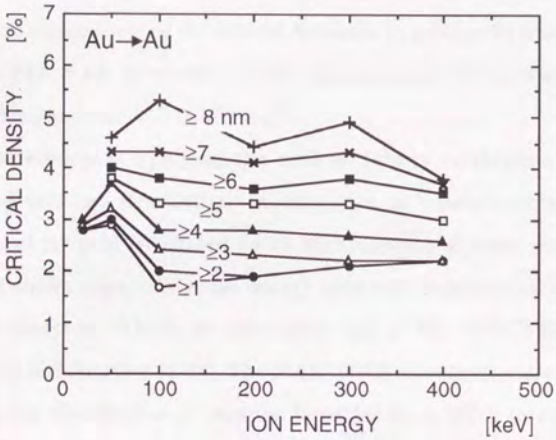

Fig. 5-12 **Critical densities for each size of the clusters that is observed in self-ion irradiated gold at room temperature. If one excludes 20 and 50 keV irradiations because of their very limited data, the critical densities are independent of incident ion energies.**

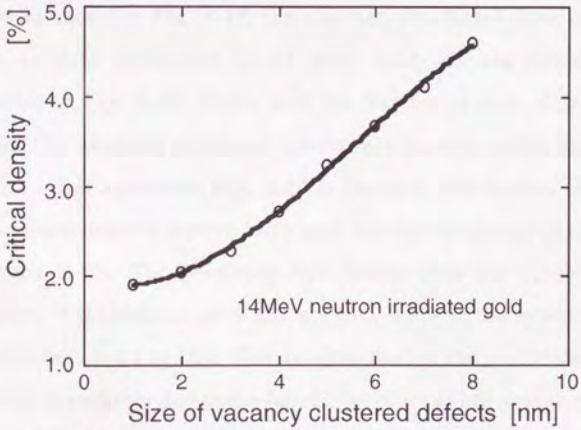

Fig. 5-13 **Cluster size dependence of critical densities in gold irradiated by self-ion at room temperature. The critical densities are averaged over the ion-energy range from 100 to 400 keV.**

critical densities on incident ion energies may not be unreasonable. The cluster size dependence of the critical densities in self-ion irradiated gold is shown in ***Fig. 5-13***, where the critical densities are averaged over the ion energies ranging from 100 to 400 keV.

The possibility of applying the critical density calibration using the results of self-ion irradiation experiments to neutron irradiation is investigated for gold irradiated by 14 MeV neutron at room temperature. ***Fig. 5-14*** shows a primary recoil energy spectrum in gold irradiated by the RTNS-II neutron, which is calculated using the SPECTER code of Greenwood and Smither [5-34]. The MARLOWE calculations are performed to obtain the distribution of vacancy densities in an *HDR* formed in 3000 single cascades that are initiated from a PKA with the kinetic energies chosen so as to fit statistically to the recoil energy spectrum of ***Fig. 5-14***. ***Fig. 5-15*** shows the distribution of vacancy densities in an *HDR* at the end of the collisional phase. Using the cluster size dependence of the critical densities as shown in ***Fig. 5-13***, the expected size distribution of vacancy clusters in gold irradiated by 14 MeV neutrons are calculated, as represented in ***Fig. 5-16***, where only the fraction of each cluster size is presented. The absolute number of the clusters depends on the thickness of irradiated metal specimen. ***Fig. 5-17*** is the size distribution of vacancy clusters experimentally observed in a gold thin foil irradiated by the *RTNS-II* neutrons [5-35]. The predicted distribution does not agree with the experiment. The predicted peak size is ~4nm, while in the experiments the peak exists between 1 to 2nm. The disagreement of the prediction with the experiment is probably due to the lack of the effect of low energy recoil that largely occurred in a neutron irradiation. In the employed ion irradiation, ion fluence is $1x10^{14}$ n/m^2, while neutron fluence in the *RTNS-II* irradiation is ~10^{20} n/m^2. In those ion irradiation, almost all incident ions with kinetic

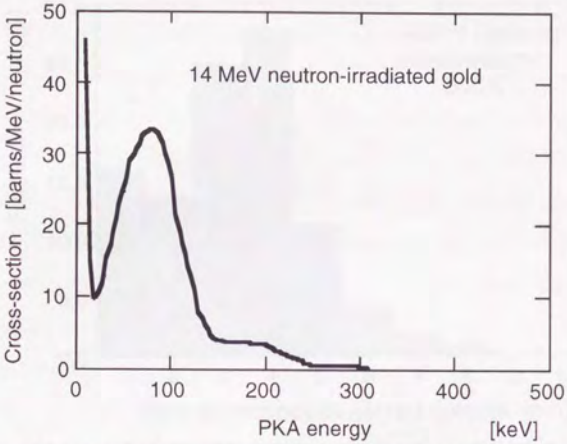

Fig. 5-14 **PKA energy spectrum in 14 MeV neutron-irradiated gold, estimated using the SPECTER code of Greenwood and Smither.**

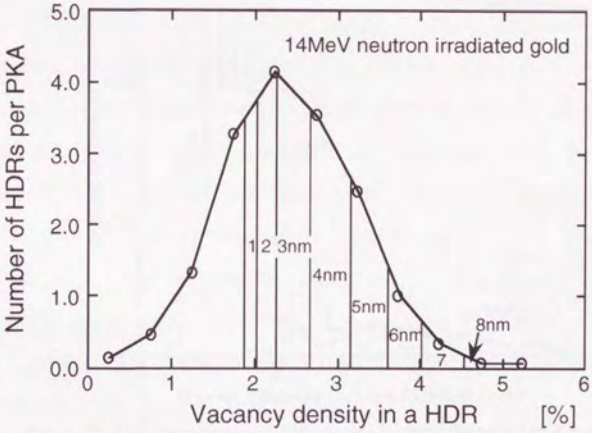

Fig. 5-15 **Distribution of vacancy density in an *HDR* at the end of the collisional phase in 14 MeV neutron irradiated gold at 300K, calculated using the MARLOWE code.**

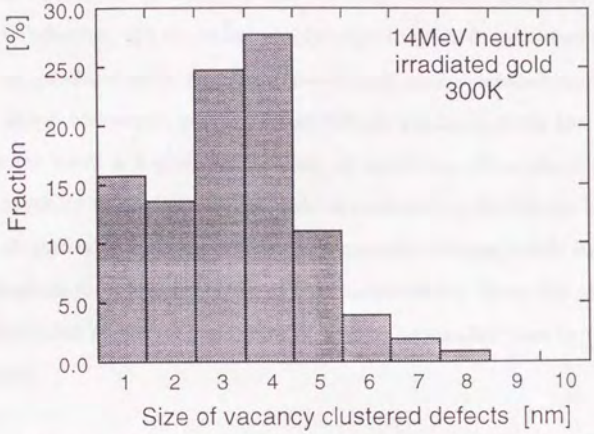

Fig. 5-16 **Predicted size distribution of vacancy clusters in gold irradiated by RTNS-II neutrons.**

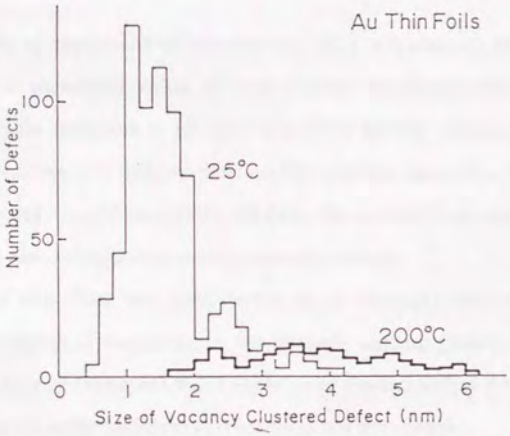

Fig. 5-17 **Size distribution of vacancy clusters observed in a gold thin foil irradiated using RTNS-II neutrons.**

kinetic energies ranging from 20 to 400 keV will produce large cascades that have an ability to collapse into vacancy clusters. However, in the neutron irradiation, the overwhelmingly large number of neutrons will not be able to produce such cascades, producing much greater number of Frenkel pairs. Moreover, such Frenkel defects produced from low energy recoil atoms have a higher probability of surviving. Therefore, a large amount of freely migrating interstitials is expected to shrink the existing vacancy clusters that have been formed by cascade collapse, while vacancies cannot migrate for a long distance at this temperature. Thus, the observed size distribution of vacancy clusters is shifted to smaller size in neutron irradiations.

5-5 Summary

The analysis of experimental results and *BCA* simulations shows that there exists the threshold value of local atomic displacements (i.e., the critical density) for cascades to collapse into TEM-visible vacancy clusters. The critical densities are independent on the cascade energy in the same material. Moreover, in self-ion irradiated gold, the critical densities for each cluster size are also independent on the cascade energy.

The critical densities are considered to be strongly related to the mobility *or* transport of vacancies in the cascade cooling phase. A precise estimation of vacancy transport will enable us to predict defect yield values in arbitrary metals under arbitrary irradiation environments.

In application of ion-irradiation data to neutron irradiations, the effects of low energy recoil must be incorporated into the analysis.

References 5

[5-1] M.T. Robinson and I.M. Torrens, Phys. Rev. B9 (1974) 5008.

[5-2] H.L. Heinisch and B.N. Singh, Phil. Mag. A67 (1993) 407.

[5-3] N. Sekimura, Y. Kanzaki, S.R. Okada, T. Masuda and S. Ishino, in: Sixth International Conference on Fusion Reactor Materials (ICFRM6) Stresa, ITALY (1993), to be published in J. Nucl. Mater; T. Masuda, Graduate Thesis (1993) University of Tokyo; Y. Kanzaki, Master of Engineering Thesis (1993) University of Tokyo.

[5-4] K.L. Merkle, L.R. Singer and J.R. Wrobel, Appl. Phys. Lett. 17 (1970) 6.

[5-5] T. Schober, Phys. Stat. Sol. (a) 1 (1970) 307.

[5-6] M. Kiritani, H. Kato, M. Hoshino, H. Matsui and N. Matsunami, J. Nucl. Mater. 191-194 (1992) 1128.

[5-7] A.Y. Stathopoulos, Phil. Mag. A44 (1981) 285.

[5-8] A.Y. Stathopoulos and C.A. English, J. Nucl. Mater. 108 & 109 (1985) 69.

[5-9] I.M. Robertson, J.S. Vetrano, M.A. Kirk and M.L. Jenkins, Phil. Mag. A63 (1991) 299.

[5-10] M.L. Jenkins, C.A. English and B.L. Eyre, Phil. Mag. 38 (1987) 97.

[5-11] C.A. English and M.L. Jenkins, Mater. Sci. Forum 15-18 (1987) 1008.

[5-12] F. Haussermann, Phil. Mag. 25 (1972) 583.

[5-13] Z. Kopal, Numerical Analysis 2nd ed. (Wiley, New York, 1961) p.367.

[5-14] O.B. Firsov, J. Exp. Theor. Phys. (USSR) 36 (1959) 1517; O.B. Firsov, Sov. Phys. JETP 9 (1959) 1076.

[5-15] G. Moliere, Z. Naturforsch. A2 (1947) 133.

[5-16] I.M. Torrens and M.T. Robinson, in: "Interatomic Potentials and Simulation of Lattice Defects" (edited by P.C. Gehlen, J.R. Beeler and R.I. Jaffee) Plenum, New York (1972) p.423.

[5-17] M.W. Guinan and J. Kinney, J. Nucl. Mater. 133-134 (1985) 357.

[5-18] G. Wallner, M.S. Anand, L.R. Greenwood, M.A. Kirk, W. Mansel and W. Waschkowski, J. Nucl. Mater. 152 (1988) 146.

[5-19] Report on: Standard estimation method of materials irradiated by accelerated particles, edited by S.Ishino (1985) p.35.

[5-20] S. Ishino, Radiation Damage (University of Tokyo Press, Tokyo, 1987) p.15 (in Japanese).

[5-21] M. Kiritani, M. Konno, T. Yoshiie and S. Kojima, Mater. Sci. Forum 15-18 (1987) 181.

[5-22] L. De Schepper, G. Knuyt, L.M. Stals, D. Segers, L. Dorikens-Venpraet, M. Dorinkens and P. Moser, Mater. Sci. Forum 15-18 (1987) 131.

[5-23] M. Kiritani, J. Phys. Soc. Jpn. 40 (1976) 1035.

[5-24] J.N. Mundy, S.T. Ockers and L.C. Smedskjaer, Mater. Sci. Forum 15-18 (1987) 199.

[5-25] T. Diaz de la Rubia, R.S. Averback, R. Benedek and W.E. King, Phys. Rev. Lett. 59 (1987) 1930.

[5-26] D.K. Tappin, private communication; I.M. Robertson, D.K. Tappin and M.A. Kirk, Philos. Mag. A68 (1993) 843; D.K. Tappin, I.M. Robertson and M.A. Kirk, submitted to Philos. Mag. A (1993).

[5-27] C.P. Flynn and R.S. Averback, Phys. Rev. B38 (1988) 7118.

[5-28] P.B. Allen, Phys. Rev. Lett. 59 (1987) 1460; P.B. Allen, T.P. Beaulac, F.S. Khan, W.H. Butler, F.J. Pinski and J.C. Swihart, Phys. Rev. B34 (1986) 4331; P.B. Allen, Phys. Rev. B36 (1987) 2920.

[5-29] D.A. Papaconstantopoulos, Handbook of the Band Structure of Elemental Solids (Plenum, New York, 1968).

[5-30] W.L. McMillan, Phys. Rev. 167 (1968) 331.

[5-31] G.H. Vineyard, Rad. Effects 29 (1976) 245.

[5-32] C. Kittel, Introduction to Solid State Physics (Maruzen Tokyo, 1978) p.118 (in Japanese).

[5-33] N. Sekimura, Y. Kanzaki, S.R. Okada, T. Masuda and S. Ishino, private communication.

[5-34] L.R. Greenwood and R.K. Smither, Report No. ANL/FPP/TM-197 (1985) Argonne National Lab., USA.

[5-35] M. Kiritani, J. Nucl. Mater. 155-157 (1988) 113.

Chapter 6

ON APPLICATION OF COMPUTER SIMULATION TECHNIQUE TO CASCADE DAMAGE PROCESSES

6-1 Computational Studies of Cascade Damage Processes

Radiation damage processes, from initial defect production to microstructure evolution, occur over a wide spectrum of the time and size scale [6-1], as shown in ***Fig 6-1***. Atomic collision sequences during the collisional phase continue for a few tenth of picosecond in a small region on nanometer scale. The subsequent cooling phase takes place for ~10^{-11} sec, showing a liquid-like structure of atomic configuration at the cascade core. Relatively short range (~10^{-8} m) migrations of defects occur during the thermal phase (~10^{-6} sec), followed by a long range (~10^{-6} m) migrations in the diffusional phase (~10^{-3} sec). Thus, a physical description of the cascade processes is widely varied with increasing time, from the ballistic binary collisions to the many-body interactions, followed by the thermally activated processes. The practical problem in the fission and fusion reactors are those

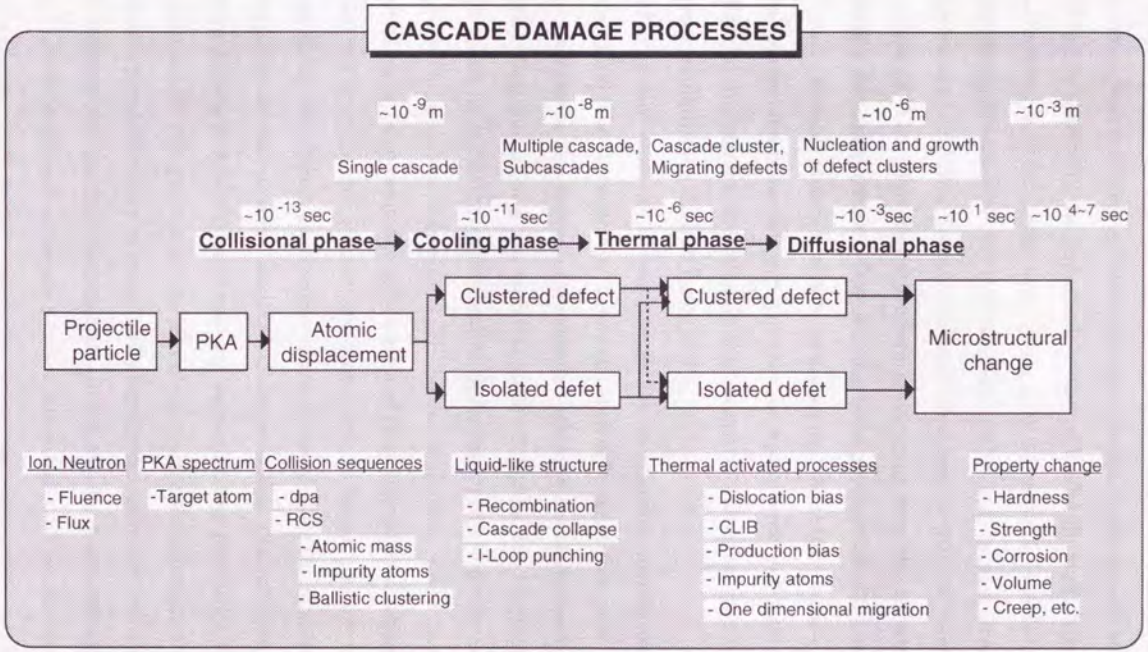

Fig. 6-1 **A schematic representation of a wide spectrum of time and size scale on cascade damage processes.**

in the time range up to 10^9 sec [6-1], including the cascade damage processes described above. However, experimental information is almost confined to observing the end result of the radiation-induced defects and their interactions on a global scale, from in-situ observations [6-2] of defect diffusion processes with a time constant of 10^{-3} sec, to post-irradiation examinations of final microstructural changes at 10^1~10^7 sec after irradiations. Therefore, there are two major gaps over the time scale of radiation damage processes. One is a long term problem from 10^7 sec up to 10^9 sec, where plant lifetime expansion, ultrahigh burn-up fuel development and materials development for fusion first wall and blanket structural application are fall into this category. The other gap lies in a shorter term problem than 10^{-3} sec.

One of the most important issues for irradiation correlation is to understand the interaction between projectile particles and target materials, since the spread of a cascade including the defect and energy spatial distribution and the survival ratio of defects are the essence of differences in radiation effects under different irradiation sources. The short term problem contains such issue. Atomistic scale computer simulation is, at present, the only means of obtaining detailed information on spatial arrangement of individual point defects in the primary damage state. Molecular dynamics computer simulations provide the most realistic description of the primary damage state including the collisional and cooling phases [6-3~20]. Binary collision approximation provides a realistic description of the gross features of defect spatial distribution with the requisite physical reality in statistically significant numbers, including the size, number and spacing of subcascades [6-21~26]. Short-term annealing in the thermal phase and subsequent defect interactions in the cascade region are well-described using stochastic annealing simulation method [6-

27,28,29]. The basic premise of the method is that point defects and defect clusters are treated as entities that interact through thermally activated diffusion. The defects are associated with crystal lattice sites, and the movement of mobile defects by hopping is governed by the numbers of the various types of defects and their relative jump frequencies. Interactions occur when two defects come within the critical reaction distance for their types. Diffusion rate theory equations are applied to intercascade interactions of defects during the cascade diffusional phase [6-30~32]. In those works, point defect and defect clusters are described by their concentrations, not by atomistic size scale. Thus, individual simulation method is almost established, providing much information on each defect interaction in the cascade processes with time constant less than 10^{-3} sec.

If one employs an appropriate interatomic potential, the molecular dynamics technique can provide an appropriate description of the whole range of the cascade damage processes, from the collisional to diffusional phases. However, the size scale of defect interaction increases with increasing time, making it difficult to simulate the processes using the single calculation technique. For comprehensive understanding of cascade damage processes and direct comparison of computer simulation results with corresponding experimental results, several simulation techniques should be integrated. The integration will be possible by taking the following methodology; the output results obtained from a certain simulation method are employed as the input parameters of another method simulating subsequent processes. However, the integration is not at present fully developed.

The hybrid method of the binary collision approximation with the stochastic annealing simulation is developed individually by Heinisch *et al.* [6-22] and Muroga *et al.* [6-21]. In those works, lacking any knowledge of

atomic motion in the cooling phase, the stochastic annealing simulation is applied to the cascades that had undergone only the collisional phase. The results of the molecular dynamics simulation of the cascade cooling phase may be required to be incorporated into their works.

Liquid droplet treatment of Alurralde *et al.* [6-33] is the method to obtain a description of the cascade behavior beyond the collisional phase, where the binary collision approximation is coupled with the heat equation. However, such a treatment is not reasonable for the validity of physical argument, since the spatial distribution of kinetic energy deposition extracted from the binary collision approximation is poorly described, moreover, the atomic-level behavior of defect interactions after the cooling phase are not considered in their approach.

For simulating all through the cascade damage processes, the new method beyond the existing simulation techniques is required to be developed, available at reasonable computational cost. In the present chapter, the possibility of extension of cascade damage simulations is discussed. Thermodynamical treatment of the cooling phase will be discussed in *section 6-2*, and the unified approach of molecular dynamics with finite difference method is suggested in *section 6-3*.

Individual simulation methods employed in the present studies are empirical to fit the basic material properties, such as vacancy formation energies, balk modulus, elastic constant, the heat of solution of binary alloys, equilibrium lattice constant, sublimation energies and threshold displacement energies. However, the direct comparison between the end result of computer simulations and that of experiments is not performed in the present studies because individual time scales are not comparable. At low temperature irradiation where the thermal and diffusional phases of cascades are not so prominent, it is possible to correlate the primary state of

cascade processes simulated using the atomistic simulation methods employed in the present studies with the corresponding result of experiments, as shown in *chapter 5*. At high temperature irradiation, on the other hand, the dominant interaction of defects is a thermally activated process represented by the random walk of defects. These thermal interactions of defects are well-described using stochastic annealing simulation and diffusion rate theory that are beyond the scope of the present studies. In such case, irradiation-induced microstructural changes might be correlated using parameters that are strongly related with irradiation temperature and surrounding microstructures. An introduction of irradiation correlation parameters including the effects of the thermally activated process of defects is still left to be further studied.

6-2 Thermodynamical Evaluation of the Cascade Primary State

Molecular dynamics calculation is performed using the modified GRAPE code, which is described in *chapter 2*, to study the cooling phase of a cascade in gold from the thermodynamic point of view. Interatomic interaction is described using the pair-wise Morse potential [6-34], which is adjusted by the cohesive energy, elastic constants and compressibility of gold. The total number of atoms is 10800 corresponding to a rectangular parallelepiped of $15a_0$ x $15a_0$ x $12a_0$, where a_0 is the lattice constant. Periodic boundary condition is employed in the present calculation, so that the calculated system is thermally insulated. At time $t=0$ sec, kinetic energy, 250 eV, is deposited to one atom (PKA), whose direction is [120]. Initial lattice temperature is 0 K.

Fig. 6-2 is a plot of the number of displaced atoms as a function of time, showing a initial increase followed by a decrease due to the spontaneous

recombination of unstable defect pairs, where a displaced atoms is defined to be displaced by over one-quarter of the lattice constant from the nearest lattice site. The time dependence of average kinetic energies is also represented in the figure. In the collisional phase the average kinetic energy rapidly decreases due to conversion of the kinetic energies to potential energies, establishing approximate equipartition of energy. During the subsequent cooling phase the kinetic energy remains constant due to the thermally insulated system. However, during the cooling phase, the migration of interstitial atoms with relatively high kinetic energies (0.1~1 eV) is observed. Moreover, the velocity distribution of moving atoms changes and gradually approaches the Maxwell-Boltzmann distribution as shown in ***Fig. 6-3***. At the initial stage of the cooling phase (0.26 psec), the system is strongly deviated from thermal equilibrium, while at 2 psec, equilibrium velocity distribution has been almost established. Moreover, if

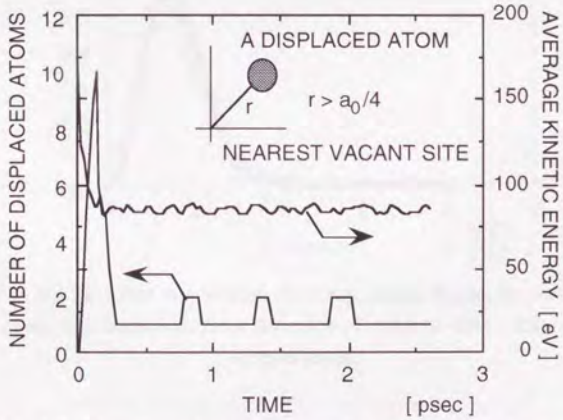

Fig. 6-2 **Time dependence of the number of displaced atoms and average kinetic energy in a 250 eV cascade in gold.**

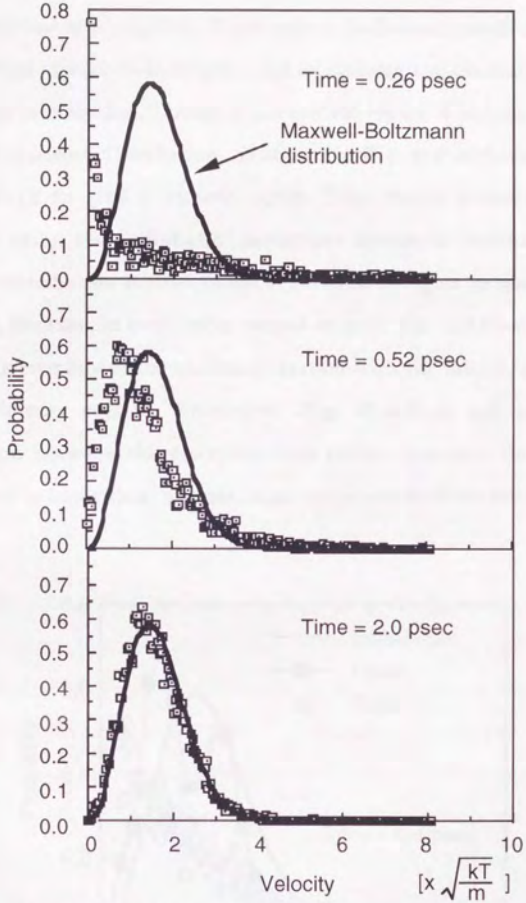

Fig. 6-3 **Velocity distribution of moving atoms during the cooling phase of a cascade initiated from 250 eV PKA for three different elapsed times.**

one takes a closer look at a local region, near-equilibrium condition has been established much earlier. If the system is divided into 27 regions (cut into one third of each side length) and examining the central part of the cascade, the velocity distribution of the central region is almost close to the Maxwell-Boltzmann distribution, as shown in ***Fig. 6-4***, although statistics is not enough to give a smooth curve. This result presented here is calculated using the "adiabatic" molecular dynamics technique, where electronic contribution to dissipation of thermal energies in cascades is not considered, because, in such noble metals as gold, the contribution is small due to weak coupling of the electronic system with the lattice, as discussed in the following section. Therefore, ***Fig. 6-4*** does not indicate an equilibration between the electronic and lattice systems. However, this figure seems to imply that, at least, local temperature of the lattice system

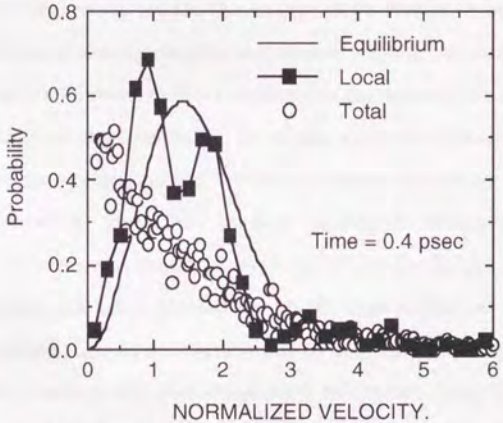

Fig. 6-4 **Velocity distribution of moving atoms during the cooling phase of a cascade initiated from 250 eV PKA, for total calculated volume and for the central 1/27 of the total volume.**

can be defined even at such an early stage of the cooling phase of cascade evolution. This may justify Monte Carlo type calculation of defect jump processes during the cooling and thermal phases of cascades [6-21].

6-3 A Unified Approach of Molecular Dynamics Method and Finite Difference Method

Recently, the molecular dynamics computer simulation has been shown to be a powerful tool to describe the behavior of energetic displacement cascades in the primary state. According to the molecular dynamics studies, a critical importance of the cooling phase is highlighted in determining the amount of atomic rearrangement. In the cooling phase commonly termed a thermal spike stage, atom trajectories are diffusive as opposed to ballistic in the collisional phase.

In the thermal spike model the energy deposited in a local region is quickly partitioned among neighboring atoms, raising the region to a very high temperature followed by the temperature decreases with spreading the heat by thermal conduction [6-35]. In metals most of the heat deposited in the lattice is generally transported to electrons, depending on electron-phonon interaction. However, in the "standard molecular dynamics simulation", the thermal conductivity is obviously the lattice conductivity. Flynn and Averback have pointed out [6-36] that neglect of the electron-phonon coupling may lead to overestimate of thermal spike temperatures in many metals, because the phonon-phonon relaxation time ($\tau_{ph\text{-}ph} \approx 10^{-11}$ sec) is comparable to the time constant of electronic thermalization of lattice ($\tau_{ph\text{-}e} \approx 10^{-11}$ sec).

Caro and Victoria [6-37] have proposed a simple model to describe the metallic thermal conductivity by coupling ions to electronic system as a

thermal reservoir using the Langevin equation generating the canonical ensemble [6-38]. Their formalism was incorporated into the MOLDYCASK code by Prönnecke *et al.* [6-39]. The Langevin equation is described as

$$m\ddot{x}_i = F_i + \eta_i(t) + \beta_i \dot{x}_i \ , \tag{6.1}$$

where, η_i is a random force and β_i is the damping term that is written empirically as

$$\beta_i = A \log_{10}(B\rho_i^{1/3} + C) \ . \tag{6.2}$$

Here, B is a constant and ρ_i is host electron density estimated using EAM potential framework. The numbers A and C are adjustable parameters to empirically fit the coupling constant that is obtained from experiments [6-40,41] *or* electronic excitation theory [6-42]. However, their work has not considered an effect of the electronic heat conductivity, so that the formalism can only be applied to such weakly electron-phonon coupling system as copper, silver and gold, where electronic temperature is considered to remain constant all through the cascade thermal spike stage.

Finnis *et al.* [6-43] have proposed another formalism for the electron-phonon coupling effects into molecular dynamics technique. They adopted a damping force, $\boldsymbol{F}_i$, to each ion in the form,

$$\boldsymbol{F}_i = -\mu \boldsymbol{v}_i \ , \tag{6.3}$$

where, μ is the damping constant which satisfied

$$-\mu \boldsymbol{v}_i \cdot \boldsymbol{v}_i = -3k_B \alpha (T_i - T_e) \ . \tag{6.4}$$

Here, $-3k_B\alpha(T_i - T_e) = \frac{\partial}{\partial t}(3k_B T_i) = \boldsymbol{F}_i \cdot \boldsymbol{v}_i$ is the rate of change of thermal energy. Electronic temperature was assumed to be constant, the ambient temperature.

Car and Parrinello [6-44] have proposed a unified scheme that, by combining the molecular dynamics with the density-functional theory, profoundly extends the range of both concepts. The approach extends the molecular dynamics beyond the usual pair-potential approximation, thereby making possible simulation of both covalently bonded and metallic systems [6-44~47]. Although this *ab-initio* molecular dynamics can reproduce atomic configuration with high accuracy, it does not necessarily guarantee the dynamic behavior of atoms without a careful treatment [6-48]. Moreover, since an excessive computational load is needed, it is practically at present impossible to apply this approach to the cascade damage evolution, where 10^6-10^8 atoms are, at least, required in calculations.

In the present study that follows, a unified scheme of a microcanonical molecular dynamics method with a finite difference method is proposed. The aim of the present work is twofold; one thing is to incorporate the electronic thermal conductivity into a standard molecular dynamics without an excessive increment of computational cost, and another is to develop a comprehensive simulation method that covers the cascade processes from the cooling to thermal phases.

Cascade damage region is considered to be consist of two regions: One is the region where displacement damage takes place. It should be described by an atomistic scale simulation, as molecular dynamics (MD) technique. The other is the region where only the thermal damage is expected to occur, described by a continuum approximation approach, as finite different method (FDM). In the present work, the cascade damage region is divided

into several computational FDM cells, and all heat conductions are treated in the FDM framework. Moreover, MD cells are embedded into the center of the FDM cells as shown in ***Fig. 6-5***, ranging so as to cover the cascade displacement damage region. Atom behavior is treated in the MD approach. The electronic and lattice temperatures are individually defined for each FDM cell, and the phonon and electron systems are coupled as shown in ***Fig. 6-6***. The details of application of the electron-phonon coupling based on the Allen's model [6-40] to the FDM approach have been already discussed in *chapter 5*. In order to calculate the temperature evolution of phonons and electrons including the effects of the electron-phonon coupling, and to observe the atomic rearrangement in the cascade volume, the following procedure is proposed here. This approach should be applied to the cascade evolution after the cooling phase where local lattice temperatures can be defined.

(1) The electronic and lattice temperatures at time t=(k+1)Δt in all regions are estimated from the previous temperatures at t=kΔt, using the FDM approach, as shown in *chapter 5*. The following equations of thermal conduction are applied to each FDM cell.

$$\rho_0 C_e \frac{\partial T_e}{\partial t} = \kappa_e \nabla^2 T_e - G(T_e - T_l) \tag{6.5}$$

$$\rho_0 C_l \frac{\partial T_l}{\partial t} = \kappa_l \nabla^2 T_l + G(T_e - T_l) \tag{6.6}$$

where, T_e and T_l are the electronic and lattice temperatures (K), κ_e and κ_l are the electronic and lattice thermal conductivity (J/sec/K/m), G is the electron-phonon coupling constant (J/sec/K/m^3), ρ_0 is the molar density of atoms (mol/m^3), and C_e and C_l are the electronic and lattice specific heat coefficients (J/mol/K), respectively.

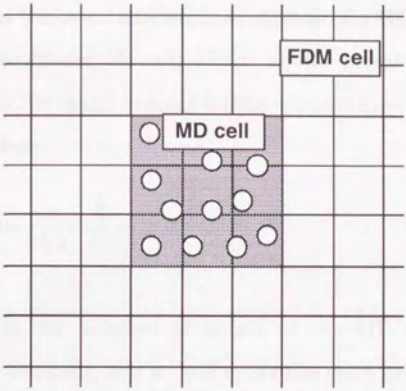

Fig. 6-5 **A schematic representation of the unified approach of the thermal spike stage simulation.**

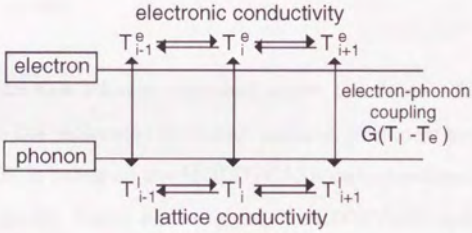

Fig. 6-6 **A schematic representation of the coupling of lattice system with electronic system.**

(2) The atom velocities in the MD cell, j, are scaled with the new lattice temperatures estimated in the FDM calculations.

$$\boldsymbol{v}_i^{'}(t) = \boldsymbol{v}_i(t)\,[1 + a\,\{(\frac{T_j}{T(t)})^{1/2} - 1\}]\ , \qquad (6.7)$$

where, T_j is the new lattice temperature at the MD cell j, and α is a variable parameter ($0 \leq \alpha \leq 1$) which allows temperature statistical fluctuation. $T(t)$ is the present lattice temperature at the MD cell, j, calculated from

$$T(t) = \frac{1}{3Nk_B} \sum_{i=1}^{N} m_i \boldsymbol{v}_i(t)^2 , \qquad (6.8)$$

where, N is the number of atoms in the MD cell j, k_B is the Boltzmann constant, and m_i and $\boldsymbol{v}_i$ are the mass and velocity of atom i in the MD cell j.

(3) A standard MD method is performed, computing phase space trajectories of a collection of atoms which individually obey classical laws of motion.

Based on the new scheme described above, the finite difference method is combined to the molecular dynamics method. This new program, termed MOLDYSPIKE, is based on the MOLDYCASK code developed by Diaz de la Rubia *et al.* [6-49]. Since the original MOLDYCASK code has already incorporated the electronic conductivity of Caro and Victoria's model [6-37] where electronic temperature is assumed to be constant, their model is removed in this work. The new MOLDYSPIKE can estimate the fluctuation of electronic temperature, incorporating the effect of the electron-phonon coupling into the rearrangement of atoms in the thermal spike stage. Besides, it can also evaluate the electronic and lattice temperatures of the outside of the MD cells. Once the theory of standard defect diffusion based on the random walk of defects is assumed to be valid, the program enables us to calculate, not only the behavior of atoms in the MD cells by using the standard MD scheme, but also the migrations of defects in the surrounding

region during the cooling phase. Moreover, the migrations of defects during the thermal phase can also be estimated in all the computational regions.

Preliminary calculations are performed for simulating thermal spike events in copper and nickel, using the unified approach developed here. The embedded atom method (EAM) potential of Foiles *et al.* [6-50] is employed for describing the interactions of atoms in the MD cell. The crystallites are cubic cells containing 10976 atoms, equilibrated at 300 K prior to an initiation of the spike event. Thermal spike events are introduced into the MD cell by endowing the atoms in the center of the crystal with the Gaussian radial distribution of velocities corresponding to deposited energy 10000 eV. The width of the Gaussian is chosen as $5a_0$, where a_0 is the lattice constants. In the present calculations, just one MD cell is embedded into the FDM cells. The MD cell is not linked with the FDM cells in the first 50 times of MD steps, during which about half of deposited kinetic energies converts to potential energies to establish approximate equipartition of deposited energy. After the time when the equipartition is almost established, i.e., when local temperatures can be defined, the MD cell is coupled with the FDM cells. As for an initial condition of the FDM calculation at the time when the MD cell is just coupled with the FDM cells, it is natural to consider that the lattice temperature of the FDM cell coupling the MD cell is matched to the occasional MD lattice temperature, the other surrounding lattice temperatures are set at the irradiation temperature and all the electronic temperatures are set so as consistent with the energy transfer from the lattice to the electrons in the collisional phase ($\tau_{e\text{-}ph} \approx 10^{-13}$ sec, $\tau_{e\text{-}e} \approx 10^{-13}$ sec). For simplicity, however, in these preliminary calculations, the spatial distribution of initial lattice temperatures is assumed to be the Gaussian radial distribution so that the initial lattice temperatures are smoothly distributed, as follows.

$$T_l = T_l^0 \exp\left(-\frac{r^2}{R^2}\right) + T_{amb} \tag{6.9}$$

Initial electronic temperatures are constant for all the FDM cells.

$$T_e = T_{amb} \ , \tag{6.10}$$

where, T_{amb} is the ambient temperature, 300K. $T_l\ (t = t_0) = T_l^0 + T_{amb}$ is the average kinetic temperature at the MD cell, where t_0 is the time when the MD cell and FDM cells are just started to be coupled with each other.

Fig. 6-7 is a plot of changes in kinetic energies averaged over the atoms in spherical cascade volume with radius of $5a_0$ (a_0 is the lattice constant) in the MD cell, as a function of the elapsed time from the spike initiation, for the heat spike events in (a) copper and (b) nickel. For comparison, results for the case of the event, where the MD cell is not coupled with the FDM for all time, are also shown in the figure. In copper, the time decay constants of average kinetic energy dissipation are 2.4 and 3.5 psec for the coupled and uncoupled events, respectively. In nickel, those are 0.95 and 3.0 psec for the coupled and uncoupled events, respectively. The fractions of the time constant for the coupled event to that for the uncoupled are 0.69 and 0.32 in copper and nickel, respectively. ***Fig. 6-8*** shows the time dependencies of mean square displacement (*MSD*) in the cascade volume with radius $5a_0$, for (a)copper and (b)nickel. Due to the coupling with the electronic system, the mean square displacements are reduced by ~2/3 and ~1/5 in copper and nickel, respectively, showing that strong electron-phonon interaction suppresses atomic rearrangement during the cascade cooling phase.

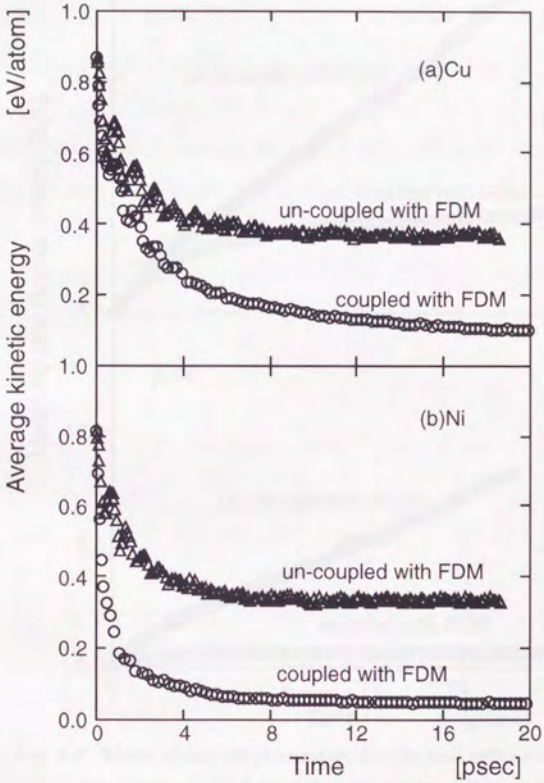

Fig. 6-7 **Average kinetic energy changes for the heat spike events in (a)copper and (b)nickel, as functions of time.**

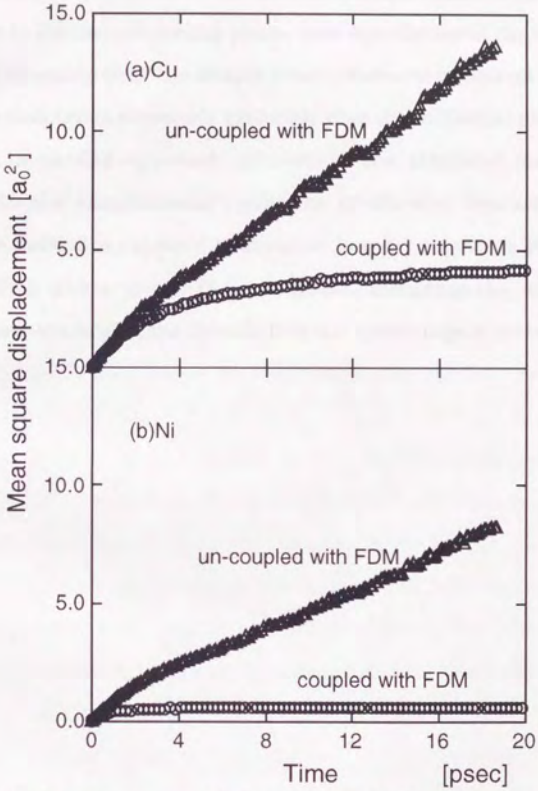

Fig. 6-8 **Mean square displacements for the heat spike events in (a)copper and (b)nickel, as functions of time.**

6-4 Summary

The possibility of extension of cascade process simulation is discussed. At early stage in the cascade cooling phase, local equilibrium of the lattice is established, indicating that the simple jump processes of defects may be applied to the simulation of cascade evolution after the collisional phase.

Moreover, a unified approach connecting the standard molecular dynamics with the simultaneous equations of thermal conductivity is proposed. The method is expected to simulate long-term cascade evolution from the cooling phase to the thermal phase, including the effects of electron-phonon coupling on the cascade thermal spike stage in metals.

References 6

[6-1] S. Ishino, J. Nucl. Mater. 206 (1993) 139.

[6-2] S. Ishino, K. Hasegawa, H. Kawanishi and K. Someya, Final Report of Research Project, Grant-in-Aid for Scientific Research from Monbusho for FY 1977-1978 (March 1979); S. Ishino, H. Kawanishi, K. Fukuya and T. Muroga, IEEE Trans. Nucl. Sci. NS 30 (1983) 1255; S. Ishino, T. Muroga and N. Sekimura, Nucl. Eng. Design/Fusion 2 (1985) 3; S. Ishino, S. Iwata, N. Sekimura and A. Kohyama, Fusion Eng. Design 7 (1989) 237; S. Ishino, N. Sekimura, H. Sakaida and Y. Kanzaki, Mater. Sci. Forum 97-99 (1992) 165.

[6-3] J. B. Gibson, A. N. Goland, M. Milgram and G. H. Vineyard, Phys. Rev. 120 (1960) 1229.

[6-4] T. Diaz de la Rubia, R. S. Averback, R. Benedek and W. E. King, Phys. Rev. Lett. 59 (1987) 1930; T. Diaz de la Rubia, R. S. Averback, H. Hsieh and R. Benedek, J. Mater. Res. 4 (1989) 579; T. Diaz de la Rubia, R. S. Averback, R. Benedek and I. M. Robertson, Rad. Eff. Def. Sol. 113 (1990) 39; T. Diaz de la Rubia and M. W. Guinan, J. Nucl. Mater. 174 (1990) 151; T. Diaz de la Rubia and M. W. Guinan, Phys. Rev. Lett. 66 (1991) 2766; T. Diaz de la Rubia and M. W. Guinan, Mater. Sci. Forum 97-99 (1992) 23.

[6-5] R. S. Averback and T. Diaz de la Rubia, Nucl. Instr. and Meth. B33 (1988) 693; R. S. Averback, T. Diaz de la Rubia, H. Hsieh and R. Benedek, Nucl. Instr. and Meth. B59/60 (1991) 709; R. S. Averback, H. Hsieh , T. Diaz de la Rubia and R. Benedek, J. Nucl. Mater. 179-181 (1991) 87.

[6-6] H. Hsieh, R. S. Averback, H. Sellers and C. P. Flynn, Phys. Rev. B45 (1992) 4417.

[6-7] W. E. King and R. Benedek, Phys. Rev. B23 (1981) 6335; W. E. King and R. Benedek, Point Defects and Defect Interactions in Metals, Yamada Sci. Foundation (University of Tokyo Press, 1982); W. E. King and R. Benedek, J. Nucl. Mater. 117 (1983) 26.

[6-8] M. W. Guinan and J. H. Kinney, J. Nucl. Mater. 103&104 (1981) 1319.

[6-9] S. P. Chou and N. M. Ghoniem, Phys. Rev. B43 (1991) 2490; S. P. Chou and N. M. Ghoniem, J. Nucl. Mater. 179-181 (1991) 909.

[6-10] A. El-Azab and N. M. Ghoniem, J. Nucl. Mater. 191-194 (1992) 1110; A. El-Azab and N. M. Ghoniem, Rad. Eff. Def. Sol. (1993) in press.

[6-11] H. Huang and N. M. Ghoniem, in : Proc. of ICFRM-6 (1993) to be published in J. Nucl. Mater.

[6-12] K. Morishita, N. Sekimura, S. Iwata and S. Ishino, Simulation-J. Jpn. Soc. for Simulation Technol. 10 (1991) 352 (in Japanese); K. Morishita, N. Sekimura, T. Toyonaga and S. Ishino, J. Nucl. Mater. 191-194 (1992) 1123; K. Morishita, N. Sekimura and S. Ishino, Rad. Eff. Def. Sol. (1993) in press; K. Morishita, T. Toyonaga, N. Sekimura and S. Ishino, Trans. Meter. Res. Soc. Jpn. 9 (1992) 110.

[6-13] N. V. Doan, N. Q. Lam, L. Dagens and Y. Adda, Point Defects and Defect Interaction in Metals, Yamada Sci. Foundation (Univ. of Tokyo Press 1982) 372; N. V. Doan, F. Rossi and L. Boulanger, J. Nucl. Mater. 191-194 (1992) 1106.

[6-14] F. Rossi and N. V. Doan, Nucl. Instr. and Meth. B61 (1991) 27.

[6-15] A. Tenenbaum and N. V. Doan, Philos. Mag. 35 (1977) 379.

[6-16] V. V. Kirsanov, N. N. Musin, D. G. Roskin and E. I. Shamarina, Phys. Lett. A163 (1992) 112; V. V. Kirsanov, Mater. Sci. Forum 97-99 (1992) 117.

[6-17] V. I. Protasov and V. G. Chudinov, Rad. Effects 66 (1982) 1.

[6-18] Z. Pan, Nucl. Instr. and Meth. B66 (1992) 325; Z. Pan and M. Hou, to be published in Nucl. Instr. and Meth. B

[6-19] C. Massobrio, V. Pontikis, N. V. Doan and G. Martin, J. Nucl. Mater. 179-181 (1991) 921.

[6-20] A. J. E. Foreman, W. J. Phythian and C. A. English, AEA Technology Report, AEA-TRS-2031, UKAEA Harwell, UK (1991).

[6-21] T. Muroga and S. Ishino, J. Nucl. Mater. 117 (1983) 36.

[6-22] H. L. Heinisch, J. Nucl. Mater. 108-109 (1982) 62; H. L. Heinisch, Philos. Mag. A45 (1982) 1085; H. L. Heinisch, J. Nucl. Mater. 117 (1983) 46; H. L. Heinisch, Rad. Eff. Def. Sol. 113 (1990) 53; H. L. Heinisch and B. N. Singh, J. Nucl. Mater. 179-181 (1991) 893; H. L. Heinisch and B. N. Singh, Philos. Mag. A67 (1993) 407.

[6-23] K. Morishita, H. L. Heinisch. S. Ishino and N. Sekimura, Proc. of ICFRM-6 (1993) to be published in J. Nucl. Mater.

[6-24] R. Dierckx, J. Nucl. Mater. 144 (1987) 214.

[6-25] Y. Yamamura, I. Yamada and T. Takagi, Nucl. Instr. and Meth. B37/38 (1989) 902; Y. Yamamura, J. Nucl. Mater. 179-181 (1991) 94; Y. Yamamura and W. Takeuchi, Nucl. Instr. Meth. B29 (1987) 461.

[6-26] M. Rosen and R. H. Bassel, Nucl. Instr. and Meth. B2 (1984) 592.

[6-27] D. G. Besco, GEMP-644 (1967).

[6-28] D. G. Doran, Rad. Effects 2 (1970) 249.

[6-29] H. L. Heinisch, D. G. Doran and D. M. Schwarz, Effects of Radiation on Materials, ASTM Special Technical Publication 725 (1981) 191; H. L. Heinisch, J. Nucl. Mater. 117 (1983) 46; H. L. Heinisch and B. N. Singh, J. Nucl. Mater. 191-194 (1992) 1083; H. L. Heinisch, B. N. Singh and T. Diaz de la Rubia, in : Proc. of ICFRM-6, Stresa, Italy (1993) to be published in J. Nucl. Mater.

[6-30] C. H. Woo, B. N. Singh and H. L. Heinisch, J. Nucl. Mater. 174 (1991) 190; C. H. Woo, B. N. Singh and F. A. Garner, J. Nucl. Mater. 191-194 (1992) 1224; C. H. Woo and B. N. Singh, Phys. Status Solidi B159 (1990) 609; C. H. Woo and B. N. Singh, Philos. Mag. A65 (1992) 889.

[6-31] Y. Katoh, R. E. Stoller, Y. Kohno and A. Kohyama, J. Nucl. Mater. 191-194 (1992) 1144; Y. Katoh, R. E. Stoller and A. Kohyama, in : Proc. of ICFRM-6, Stresa, Italy (1993) to be published in J. Nucl. Mater.

[6-32] T.Yoshiie and M.Kiritani, Mater. Sci. Forum 97-99 (1992) 105; T.Yoshiie, Y.Sato, S.Kojima and M.Kiritani, J. Nucl. Mater. 179-181 (1991) 954; T.Yoshiie and M.Kiritani, J. Nucl. Mater. 191-194 (1992) 1088; T.Yoshiie and M.Kiritani, to be published in Proc. of ICFRM-6 in J. Nucl. Mater.

[6-33] M. Alurralde, A. Caro and M. Victoria, J. Nucl. Mater. 183 (1991) 33; M. Caro, A. Ardelea and A. Caro, J. Mater. Res. 5 (1990) 2652; M. Alurralde, A. Caro and M. Victoria, Mater. Sci. Forum 97-99 (1992) 111.

[6-34] I. M. Torrens, Interatomic Potentials (Academic Press, New York 1972) p.54.

[6-35] F. Seitz and J. Koehler, Solid State Physics (Academic, New York, 1956), Vol. 2, p. 307.

[6-36] C. P. Flynn and R. S. Averback, Phys. Rev. B38 (1988) 7118.

[6-37] A. Caro and M. Victoria, Phys. Rev. A40 (1989) 2287.

[6-38] D. W. Heenamm, Computer Simulation Methods in Theoretical Physics (Springer-Verlag, New York, 1989), 2nd Edition, p. 55.

[6-39] S. Prönnecke, A. Caro, M. Victoria, T. Diaz de la Rubia and M. W. Guinan, J. Mater. Res. 6 (1991) 483.

[6-40] P. B. Allen, Phys. Rev. Lett. 59 (1987) 1460.

[6-41] H. E. Elsayed-Ali, T. B. Norris, M. A. Pressot and G. A. Mourou, Phys. Rev. Lett. 58 (1987) 1212.

[6-42] P. B. Allen, Phys. Rev. B36 (1987) 2920.

[6-43] M. W. Finnis, P. Agnew and A. J. E. Foreman, Phys. Rev. B44 (1991) 567.

[6-44] R. Car and M. Parrinello, Phys. Rev. Lett. 55 (1985) 2471; R. Car and M. Parrinello, Phys. Rev. Lett. 60 (1988) 204; R. Car and M. Parrinello, NATO ASI Ser B186 (1989) 455.

[6-45] F. Buda, G. L. Chiarotti, R. Car and M. Parrinello, Phys. Rev. Lett. 63 (1989) 294; F. Buda, G. L. Chiarotti, R. Car and M. Parrinello, Phys. Rev. B44 (1991) 5908.

[6-46] V. Kumar and R. Car, Phys. Rev. B44 (1991) 8243.

[6-47] I. Stich, R. Car and M. Parrinello, Phys. Rev. B44 (1991) 11092.

[6-48] Y. Morikawa and K. Terakura, J. Phys. Soc. Jpn. 48 (1993) 428 (in Japanese).

[6-49] T. Diaz de la Rubia and M. W. Guinan, J. Nucl. Mater. 174 (1990) 151.

[6-50] S. M. Foiles, M. I. Baskes and M. S. Daw, Phys. Rev. B33 (1986) 7983.

Chapter 7

CONCLUDING REMARKS

Irradiation-induced microstructural changes initiated through interactions between projectile particles and target atoms are determined by events occurring at the atomic scale. It is, therefore, considered to be taken for granted that the correlations of microstructural changes between different irradiation conditions are discussed at the atomic scale. In such a sense, the concept of dpa based on the Norgett-Robinson-Torrens (NRT) model is considered to be valid for establishing the correlation between irradiation conditions and microstructural changes. However, as represented by the experimental and theoretical studies to investigate the irradiation-induced microstructural changes, every radiation effect cannot be represented by the NRT dpa value [7-1,2]. The NRT dpa concept does not represent the net number of Frenkel pairs after cascades are quenched, nor does it include the spatial fluctuation of displaced atoms. Formation of defect agglomerations, such as loops, stacking fault tetrahedra, voids, and

other clusters, through stochastic diffusion processes considerably depends on the number of freely migrating defects, irradiation temperature and the surrounding microstructure. For such microstructure evolutions, the net number of freely migrating defects will be a correlation parameter as a function of irradiation temperature and surrounding microstructure. On the other hand, for direct defect cluster formation in nascent cascades, the spatial localization of displaced atoms and vacant lattice sites in the collisional phase is largely important rather than the number of defects averaged over space, since the duration of such interactions of defects is too short (~10^{-11} sec) for defects to migrate for a long distance. For cascade collapse, as shown in *chapter 5* [7-3], local atomic displacements are a good correlation parameter. For interstitial-dislocation-loop formation punched from nascent cascades [7-4], an difference in pressures at interfaces between cascade molten zone and surrounding crystal might be a correlation parameter. Thus, there is no unique damage parameter that adequately describes all of the various physical processes associated with cascade damage [7-5]. To establish the irradiation correlation of microstructural changes between different irradiation environments, we must determine the individual dominant parameters, depending on each individual phenomenon. Computer simulation methods are and will be a very powerful tool for modeling complexities, namely, in the present study, to extract such the dominant parameters from each phenomenon in the primary state of cascade damage processes.

A computational study of cascade damage processes mainly using molecular dynamics and binary collision approximation gives an example utilizing computer simulation techniques and it leads the present author to the following conclusions:

(1) The localization of atomic displacement is important for a primary state of cascade damage processes; the survival ratio of cascade defects, the interstitial- and vacancy-cluster formation directly in a cascade and so on. Direct vacancy cluster formations in cascades, --- so-called "cascade collapse" ---, under different irradiation environments are well correlated by the local atomic displacements. There exists a threshold minimum value in local atomic displacements for a cascade to collapse into a TEM-visible vacancy cluster.

(2) The cascade collapse depends much on the vacancy transport during the cascade cooling phase. The minimum threshold values of local atomic displacements for cascade collapse are smaller in the cases where the higher vacancy transport can take place.

(3) Atomic scale computer simulations are a powerful tool to investigate the primary state of cascade damage events. A unified scheme of the molecular dynamics with the finite different method will be an efficient procedure to incorporate the electron-phonon coupling effects into the standard MD method for simulating the cooling and thermal phases of cascade processes.

References 7

[7-1] H.L. Heinisch, J. Nucl. Mater. 155-157 (1988) 121.

[7-2] T. Muroga, M. Eguchi, N. Yoshida, N. Tsukuda and K. Kitajima, J. Nucl. Mater. 141-143 (1986) 865.

[7-3] K. Morishita, H.L. Heinisch, S. Ishino and N. Sekimura, in: Sixth International Conference on Fusion Reactor Materials (ICFRM6) Stresa, Italy (1993); to be published in J. Nucl. Mater.

[7-4] T. Diaz de la Rubia and M.W. Guinan, Phys. Rev. Lett. 66 (1991) 2766.

[7-5] S.J. Zinkle and B.N. Singh, J. Nucl. Mater. 199 (1993) 173.

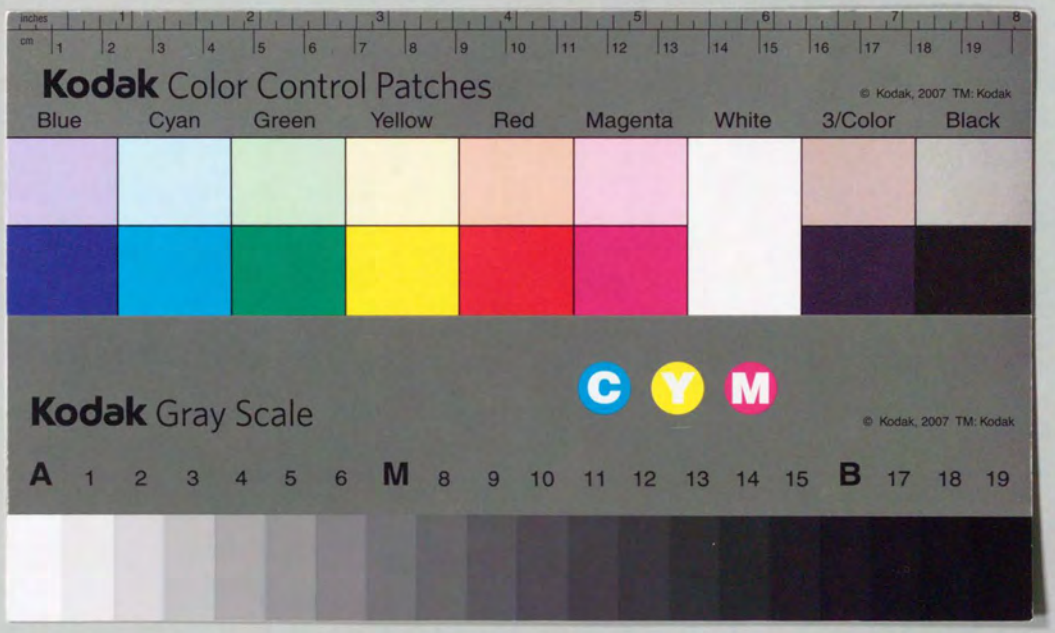
inches
cm
Kodak Color Control Patches
© Kodak, 2007 TM: Kodak
Blue
Cyan
Green
Yellow
Red
Magenta
White
3/Color
Black
C
Y
M
Kodak Gray Scale
© Kodak, 2007 TM: Kodak
A 1 2 3 4 5 6 M 8 9 10 11 12 13 14 15 B 17 18 19